TÜRKİYE CUMHURİYETİ
ADANA ALPARSLAN TÜRKEŞ SCIENCE AND TECHNOLOGY UNIVERSITY

GRADUATE SCHOOL OF NATURAL AND APPLIED SCIENCES
DEPARTMENT OF MECHANICAL ENGINEERING

EXPERIMENTAL AND FINITE ELEMENT FREE VIBRATION ANALYSIS OF A 3D PRINTED NANOCOMPOSITE POLYMER CANTILEVER BEAM

SABRİ CAN EKERER
MASTER OF SCIENCE

ADANA 2022

TÜRKİYE CUMHURİYETİ
ADANA ALPARSLAN TÜRKEŞ SCIENCE AND TECHNOLOGY UNIVERSITY

GRADUATE SCHOOL OF NATURAL AND APPLIED SCIENCES
DEPARTMENT OF MECHANICAL ENGINEERING

EXPERIMENTAL AND FINITE ELEMENT FREE VIBRATION ANALYSIS OF A 3D PRINTED NANOCOMPOSITE POLYMER CANTILEVER BEAM

SABRİ CAN EKERER
MASTER OF SCIENCE

SUPERVISOR
ASSOC. PROF. DR. CEM BOĞA

CO-SUPERVISOR
ASSOC. PROF. DR. TURAÇ FARSADİ

ADANA, 2022

DECLARATION OF CONFORMITY

I hereby declare that all information in this thesis has been obtained and presented in accordance with academic rules and ethical conduct. I also declare that, as required by these rules and conduct, I have fully cited and referenced all information that is not original to this work.

27/12/2022

[İmza]

Sabri Can EKERER

ABSTRACT

EXPERIMENTAL AND FINITE ELEMENT FREE VIBRATION ANALYSIS OF A 3D PRINTED NANOCOMPOSITE POLYMER CANTILEVER BEAM

M.Sc., Department of Mechanical Engineering
Supervisor: Assoc. Prof. Dr. Cem BOĞA
Co-Supervisor: Assoc. Prof. Dr. Turaç FARSADİ
December 2022, 158 pages

Fused Deposition Modeling (FDM) is steadily increasing its usage in manufacturing since it enables flexibility in design and significantly shortens the amount of time needed from the design phase to the first production. Like many manufacturing methods, the process comes along with some drawbacks, one of them being weaknesses in mechanical properties mostly caused by anisotropy due to the nature of the method. Nevertheless, there are many novel efforts made for overcoming these difficulties such as the inclusion of nanoparticles in the feedstock of the process which is the filament. By including these nanoparticles, researchers aim to enhance the relatively weak properties of the parts produced with Fused Deposition Modeling. Furthermore, the use of parts manufactured with this method is taking place in the Automotive and Aeronautics industries as well which requires low-weight but durable parts. Along with reliability, an important characteristic of the parts used in these industries is vibrational behavior, since these parts are subjected to intense vibration frequently. It is a known fact that if vibration caused by external forces on a part coincides with the natural frequency of the part then a phenomenon called resonance occurs causing devastating effects.

In this study, two types of nanocomposite cantilever beams composed of Acrylonitrile Butadiene Styrene (ABS) containing Calcium Carbonate ($CaCO_3$) nanoparticles of 1%, 2%, 3%, and 5% in weight fraction and ABS containing Carbon Black (CB) nanoparticles of 0.3%, 1% and 2% in weight fraction were manufactured by FDM method. The filaments used for these beams were fabricated in-house with the material extrusion method. The cantilever beams were physically tested for determining the effect of nanoparticle addition on vibrational behavior regarding natural frequency and damping ratio values. Along with the

physical tests, the natural frequency values of the beams were also numerically calculated with ANSYS software for validation. The results showed that CB nanoparticle content in ABS resulted in an increase in the damping ratio of the beams compared to pure ABS beams with a maximum value obtained in 0.3wt% CB nanocomposite beams with a 39.6% increase in the damping ratio value however, it had a small influence on the natural frequency value of the beams. The $CaCO_3$ content in the matrix also provided a maximum of 11.1% increase in the damping ratio with 5wt% $CaCO_3$ content. In terms of natural frequency values, it was concluded that the addition of $CaCO_3$ nanoparticles has a limited effect on the parameter.

Keywords: Fused deposition Modeling, Natural Frequency, Damping Ratio, Nanocomposite, Free vibration

ÖZET

ÜÇ BOYUTLU YAZICIDA ÜRETİLMİŞ NANOKOMPOZİT POLİMER ANKASTRE KİRİŞİN DENEYSEL VE NÜMERİK SERBEST TİTREŞİM ANALİZİ

Sabri Can EKERER
Yüksek Lisans, Makine Mühendisliği Anabilim Dalı
Danışman: Doç. Dr. Cem BOĞA
İkinci Danışman: Doç. Dr. Turaç FARSADİ
Aralık 2022, 158 sayfa

Eriyik yığma modelleme yöntemi, tasarımda esneklik sağlaması ve tasarım aşamasından ilk üretime kadar geçen süreyi önemli ölçüde kısaltması nedeniyle imalatta kullanımını giderek artırmaktadır. Pek çok üretim yönteminde olduğu gibi, süreç bazı dezavantajlara sahiptir; bunlardan biri, yöntemin doğası gereği çoğunlukla anizotropinin neden olduğu mekanik özelliklerdeki zayıflıklardır. Bununla birlikte, bu zorlukların üstesinden gelmek için, örneğin filament hammaddesine nanopartiküllerin dâhil edilmesi gibi birçok yeni çalışma vardır. Araştırmacılar, bu nanopartikülleri dâhil ederek, eriyik yığma modelleme ile üretilen parçaların nispeten zayıf özelliklerini geliştirmeyi amaçlamaktadır. Ayrıca bu yöntemle üretilen parçaların kullanımı, hafif ama dayanıklı parça gerektiren Otomotiv ve Havacılık sektörlerinde de yerini almaktadır. Güvenilirliğin yanı sıra, bu endüstrilerde kullanılan parçaların önemli bir özelliği de titreşim davranışıdır, çünkü bu parçalar sıklıkla yoğun titreşime maruz kalırlar. Bir parça üzerinde dış kuvvetlerin neden olduğu titreşim, parçanın doğal frekansı ile çakışırsa, rezonans denilen ve yıkıcı etkilere neden olan bir olayın meydana geldiği bilinen bir gerçektir.

Bu çalışmada, ağırlık olarak %1, %2, %3 ve %5 Kalsiyum Karbonat ($CaCO_3$) nanopartikülleri içeren Akrilonitril Bütadien Stiren (ABS) ve %0,3, %1 ve %2 Karbon Siyahı (KS) nanopartikülleri içeren ABS olmak üzere iki tip nanokompozit ankastre kiriş eriyik yığma modelleme yöntemi ile üretilmiştir. Bu kirişler için kullanılan filamentler, malzeme ekstrüzyon yöntemiyle laboratuvarda üretilmiştir. Ankastre kirişler, nanopartikül ilavesinin doğal frekans ve sönüm oranı değerlerine ilişkin titreşim davranışı üzerindeki etkilerini belirlemek için fiziksel olarak test edilmiştir. Fiziksel testlerin yanı sıra kirişlerin doğal frekans değerleri de doğrulama için ANSYS yazılımı ile sayısal olarak hesaplanmıştır. Sonuçlar, ABS matrisindeki karbon siyahı miktarının sönümleme katsayısı değerlerinde olumlu etkiye sebep olduğunu göstermiş ve %0,3 karbon siyahı nanoparçacık içeriğinin, sönüm oranı değerinde %39.6'lık bir artış sağladığını göstermiştir. Bununla birrlikte doğal frekans değerinde çok az değişimler tespit edilmiştir. Matristeki $CaCO_3$ içeriği, ağırlık yüzdesindeki her artış için sönümleme oranı değerlerinde küçük artışlara neden olmuştur ve maksimum artış %5 $CaCO_3$ katkılı ankastre kirişte %11.1 olarak kaydedilmiştir. Doğal frekans değerleri açısından $CaCO_3$ nanoparçacıklarının eklenmesinin parametre üzerinde çok sınırlı bir etkiye sahip olduğu sonucuna varılmıştır.

Anahtar Kelimeler: Eriyik Yığma Modelleme, Doğal Frekans, Sönümleme , Nanokompozit, Serbest Titreşim

Dedication

To my precious family.

ACKNOWLEDGEMENTS

I would like to express my deepest appreciation to my supervisor Assoc. Prof. Dr. Cem Boğa for making this work possible with his continuous support and encouragement. His infinite patience and determination kept me pursuing the better in every stage of this study. I would also like to thank my co-supervisor Assoc. Prof. Dr. Turaç Farsadi for supporting me with my thesis. I am also grateful for the guidance of Asst. Prof. Dr. Mirsadegh Seyedzavvar for his assistance with this study. Additionally, this undertaking would not have been possible without the generous support from the Adana Alparslan Türkeş Science and Technology University Department of Scientific Research who financed my research.

I would like to thank my lovely wife for supporting me through this undertaking patiently and making my life easier through the long hours of work. I deeply appreciate the presence of my daughters whom I hopefully can inspire them with my hard work. Lastly, I would like to thank my parents and especially my mother who believed in me for all these years who always supported me along with my sister. I would also like to thank all my teachers who inspired me through my educational journey so far.

This thesis was financially supported by Adana Alparslan Türkeş Science and Technology University Department of Scientific Research Projects with project number 21303013.

İÇİNDEKİLER

LIST OF FIGURES

LIST OF TABLES

LIST OF ABBREVIATIONS

$CaCO_3$	: Calcium Carbonate
AM	: Additive Manufacturing
FDM	: Fused Deposition Modeling
CB	: Carbon Black
STL	: Standard Tesselation Language
ABS	: Acrylonitrile Butadiene Styrene
PLA	: Poly lactic acid
DED	: Directed Energy Deposition
CNC	: Computerized Numerical Control
3D	: Three dimensional
PC	: Polycarbonate
PEEK	: Polyether ether ketone
PEI	: Polyetherimide
PETG	: Polyethylene terephthalate glycol-modified
HIPS	: High-impact polystyrene
TPU	: Thermoplastic polyurethane
SEM	: Scanning Electron Microscopy
EMI	: Electromagnetic interference
MWCNT	: Multiwall Carbon Nanotubes
GO	: Graphene oxide
OMMT	: Organically Modified Montmorillonite
ATO	: ABS Tin Oxide
PPR	: Polypropylene Random Copolymer
CNF	: Cellulose Nanofibers
CNT	: Carbon Nano-tube
FFF	: Fused Filament Fabrication
FFT	: Fast Fourier Transformation
LED	: Light emitting diode
FE	: Finite Element

COF	: Coefficient of Friction
ANOVA	: Analysis of Variance
PA66	: Polyamide 66
FE	: Finite Element
ANN	: Artificial Neural Network
FESEM	: Field Emission Scanning Electron Microscope
ANOVA	: Analysis of Variance
PA66	: Polyamide 66
FE	: Finite Element
ANN	: Artificial Neural Network
Fe	: Iron
Cu	: Copper
ZnO	: Zinc Oxide
TiO_2	: Titanium Dioxide
Sb	: Antimony
SnO_2	: Doped Tin Oxide
BN	: Boron Nitride

LIST OF SYMBOLS

$CaCO_3$	: Calcium Carbonate
F	: Force
k	: Spring Constant
x	: Displacement
c	: Damping Constant
v	: Velocity
m	: Mass
$u(t)$	: Displacement
$\dot{u}(t)$	: Velocity
$\ddot{u}(t)$	: Acceleration
f_s	: Elastic resisting force
$p(t)$	: External force
f_D	: Damping resisting force
ω_n	: Natural frequency in rad/sec
T_n	: Natural period
f_n	: Natural frequency in hertz
E	: Modulus of elasticity
I	: Moment of inertia
t	: Time
L	: Length
c_{cr}	: Critical damping coefficient
ζ	: Damping ratio
ω_D	: Damped natural frequency in rad/sec
T_D	: Natural period of damped vibration
t	: Time
ρ	: Density
e	: Mathematical constant e

1. INTRODUCTION

From the early days of the industrial revolution to today's era of industry 4.0, manufacturing technology is still in progress carrying on with its journey of technological evolution. The way goods are manufactured constantly changes, adapting to environmental, technological, or financial circumstances in terms of concept design, production methods, and tools. The adaptation to these various conditions has led to the development of many different manufacturing processes and techniques. The development of new materials suitable for individual manufacturing processes goes hand in hand with the research carried out on the development of manufacturing processes itself. This ongoing process of development in these manufacturing processes and materials is undoubtedly driven by scientific research that helps build up knowledge on top of each research effort made. Academic researchers bear the responsibility of expanding the capabilities of newly introduced technologies and foreseeing new areas of development that may take their place at the forefront of technological enhancement. These efforts result in the manufacturing of more efficient, cheaper, and advanced goods served to millions of customers around the world affecting every nation. With the advancements made in communication and transport technologies, the world is much smaller than ever, bringing many challenges and opportunities in every aspect of life, especially in the manufacturing of goods. Consequently, every research that contributes to the development of manufacturing technology in terms of processes or new materials adapted to a process might have a considerable impact on future research and consequently impact the goods placed on the global market for consumers.

Additive Manufacturing (AM) is one of the emerging manufacturing processes that is recently getting attention for research through the development of the process and the employment of new materials. The use of nanoparticle additives in the raw materials of AM processes creates new composite materials to be employed in the process. This is a new trending topic in the AM process studies for the enhancement of certain properties of parts produced with the AM method. This study aims to investigate the vibrational properties of a cantilever beam manufactured by AM method which has a nanoparticle-enhanced material composition. The effect of nanoparticle content on the vibrational characteristics of the composite material produced with AM method was evaluated along with other parameters of the process. As nanoparticles, Calcium Carbonate ($CaCO_3$) and Carbon Black (CB) was separately incorporated with Acrylonitrile Butadiene Styrene (ABS) matrix material and nano-composite filaments were fabricated. Cantilever beam specimens were 3D printed with these filaments in order to carry out vibration tests. Natural frequency and damping ratio values were obtained. Tensile tests were also carried out in order to calculate the natural frequency values numerically.

This study is unique in the way that free vibration characteristics of a 3D printed ABS + CB and ABS + $CaCO_3$ Nanocomposite parts were investigated and the effect of the Nanoparticle content in weight fraction was evaluated. It is believed that this study will contribute to the literature with its findings.

1.1. Additive Manufacturing Process

The various manufacturing processes developed until now, as mentioned previously, can be classified differently by using various methods considering distinct aspects and features of the processes. A technology-based categorization of manufacturing processes was proposed in a study [1] which can be seen below;

- Joining Technology: This method utilizes operations involving the joining of two or more parts to fabricate a new part. Examples of the method can be specified as welding of parts and fastening of different parts with bolts and nuts.
- Dividing Technology: This technology can be expressed as a contrasting version of the joining technology. Cutting a work piece into two separate parts is the most common example that can be given to express this technology.
- Subtractive Technology: This technology follows the principle of removing material from the base part to manufacture the final product. Metal cutting, milling, and turning are perfect examples of this manufacturing technology.

- Transformative Technology: A wide range of operations can be included in this category as long as the mass of a solitary part is not changed and transformed into a new part. Sheet metal forming and heat treatment are common methods used in this category.
- Additive Technology: Additive technology is the process of material addition, generally in terms of layers by layer, to form a work piece from scratch or to an existing part. It embodies various methods such as; Fused Deposition Modelling, Selective Laser Sintering, Powder Bed Fusion, and Stereolithography.

When these manufacturing technologies are categorized according to the above perspective, it becomes easier to comprehend the distinguishing features of AM technology. To be more precise, we should dive deeper into the definition of AM. AM process is a relatively new process of fabrication that was intended for building parts by forming successive thin layers of material in conformity with the three-dimensional (3D) Computer-Aided Design (CAD) model representing the final product. This layer-wise approach uses the 3D CAD data and transforms the whole body of the designed product into thin layers added on top of each other. The direct production of the part in one step is enabled when AM method is used without any extra operations such as machining that is used in conventional subtractive manufacturing methods. With the advantages of a rapid and flexible design process, AM technology also reduces production time in scenarios where small amounts of unique parts are requested from the costumers. Another main advantage of the AM process is that thanks to its contrary approach to subtractive manufacturing, it is relatively effortless to produce parts having complicated geometries [2]. AM during the process contrary to subtractive manufacturing is illustrated in Figure 1.1.

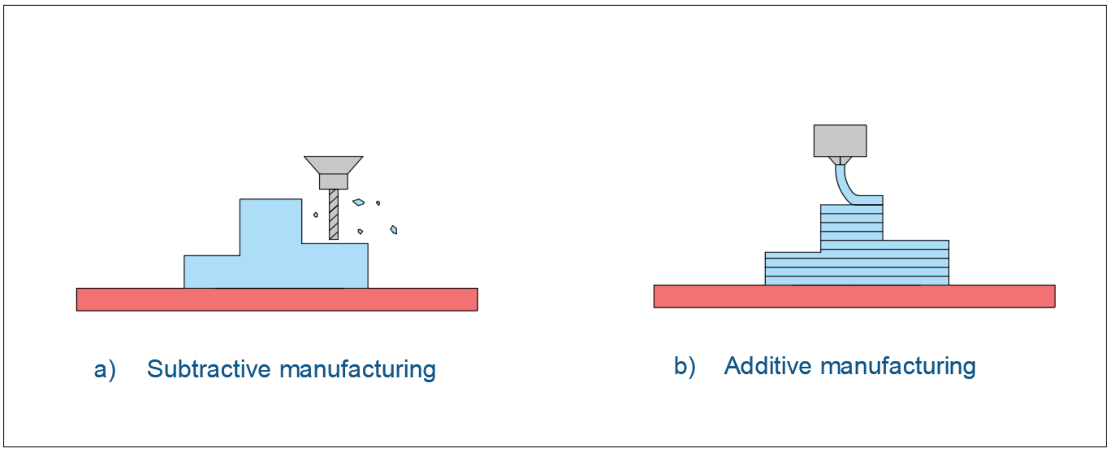

Figure 1.1. Illustration of a) Subtractive manufacturing b) Additive manufacturing

The flexible nature of AM technology allows it to find application in a wide range of industries such as energy [3], aerospace [4], and even dentistry [5]. Possessing the mentioned advantages AM technology has some downsides such as the limited dimensions of the manufactured part, the anisotropic behavior of the manufactured part due to the layer-wise deposition of the material, and the long periods that take in the production of the part. We need to clarify the production time concept to avoid any confusion since it should be stated that the time that takes to build a part is relatively longer compared to other manufacturing methods however when we think about the time that is spent on the overall design, preparation and post-processing of a part it takes much less time if AM technology is preferred. AM technology employs various techniques of fabrication where different materials are adopted along with the use of miscellaneous physical principles. The processes of AM technology can be divided into seven distinct methods and classified as below [6];

- Vat Photopolymerization
- Material Jetting
- Binder Jetting
- Fused Deposition Modelling (Material Extrusion, Fused Filament Fabrication)
- Powder Bed Fusion
- Sheet Lamination
- Directed Energy Deposition

1.1.1. Vat Photopolymerization

In this AM method, a photopolymer in liquid form is placed in a vat and it is selectively activated by a light source in a certain wavelength to be polymerized. In other words, the photopolymer is in the form of a resin that can be cured by interacting with a light source of either visible form or in the form of a UV spectrum. The light starts and the reaction that causes the curing process forms polymer chains which solidify the liquid resin. This process is irreversible and once solidified, the part does not return to its liquid state. This principle is employed to form layers of solidified resin according to the Standard Tesselation Language (STL) file with slices that are generated by using the original model. The process of photopolymerization is categorized according to the type of curing such as Stereolithography (SLA) which uses lasers, digital projection (digital light processing (DLP)), a method that employs light-emitting diodes for curing (LED) and a method that uses oxygen which is called continuous digital light processing (CDLP) or continuous liquid interface production (CLIP). SLA is the most commonly known method among the mentioned techniques and it uses a platform that is submerged in a tank that has light permeability. The tank, which is called the vat, is filled with liquid resin and when the platform is submerged in the tank the laser beam traces the path generated according to the STL file and forms a layer. After a layer is completed the platform moves out of the resin bath in the z direction and waits for the curing to complete and submerges in the tank again to form the consecutive layers. The platform is either placed top-down or bottom-up according to the design of the machine [7]. The illustration of an SLA machine can be seen in Figure 1.2.

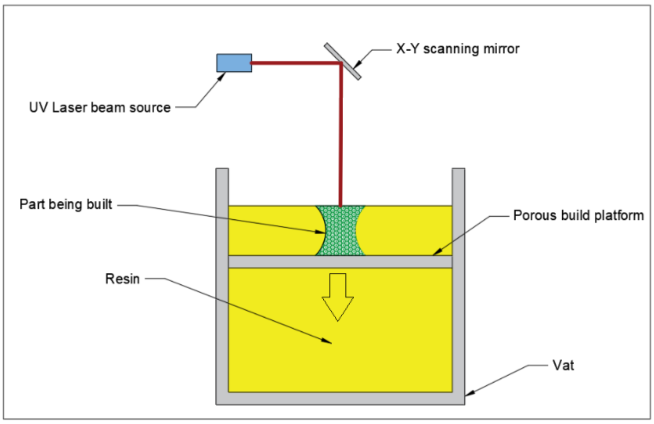

Figure 1.2. Working principle of the SLA process

1.1.2. Material Jetting

Material jetting is a remarkable AM method compared to other polymer printing techniques because it enables users to produce parts having high surface quality thanks to its ability to create very thin layers. It is possible to obtain parts with thin walls and produce parts with low surface roughness. The principle of the method is to deposit liquid polymer material through the printing nozzle jetting it on the build platform and cure the material with light to complete a single layer. The final product is manufactured with consecutive layers formed according to the STL file. The jet nozzle can move along the x-y axes and the platform can move along the z direction after the creation of each layer [8]. The process of material jetting can be seen in Figure 1.3.

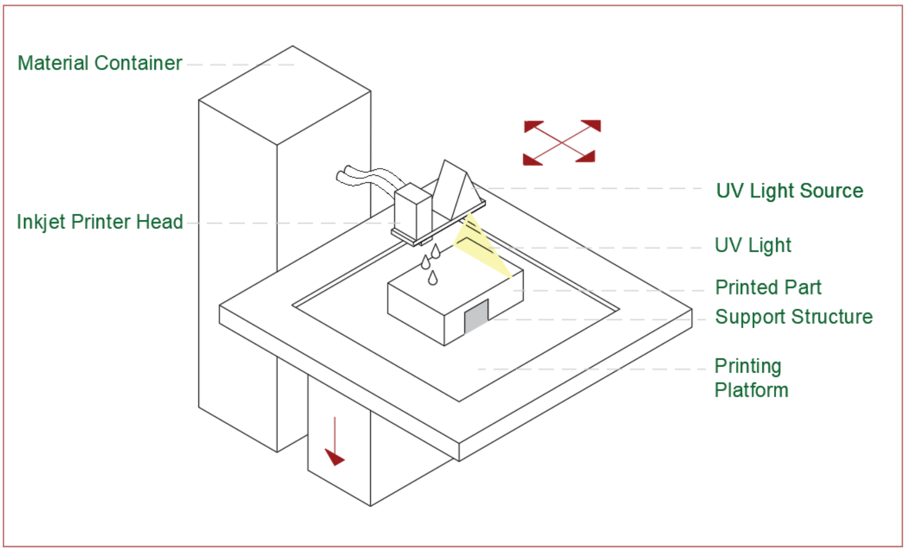

Figure 1.3. Illustration of material jetting process

1.1.3. Binder Jetting

A different approach is employed in this AM method which in principle utilizes a binder material that is used to bind the feedstock material in the form of powder. A printing nozzle deposits the mixture of powder material and liquid binder in the form of jetting action on the powder bed filled with feedstock material in powder form. The binder solidifies the materials forming a layer. Once a layer is created according to the sliced STL model, the printing platform is lowered and a powder dispenser moves horizontally across the platform to deposit the powder on the new layer to be created. The unbounded powder material stays in the powder bed during the process serving as a support structure and after the completion of the process, the unused powder can be reused for other printing sessions. The process might need some post-processing to obtain desired properties [9]. The binder jetting process is illustrated in Figure 1.4.

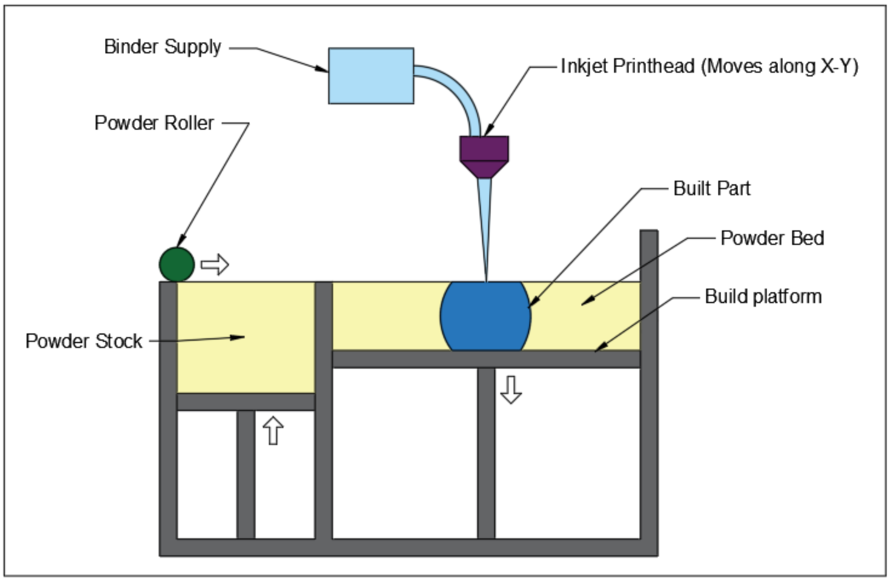

Figure 1.4. Illustration of binder jetting process

1.1.4. Powder Bed Fusion

This method has a common feature with the Binder Jetting method where both methods employ the use of a feedstock material in powder form. The difference is the method of binding and this technology is based on the use of lasers as a means of binding the powder material. The process employs a laser beam that scans the surface of the powder bed along certain coordinates and binds the powder material to the solid material underneath using fusion. If the fusion is obtained by full melting it is called Selective Laser Melting (SLM) and if the fusion is attained by partial melting the process is called Selective Laser Sintering (SLS). After the completion of each layer, the powder bed is moved in a negative z direction according to the determined layer thickness and new powder is spread evenly over the build platform in order to form the consecutive layer. This process is rerun until the part production of the part is completed. An example illustration of an SLS system is illustrated in Figure 1.5.

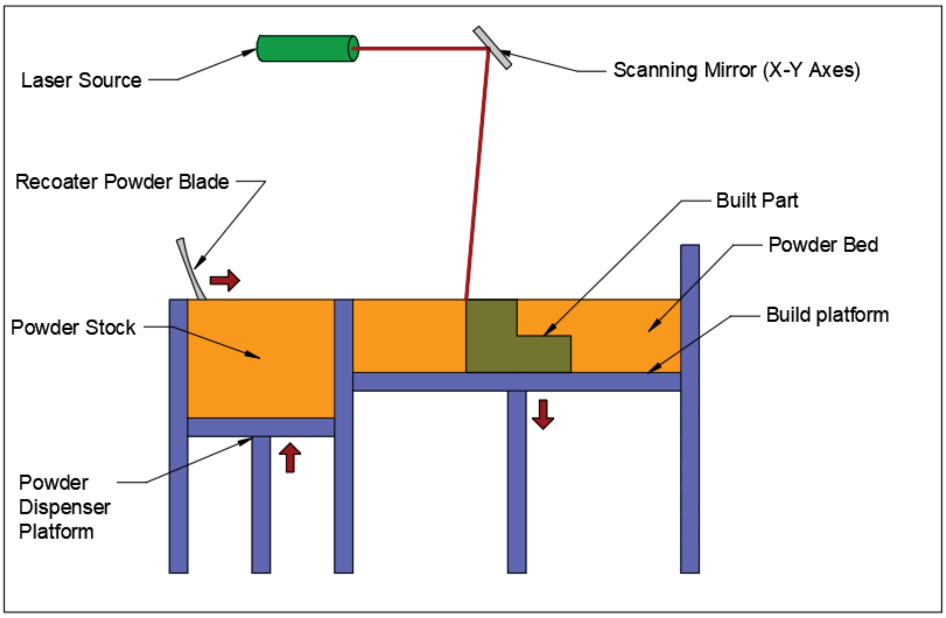

Figure 1.5 Illustration of powder bed fusion process

1.1.5. Sheet Lamination

Though inheriting the same principles, many techniques of Sheet Lamination exist and it is possible to fabricate parts using many different types of materials such as metal, ceramic, polymer, and paper. The technique was first used in manufacturing objects by combining layer-by-layer paper sheets. The paper layers were cut with the help of a CO_2 laser to form the determined layer of the part and each laminate was bonded on top of the other. Later the technology was used to bind other materials with the help of the development of new processes. The most recent material used in this method is metal and sheets of metal are bound to each other with the principle of ultrasonic welding technique which is called Ultrasonic Additive Manufacturing (UAM). The technique is a combination of CNC milling and ultrasonic seam welding. The method uses a rotating sonotrode which travels on the thin metal laminate both applying a downward force on the metal foil and using ultrasonic waves to bind the foil to the layer underneath. Generally, four foils of metal are bonded adjacent to each other which is called a level and for every level, the CNC milling tool cuts the metals to form the shape of the layer. This process repeats until the part is manufactured [2]. An illustration of the UAM method can be seen in Figure 1.6.

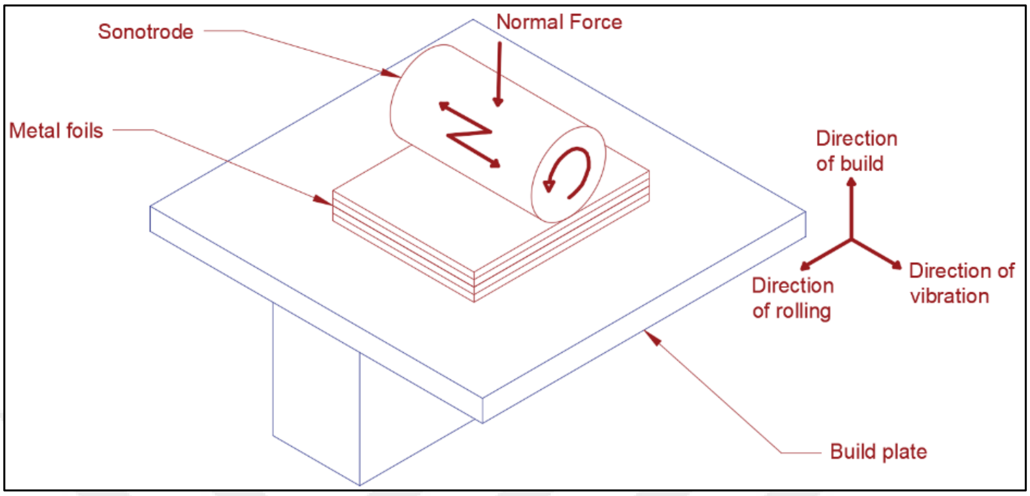

Figure 1.6. Illustration of the sheet lamination process

1.1.6. Directed Energy Deposition

Directed Energy Deposition (DED) method melts the material while it is being deposited to create the respective layer of the final product. This is contrasting with the powder bed fusion method since the powders are melted after being placed on the build platform. Many materials such as polymers, ceramics, and metal can be used in this technique however the method is more widely used for the fabrication of metal or metal matrix composite materials. The heat source that is used for the melting process of the powder feed stock material is a laser or electron beam. In some applications, the feedstock material is in the form of metal wires. The process resembles CNC milling machines or sometimes can be adopted to CNC milling machines since the movement of the deposition head is enabled by electric motors controlled by computer software where 3-axis, 4-axis, and 5-axis movements are possible according to the DED machine design. A DED machine's working principle is illustrated in Figure 1.7.

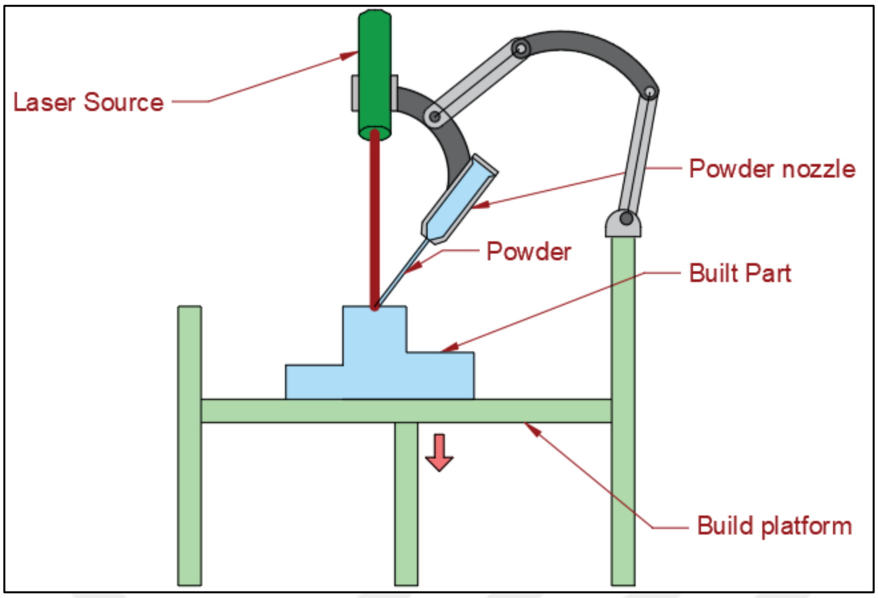

Figure 1.7. Illustration of the directed energy deposition process

1.1.7. Fused Deposition Modelling

Fused deposition modeling (FDM) is the most widely used AM technology thanks to its relatively low cost and accessible equipment, making it even possible for home users to practice the technology. The FDM method utilizes polymers as raw material in a melt extrusion process of depositing the material on top of each sequential layer. Various polymers are employed as raw materials such as Acrylonitrile Butadiene Styrene (ABS), Polypropylene (PP), and Poly Lactic Acid (PLA) [10]. Since the polymer raw material must be melt extruded in this process, the feedstock must be in the form of an extruded wire wound on a reel which is called the filament. Many types of filaments composed of various polymer materials are available on the market to be used in the FDM equipment also known as 3D printers. A polymer filament used for the FDM method is seen in Figure 1.8. A feeding mechanism that transports the filament to the printer head is used in the FDM process and the printer head then melts the material with the use of a heater to deposit the molten material on the build platform through a nozzle. (Figure 1.8.)

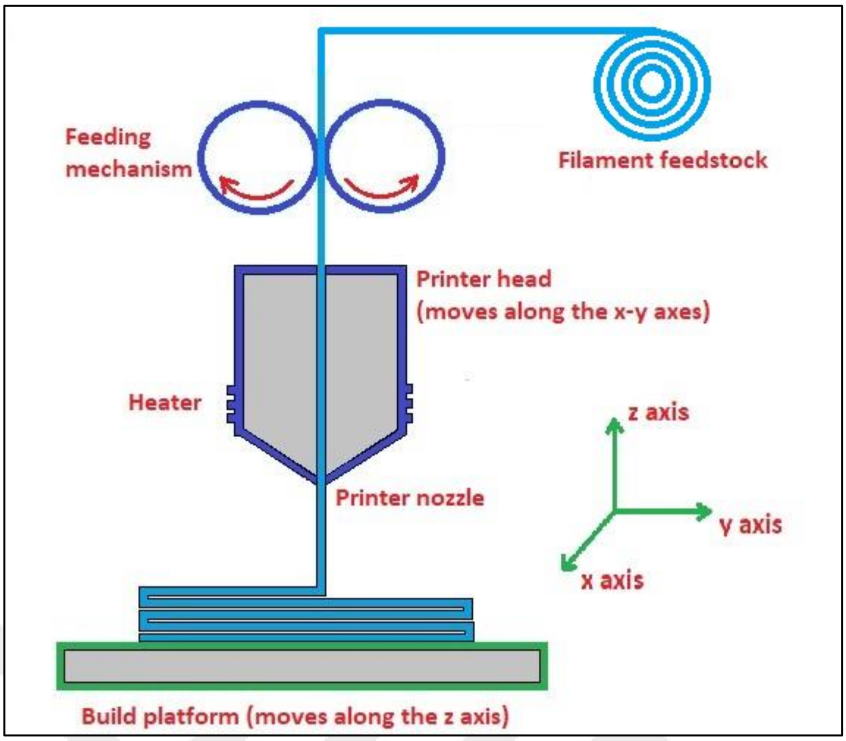

Figure 1.8. Illustration of the fused deposition modeling process

The extruder is capable of traveling in the x and y axes so that it can deposit material as required for the fabrication of each subsequent layer and once a layer is complete the build platform changes its position in the z-axis to create the next individual layer of the part to be produced. For the creation of every single layer, the CAD model data needs to be converted to a Standard Tessellation file (STL) format, and the STL file data is processed by software that creates the geometry of the layers. This pre-processing step is carried out by considering some parameters called printing parameters predetermined by the operator of the 3D printer. Following the layer creation, the tool path of the extruder head should be determined for the deposition of the material, and for this the software generates G codes. According to the generated tool path, the extruder head is programmed to move and deposit the material following the G codes created and production of the model gets completed [11]. The production process of the FDM method is illustrated in Figure 1.9.

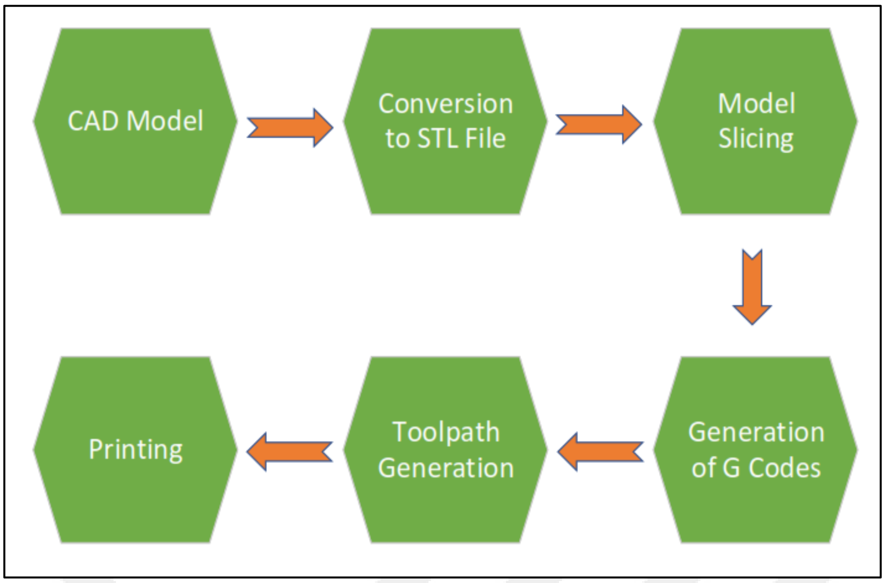

Figure 1.9. Overall process steps of fused deposition modeling

In the FDM process, one of the most important phenomena that affect the properties of the fabricated part is the selection of the process parameters. Also known as printing parameters; these parameters can be described as the input variables that drastically affect the various properties of the fabricated part such as mechanical properties, surface roughness, dimensional accuracy, and wear. Below are some of the various printing parameters employed in the fabrication of a part [12] ;

- Layer Thickness: It is the height/thickness (z-direction or vertical axis) of the deposited filament material that has just been extruded from the printing nozzle.
- Build orientation: The positioning of the part (orientation) on the build platform aligned along the X-direction, Y-direction, or Z-direction of the 3D printing equipment.
- Raster Angle: The deposition angle of the extruded material relative to the X-axis of the build platform, generally this angle is between 0 to 90 degrees.
- Air Gap: The relative distance between two deposited materials on their toolpath during the fabrication of a single layer.

- Extrusion Temperature: The temperature reached in the heater to melt the filament material in the extruder before deposition. Depends on the material to be used and the printing speed parameter.
- Printing Speed: The speed at which the extruder nozzle moves about the XY axes of the build platform during deposition.
- Infill Pattern/Infill Geometry: The geometry of the deposited material that forms the internal structure of the part fabricated by the FDM method. Common geometrical shapes used are line, triangle and hexagon.
- Infill Density/Infill Percentage: Although 3D printed parts' outer surfaces are solid the internal structure inherits a certain amount of void depending on the infill geometry and infill percentage. Therefore, this parameter determines how solid the internal structure of the part is.
- Nozzle Diameter: The geometric diameter dimension of the extruder nozzle.
- Raster Width: The width of a thin continuous line (bead) of deposited material along the toolpath belonging to the printed part on the build plate. Raster width relies upon the nozzle diameter.
- Number of Contours: Among all the deposited beads the outer layers of a 3D printed part are solid and they are called contours.
- Contour Width: The dimensional thickness of the contour beads that circumscribes the inner beads.
- Contour to contour air gap: The distance of the void between parallel contours surrounding the inner structure.

There are numerous parameters incorporated with the 3D printing of a part. Some parameters both affect the toolpath geometry determination directly and also affect the mechanical strength of the part indirectly. When a part is printed the material is deposited in a unique path taking into account some of the mentioned printing parameters. While some parameters directly affect the density of the printed part, others affect the surface roughness of the fabricated part. Illustration of parameters related to toolpath such as raster angle, air gap, raster width, contour width, number of contours, and contour to contour air gap can be seen in Figure 1.10.

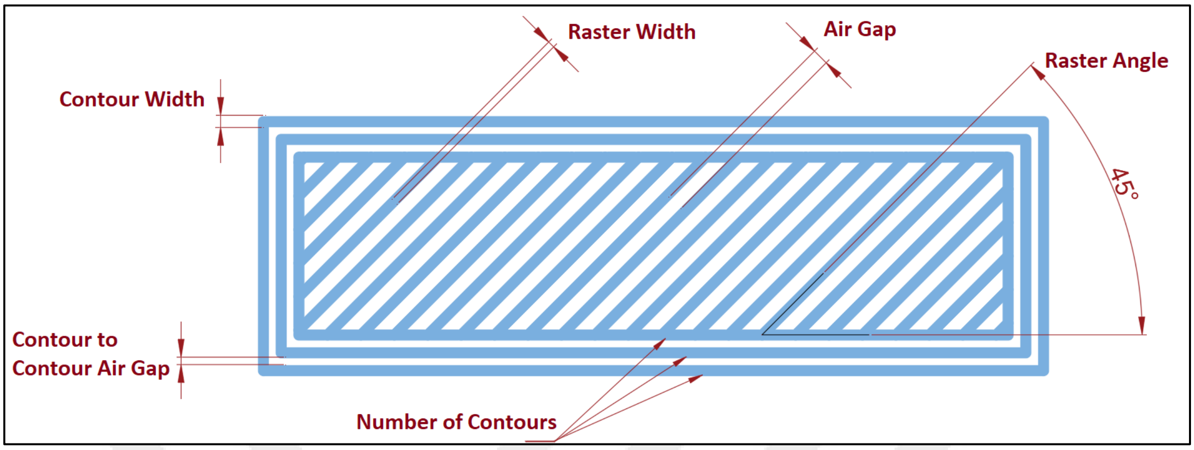

Figure 1.10. Parameters affecting tool path in FDM

The most commonly used infill geometry types are line, triangle, and hexagon which are illustrated in Figure 1.11. As can be seen in Figure 1.11, as the infill density increases the size of the infill geometrical shapes decrease which shows that these parameters are interdependent.

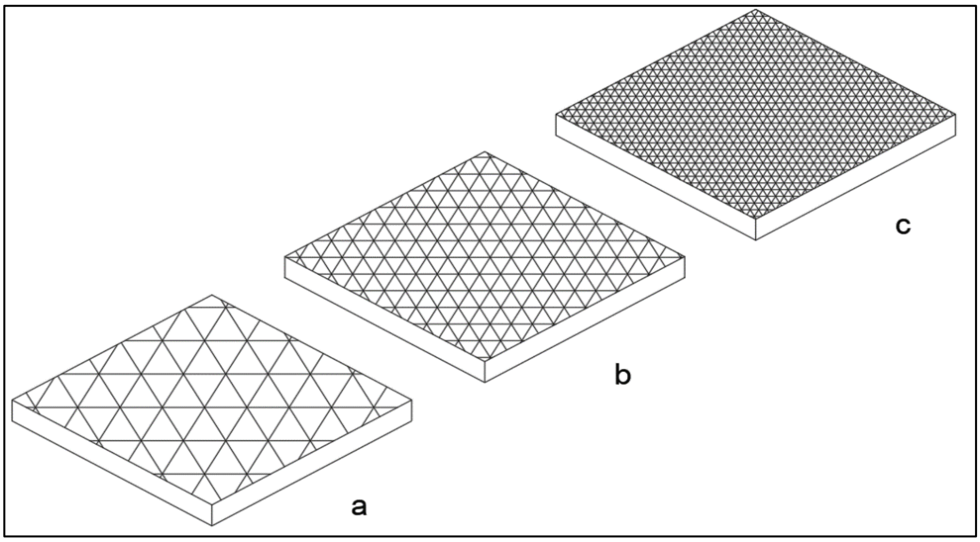

Figure 1.11. Varying infill percentage values of (a) 25% infill density, (b) 50% infill density, (c) 75% infill density for triangular geometry

One of the process parameters affecting build-time is layer thickness, which is shown in Figure 1.12. As layer thickness increases build time shortens and vice versa.

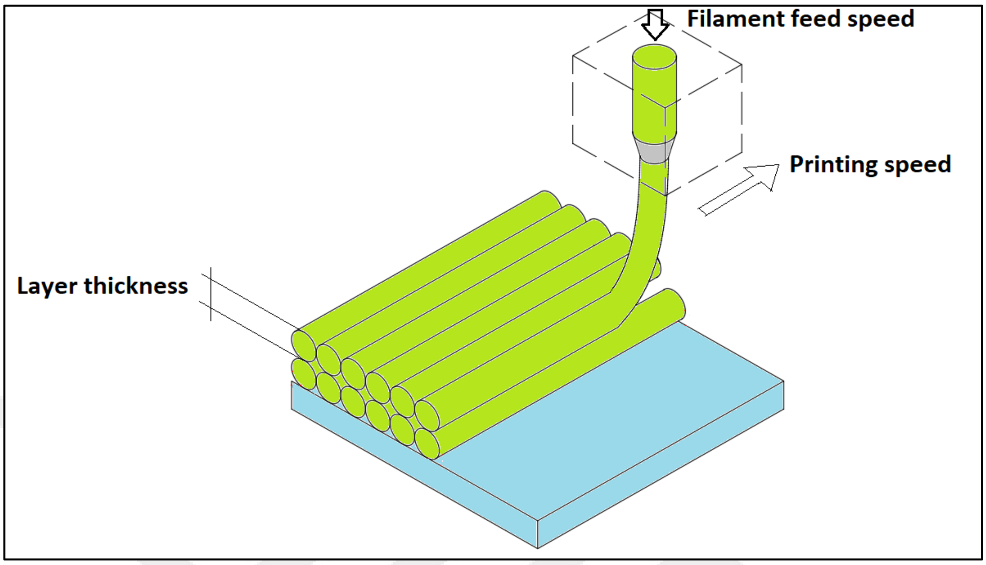

Figure 1.12. Representation of the layer thickness, printing speed, and filament feed speed

Another important parameter is build orientation which affects the mechanical properties and other process parameters should be determined in conformity with this orientation to get the optimum results. Possible build orientation options of a part can be seen in Figure 1.13.

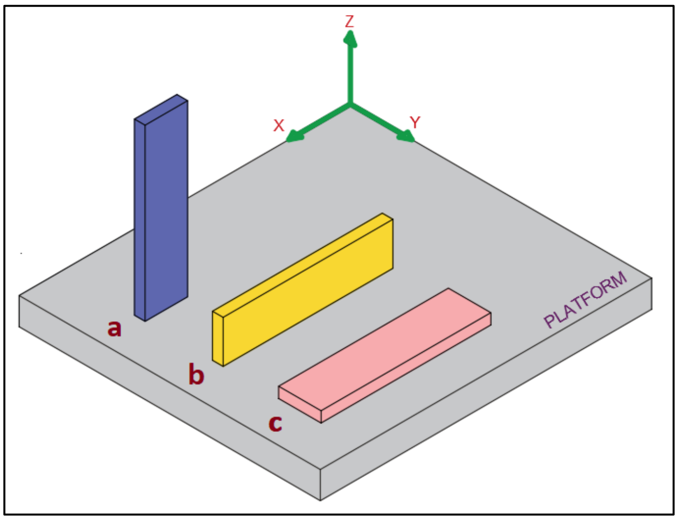

Figure 1.13. 3D Printing of the same part with three different orientations a) Upright b) On edge c) Flat

The build orientation of the part has a significant influence on the mechanical properties of the part that is 3D printed. The 3D printed part may behave brittle or ductile depending on the build orientation [13]. When a part is to be fabricated, many factors and parameters should be assessed along with the build orientation. When the build orientation is determined, it should be considered that the part geometry may limit the deposition of the materials layer by layer on top of each other for a specific build orientation. This issue may be dealt with by adding a supporting structure that has the function of carrying a load of some layers to complete the upper layers to finish the part fabrication. By doing so it should be considered that the build time will take longer since more material deposition is involved with the additional support structure. Another issue with the support structure is that the removal of the structure also takes time and the surface quality of the original part that the support was removed from sometimes gets negatively affected and additional post-surface processing may be required [14]. When a part is printed with a support structure generally a double extruder is used, one for the main part material deposition and the other for the support structure. Generally, a similar material to the main part material is used for the support material, or an easily dissolvable material like PVA is chosen [13]. In Figure 1.14, a part 3D printed with a support structure by a double extruder printer is illustrated.

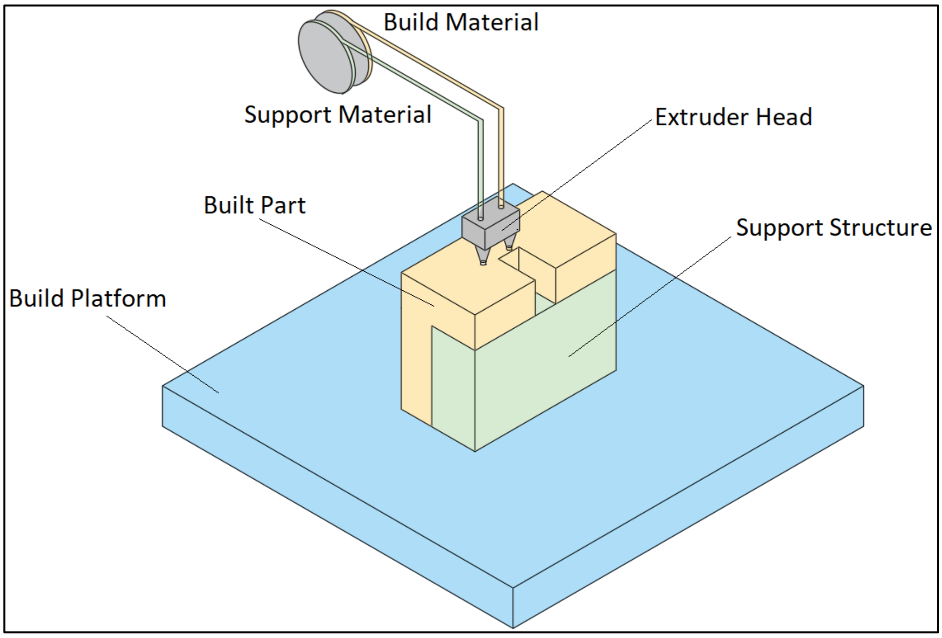

Figure 1.14. Part 3D printed with support structure utilizing two extruders

The deposition of the material on top of each other layer by layer causes the formation of some defects between the layers and this negatively affects the mechanical properties as well as the surface roughness of the built part. This phenomenon is called the ‘’staircase effect’’ and this is generally dependent on the layer thickness [15]. It is important to consider these defects if a part will be subject to certain forces in its use when deciding the build orientation. It is important to assess factors like surface quality, and strength, and build time together in deciding whether a certain orientation is suitable or whether a support structure is necessary or not.

As mentioned earlier FDM utilizes filaments of various materials and melt extrudes these materials to form the layers of the printed part. The filament is wound on a reel, placed in a reserved space in the printing machine, and with the assistance of a feeding mechanism it is transported to the extruder nozzle.

In the FDM process, generally pure thermoplastic materials are used a s filament material. A wide range of thermoplastics is available on the market. Filament extruders are used for the production of FDM filaments. For the production of FDM filaments, thermoplastics are purchased in the form of granules or pellets to be used as raw materials. The granules are fed to a filament extruder through a hopper that conveys them to a screw mounted in a barrel and rotated by an electric motor. An extruder may possess one or two screws in the assembly for different filament fabrication techniques. The granules are melted by a heater on their way through the screw in reaching the nozzle at the end of the die. The extruded molten filaments are cooled with a specific cooling system generally a water-cooling bath or air-cooling system.

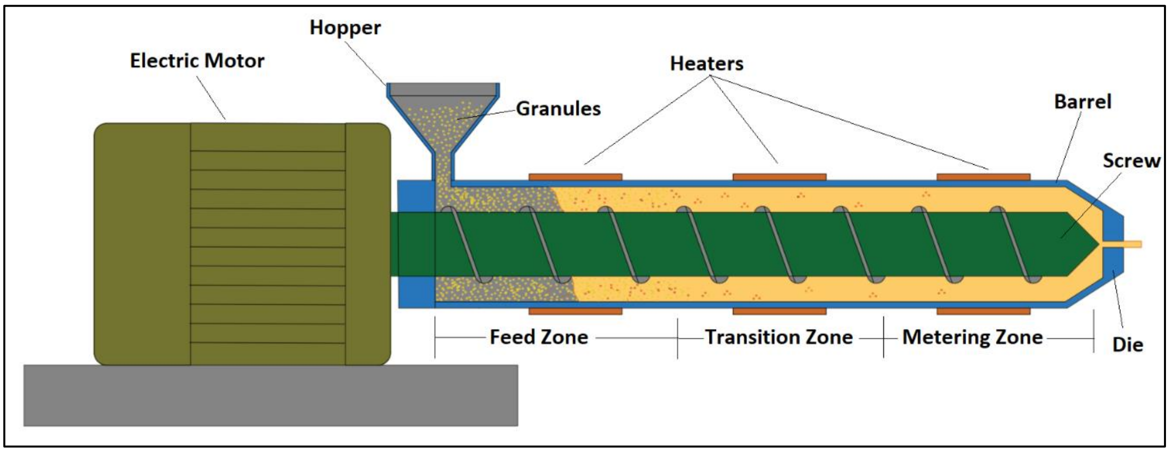

Figure 1.15 Filament extruder machine

An illustration of a single screw extruder can be seen in Figure 1.15. To fine-tune the filament diameter adjustment a drawing mechanism is used and the drawing speed can be altered for proper adjustment. There are a wide variety of different thermoplastics available in the industry, each having different properties making them suitable for use in different applications in 3D printing. Every thermoplastic material is preferred for its unique characteristics such as tensile strength, heat resistance, biocompatibility, and flexibility suitable for the intended application [16].

Pure thermoplastic filaments used for the 3D printing of parts are readily available on the market with a wide range of different brands and price spans. Although newer materials are being tested for the development of filaments with better properties, the most widely used filament materials available on the market today can be listed as follows;

- ABS
- PLA
- PC
- Polyether ether ketone (PEEK)
- Polyetherimide (PEI)
- Nylon
- Polyethylene terephthalate glycol-modified (PETG)

- High-impact polystyrene (HIPS)
- Thermoplastic polyurethane (TPU)

The most frequently used filament materials among the list above in the 3D printing industry are ABS and PLA.

1.1.7.1. Polycarbonate

Polycarbonate (PC) is a thermoplastic polymer known for its good mechanical properties and thanks to its suitable dynamic properties it is being used in the Automotive industry. It has transparent properties due to its amorphous internal structure therefore it is being used in medical and optical applications as well [17]. It has a tensile strength value between 58.6 – 72 MPa, a Young Modulus value between 1.79–3.24 GPa, it has an extrusion temperature value between 200–280 ^{o}C and it is not biodegradable[18].

1.1.7.2. Polyether ether ketone

Polyetheretherketone (PEEK) is a thermoplastic that has good thermal and chemical resistance properties. It inherits outstanding mechanical properties with a tensile strength of 100 MPa. Having an extrusion temperature between 340 – 440 ^{o}C which is one of the highest temperatures among most polymers used in FDM. It has a Young Modulus value between 3.56–4.00 GPa and it is not a biodegradable substance [18].

1.1.7.3. Polyetherimide

Polyetherimide (PEI) is a thermoplastic known for its good thermal, chemical, and mechanical stability properties. Despite its lightweight structure, it has relatively good mechanical properties. This strength-to-weight ratio advantage gives it an advantage in Automotive and Aerospace applications [19]. With its biocompatible properties, it is also used for bone tissue reinforcement in the medical field. A mixture of PEI and PC also has a commercial brand name called ULTEM. The addition of PC enhances the filaments' capacity to flow during extrusion.

1.1.7.4. Nylon

Nylon is a polymer that has a reputation for its flexible nature, ability to resist heat, and impact-resisting features. It has good durability properties and performs well regarding toughness characteristics. Due to its hygroscopic properties, it tends to absorb moisture which adversely affects the part quality. Nylon parts tend to warp after the printing process and the amount of warpage can be diminished by providing a 75 ^{o}C printing bed temperature [16].

1.1.7.5. Polyethylene terephthalate glycol-modified

It is a thermoplastic derived from Polyethylene Terephthalate (PET) which we use as plastic water bottles in daily life. It is modified with Glycol and became PETG to be used in the FDM process. It is durable to an extent, flexible, and soft compared to PLA and ABS. Its extrusion temperature is between 220 to 250 ^{o}C and has a Tensile Strength of 49 MPa. It is mainly used in the food packaging business and implants in medicine [17].

1.1.7.6. High impact polystyrene

High-impact polystyrene (HIPS) is a polymer that is biodegradable and it has rather low strength but good machinability properties. It has low cost, good flow characteristics, and good impact resistance [20]. HIPS is prone to warp and needs a heated printing bed during the process. It is soluble in limonene and therefore is suitable for use in support structures of another filament material. It is also biodegradable making it more friendly to the environment.

1.1.7.7. Thermoplastic polyurethane

Thermoplastic Polyurethane (TPU) is a polymer having outstanding hardness characteristics along with perfect wear and tear resistance properties. It has good flexibility properties and it is corrosion-resistant to most chemicals and oils used in the industry. It is used in a wide range of industrial applications since it shows versatility in terms of rubber and plastics behavior [19].

1.1.7.8. Poly lactic acid

Polyl actic acid (PLA) is a biodegradable thermoplastic with a lower melting temperature compared to ABS which results in less energy consumption for the 3D printer when PLA is used instead of ABS. It offers good quality in finished parts with a little bit of post-processing being required. Compared to ABS PLA filaments are more likely to jam extruder nozles compared to ABS filaments. PLA filaments offer greater tensile strength, low warpage, and lower ductility when compared to ABS filaments [21].

1.1.7.9. Acrylonitrile butadiene styrene

ABS is a copolymer composed of acrylonitrile, butadiene, and styrene. It is a petroleum-based thermoplastic having good mechanical properties such as impact resistance and toughness. It is a strong material and it is being used widely in the automotive, aerospace, and medical sectors [19]. It has a non-biodegradable amorphous structure with a melting point of 230 degrees and when used for 3D printing the extrusion temperature is between 220-280 ^{o}C. It has a tensile strength between 13-65 MPa and a Young modulus value between 1-2.65 GPa [18]. ABS has a lesser tendency of clogging the printer nozzle. ABS also inherits the drawback of warping in parts after the 3D printing process.

Though much research is being carried out to understand the behavior of 3D printed parts fabricated with various thermoplastic materials or the blend of two or more thermoplastic filament materials, recent studies also focus on the development of nanocomposite filament materials and their properties. This topic, which is the main concern of this study, will be discussed in the next section of the thesis.

The developments in AM technologies including the FDM method serve as a solution to the contemporary needs of manufacturing in many facets of the industry. As we are gradually entering an era of Industry 4.0 and the Internet of Things, the manufacturing industry is evolving with the capabilities of these new technologies and at the same time, it adapts to global events that take place such as the pandemic which had a drastic impact on the global supply chain. AM is changing the conventional understanding of how goods are distributed. This was demonstrated during the Covid 19 pandemic when the supply chain was adversely affected causing difficulties in the procurement of certain goods including medical equipment. The use of AM technology offered a quick response strategy with the ability to fabricate some products at home providing independence from suppliers abroad [22]. Although the volume of products fabricated by FDM technology is limited today, this experience strongly encourages the use of the technology and supports the notion that the growth potential of the technology is promising for the future. Apart from the global supply chain and distribution aspects, FDM technology has key potential in terms of the environmental aspects of the manufacturing processes in general. As stated earlier AM technology is a direct manufacturing method as opposed to subtractive manufacturing methods which require additional operations such as machining and grinding. The more the number of operations, the more energy is consumed increasing the emission of harmful gases. AM technology also offers the advantage of significantly reducing waste material compared to subtractive manufacturing. The combination of the mentioned advantages leads to the potential reduction of time and cost for special parts produced in small volumes. In the future AM, technology has the great potential to be dominant in niche fields of manufacturing.

1.2. Composite Materials

A composite material is a material structured in the form of a combination of two or more component materials at a macroscopic level. The component materials are not soluble in each other when combined. One component is called the reinforcement and the one that the reinforcement is embedded in is called the matrix. The form of reinforcement material may come in the form of fibers, particles, or flakes. The matrix material is generally in the form of a continuous phase. Examples of traditional composites can be given as concrete reinforced with steel and epoxy reinforced with graphite fibers. The production of composite materials is costly in contrast to traditional monotheistic materials like metals which are produced by either machining or welding. This makes composites expensive compared to metals however some applications call for properties of combined materials to meet the requirements. The aviation industry is the sector that implements composite materials to its applications more than any other industry. This is due to the need for lightweight yet high-strength material properties for the materials to be used in aircraft. Conventional metals succeed to comply with the high-strength properties required for aircraft components nevertheless these materials fail to comply with low weight features of the assembly components. Composites provide substantial weight reduction while maintaining outstanding stiffness and strength. The use of composite materials reduces the number of parts to be used in the assembly of an aircraft causing a reduction in production costs. On the other hand, the use of these composite parts in an aircraft results in a lesser weight of the aircraft providing reduced fuel consumption and affecting operating costs positively. Having profited from both aspects compensates for the high production cost of composite parts making the use of such parts feasible in the aviation industry [23].

Most composite materials exhibit an anisotropic nature, meaning the properties of such materials shift considerably whilst tested in different directions. This may be attributed to the alignment of the direction of reinforcement fibers, which is generally the harder component embedded in the matrix. Thus the strength of the composite part becomes superior along the fiber's longitudinal axis compared to other directions in the material. Another cause of this is that one or more components of the composite structure may exhibit an anisotropic nature. This phenomenon can be used to the designers’ advantage when producing composite materials. When producing artificial composite materials, the control over the anisotropy resulting in choosing the superior property to be in the desired direction is a key engineering aspect. This is a different engineering perspective on the design of components using conventional materials. For instance, a composite material should be produced considering the direction it will be under certain forces which will utilize the superior properties of the composite part withstanding the stresses due to the direction of the load [24]. The direction of the long fibers in some composite materials resembles the direction of the extruded beads that form the layers of the fabricated part in the FDM method. The build orientation mentioned in previous sections drastically affects the mechanical properties of the produced part in the FDM method [13]. There is much research carried out in pursuit to understand the anisotropy resulting from the direction of the melted beams in the FDM method. There are composite filaments produced with the use of various fibers embedded in the filaments polymer matrix concentrically to be used in the FDM method. The types of polymer matrix composites will be discussed in this section.

Not all composites have a matrix and long fibers as reinforcement material. There are several different configurations of composite structures. Some of these types are illustrated in Figure 1.16.

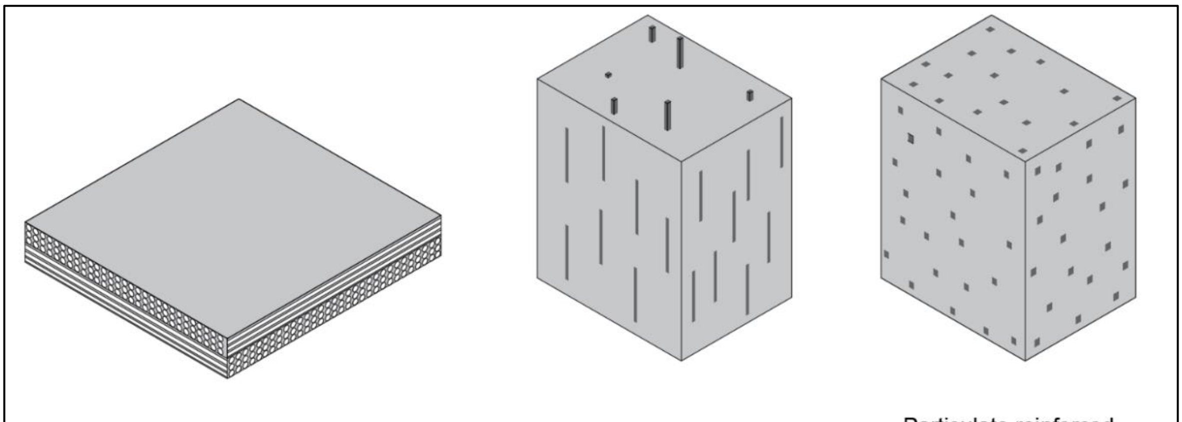

Figure 1.16. Some types of composite structures

The types of matrix materials used in composites in general are; polymers, metals, or ceramics however the most commonly used composites until today in the industry are polymer based. Generally, the polymers used in these composites are resins however there are occasions when thermoplastic polymers are used. Along with composites embodying long fibers of carbon or glass, reinforcement materials are in the form of short fibers and particulate forms. There is much research carried out to develop novel composites to obtain unique material characteristics [24]. This endeavor is also the aim of this thesis which is to enhance the vibrational characteristics of polymer matrix filament materials with the addition of particulate reinforcement.

1.2.1. Composite filaments in FDM technology

Pure thermoplastic filaments used in the FDM method have drawbacks such as insufficient strength and stiffness. For instance, in applications where high performance regarding the properties mentioned is required, the use of composite filaments may offer a solution other than the use of thermoplastic parts produced with injection molding. Thus, there is a growing interest in the research being carried out regarding composite filaments due to their superior properties compared to pure thermoplastics being used in the FDM process. In developing a composite filament for the FDM method, researchers should consider that such filaments should comply with the specific shape, ductility, and other properties required by the nature of the process. Generally, composite filaments incorporate many types and forms of reinforcement materials in their thermoplastic matrixes. It is more convenient to categorize composite filaments according to the types of reinforcements used, which can be seen in Figure 1.17.

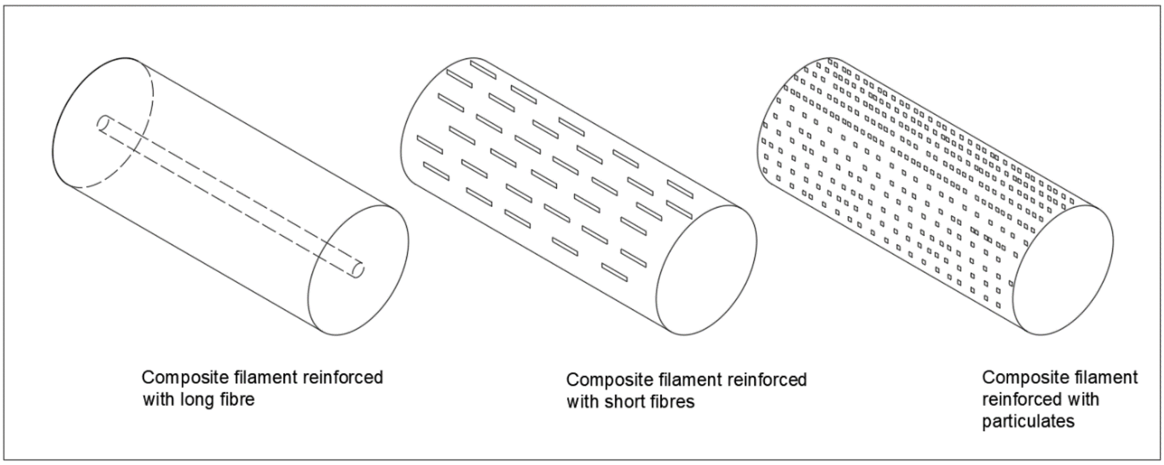

Figure 1.17. Various types of composite filaments

To manufacture the particulate composite filaments, reinforcement material in a certain particle size is blended in the polymer matrix, generally mechanically mixed with matrix material in the form of granules of polymers, then extruded into the filament via melting the mixture. The properties of the filament may depend on the size of the reinforcement particle, particle shape, orientation, volume fraction, and polymer-particle interface. Considering that the fabricated composite filament may clog the FDM extruder or break due to the brittleness of the filament, the choice of matrix and reinforcement material and the percentage of the mixture is important.

In this study, nano-sized particulate reinforcement-type composite filaments were investigated which are specified as nanocomposite materials. The focus will be on this type of composites in the rest of this thesis.

2. THEORATICAL BACKGROUND AND LITERATURE REVIEW

2.1. Vibration

In our daily lives, even if we are aware of it or not, we encounter many incidents of vibration, be it the noise of a car engine passing by or the sound coming from the speakers of a TV or a mobile phone. Since ancient times scientists studied the nature and working principles of the vibration phenomenon. They focused on developing mathematical models and expressions to explain the principles of vibration. Today the driving force behind studies concerning the vibration concept is machines, buildings, internal combustion engines, jet engines, etc… Among these systems, vibration occurs due to the lack of balance in the internal components such as crank shafts in engines. In general, we can see vibration issues caused by an imbalance in reciprocating parts in machines such as turbines, engines, and pumps. Vibration can cause additional wear in machine parts such as bearings and gears while causing extreme noise.

If the natural frequency of vibration of a system (a machine or a structure) overlaps with the frequency of the disturbance caused by external forces, a phenomenon called resonance takes place. This resonance phenomenon causes extreme deflections leading to the failure of the machine or structure. Due to the catastrophic effects of resonance in vibrating systems, vibration testing became a common engineering practice in the design of such components. When the design of vibrating systems is considered, the vibrating frequency needs to be reduced thus being far from the natural frequency where resonance might occur. This study also aims to investigate the effects of the addition of nanoparticles on the natural frequency of a 3D printed composite cantilever beam. In the future, the wings of small unmanned airplanes and drones might be built with polymer composite parts via AM and these parts act similar to a cantilever beam. Such research might lead to the use of such materials and manufacturing processes thus contributing to the existing studies.

When a particle, a body, or a system composed of linked bodies is displaced from a state of equilibrium through motion, this phenomenon is called vibration. It can also be defined in more simple terms as recurring motion with a certain time interval. The vibrating system is inclined to return to its equilibrium position and under some forces such as elastic forces or gravitational forces, the system moves backward and forwards about its equilibrium position. A vibrating system is generally comprised of a component that stores potential energy such as a spring or an elastic body, a component that stores kinetic energy such as a mass, and a component that causes the energy of the system to consistently decrease such as a damper as seen in Figure 2.1.

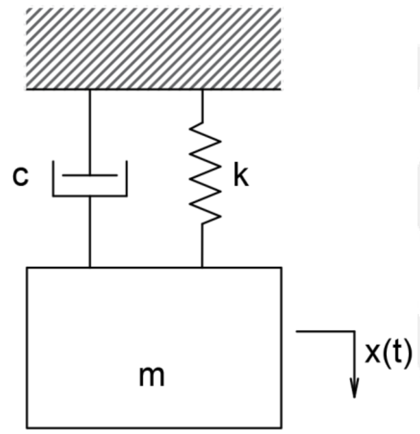

Figure 2.1. General representation of a vibrating system

As seen in Figure 2.1, there is a spring element in the vibrating system and the spring is an element where a force F is applied to one of its end tips, it elongates to a certain value of x. If there is such a relation between F and x like the Equation below then the spring is classified as a linear spring.

$$F = kx \tag{2.1}$$

Here, k is called the spring constant and it is a material property. Another element of the vibrating system is the damper and for the damper, another basic Equation is valid where F is the force, c is the damping constant and v is the velocity of the system.

$$F = cv \tag{2.2}$$

A vibrating system continues to vibrate by transferring its potential energy to kinetic energy and its kinetic energy to potential energy back and forth. If damping is present in the system, vibration will gradually diminish due to the energy loss in the system. However, if a steady vibration is desired to be sustained then the lost energy due to damping should be restored by an external impulse. This leads us to the classification of vibration where it will be discussed in the next subsection.

2.1.1. Classification of vibration

Although there are many ways to categorize types of vibration, we will make a general classification that is widely accepted.

- Free vibration: If a system is left vibrating at its own pace after an initial disturbance without exerting any additional force during vibration then this type of vibration is called free vibration.

- Forced Vibration: If a system is constantly subjected to a repeating force the type of vibration occurring is called forced vibration.

It should be remembered that when forced vibration is the case and the frequency of the external disturbance overlaps with one of the natural frequencies of the system, resonance occurs leading to unexpectedly augmented oscillations which cause damage and failure in the system.

- Damped vibration: Through the entire oscillatory movement, if there is any loss in the energy of the system due to friction or other resistive forces, this type of vibration is called damped vibration.

- Undamped vibration: As its evident from the term used, when there is no loss of energy caused by any kind of resistance in the system, this type of vibration is called undamped vibration.

In almost all real-world systems, damping is so minor that it is generally neglected especially from an engineering perspective. Nevertheless, if a vibrating system is near a frequency that is close to resonance then the assessment of damping becomes quite crucial.

- Linear vibration: If the standard elements of a vibrating system such as a spring, a damper and a mass all act in a linear manner, the system resonate in a linear vibration pattern. The governing Equations to solve such a system are linear differential Equations.

- Non-linear vibration: In a case where the standard elements of the system act non-linearly, the oscillation takes place in the form of non-linear vibration. The governing Equations to solve such a system are linear differential Equations.

- Deterministic vibration: In a vibrating system, provided that the amplitude or the amount of the external force exerted on it is known at any specified time then this kind of oscillation is called deterministic vibration or periodic vibration.

- Nondeterministic vibration: In some cases, it is not possible to foresee the amplitude of the force exerted on the system then this kind of vibration is called a nondeterministic vibration or a random vibration. In such cases, data obtained in large amounts is used with statistical methods to estimate the magnitude.

Periodic and deterministic vibration signals are illustrated in figure 2.2.

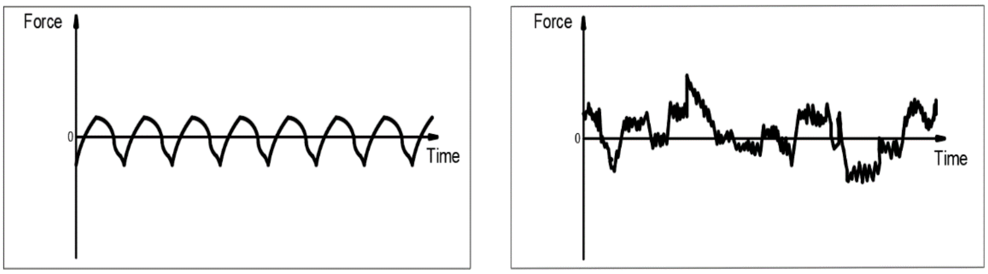

(a) (b)

Figure 2.2. (a) Periodic vibration (b) Random vibration

2.1.2. Damping and vibration

The vibrational energy is gradually transformed into heat or sound in many practical vibration cases. The response, such as the system's displacement, gradually reduces as the energy level diminishes. Damping is the process through which vibrational energy is progressively transformed into heat or sound. Despite the comparatively low amounts of energy that are transformed into heat or sound, damping considerations become crucial for a precise forecast of the system's vibration response. A damper is presumed to be free of both mass and elasticity, and damping force can only exist in the presence of relative velocity between the damper's two ends. It is challenging to pinpoint the reasons for damping in real-world systems. In most cases, damping is modeled as one or more of the damping categories described below.

2.1.2.1. Viscous damping

The most widely employed damping model in vibration analysis is viscous damping. If a mechanical system is in an environment where it is surrounded by a fluid such as air, gas, water, or oil, the resistance applied by the fluid to the vibrating body results in the dissipation of the energy. The quantity of energy dissipation depends on many parameters such as the dimensions and the geometry of the body in vibration, the viscosity of the fluid, vibration frequency, and the velocity of the body that is in vibration. The damping force is proportional to the velocity of the body that is vibrating when viscous damping is the case.

2.1.2.2. Coulomb damping

Coulomb damping can be discussed when there is friction between layers of solids that are wearing onto each other. In such cases, the surfaces are either dry or lubrication is lacking. The magnitude of the damping force is steady and it is in the opposite direction of motion.

2.1.2.3. Hysteretic damping

When a body gets subjected to deformation, the body absorbs the energy causing the dissipation of the energy. When there is deformation in the body, the friction between the internal planes that slip causes the energy to be absorbed [25].

2.1.3. Free vibration

To understand the motion of vibration in general terms, first, we should consider a case where an external force is exerted on a single degree of freedom system at a given time and then we must write the Equation of motion of the system. We will apply Newton's second law of motion to the given system and the forces acting on the system are shown in Figure 2.3.

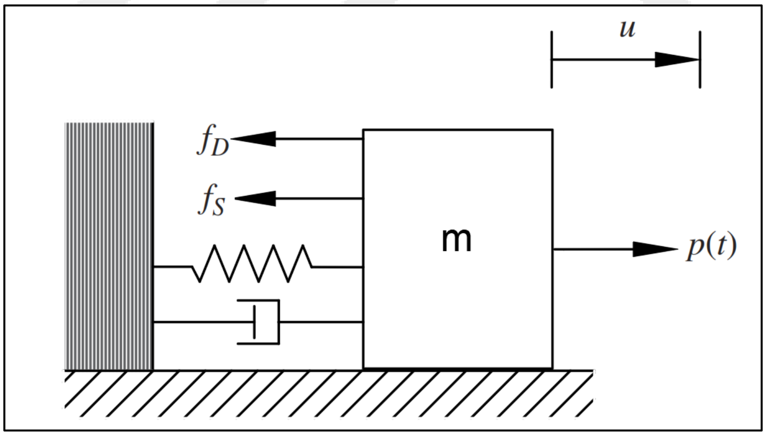

Figure 2.3. The forces acting on the mass at any given time instant

The forces shown are the external force $p(t)$, the elastic resisting force f_s, and the damping resisting force f_D . The external force $p(t)$ is exerted in the direction of the degree of freedom u and from the notation, it is understood that force p changes with time t. It is clear that the displacement of the mass also varies with time and is denoted as $u(t)$. The direction of the force $p(t)$ is taken positive on the x-axis, and the displacement $u(t)$, velocity $\dot{u}(t)$, acceleration $\ddot{u}(t)$ are considered positive in the mentioned direction. The direction of the elastic and damping forces was taken in the opposite direction since elastic force resists deformation and damping force resist velocity as internal forces of the system. It was assumed that no friction between the surface and the mass was present. When we consider the resultant force in the x-axis we get $p - f_s - f_D$ and according to Newton's second law of motion, this yields to

$$p - f_s - f_D = m\ddot{u} \tag{2.3}$$

$$m\ddot{u} + f_s + f_D = p(t) \tag{2.4}$$

We can say that $f_s = ku$ and $f_D = c\dot{u}$ and substitute these into Equation (2.4) we get

$$m\ddot{u} + c\dot{u} + ku = p(t) \tag{2.5}$$

If a linear single degree of freedom (SDOF) system vibrates freely without any damping occurring, then to understand the physics of the excitation we shall write the Equation of motion of the system. When we consider the governing Equation (2.5), we will take $p(t) = 0$ for the motion is free vibration and also we should note that $c = 0$ since there is no damping involved. For the free vibrating system without damping, the governing differential Equation becomes

$$m\ddot{u} + ku = 0 \tag{2.6}$$

Free vibration is triggered by giving the mass a little displacement $u(0)$ from its steady resting position and velocity $\dot{u}(0)$ at time zero which gives us $u = u(0)$, $\dot{u} = \dot{u}(0)$ where these define the displacement and velocity of the system at the exact moment when the excitation is triggered. Given these initial conditions, when standard methods have used the solution to the differential Equation is found as

$$u(t) = u(0)cos\omega_n t + \frac{\dot{u}(0)}{\omega_n} sin\omega_n \quad (2.7)$$

where

$$\omega_n = \sqrt{\frac{k}{m}} \quad (2.8)$$

When we get the plotted graph of Equation (2.7) in Figure 2.4., we see that this system is subject to oscillatory motion about its static initial position and the repetition is observed every $2\pi/\omega_n$ seconds. This motion is commonly known as simple harmonic motion.

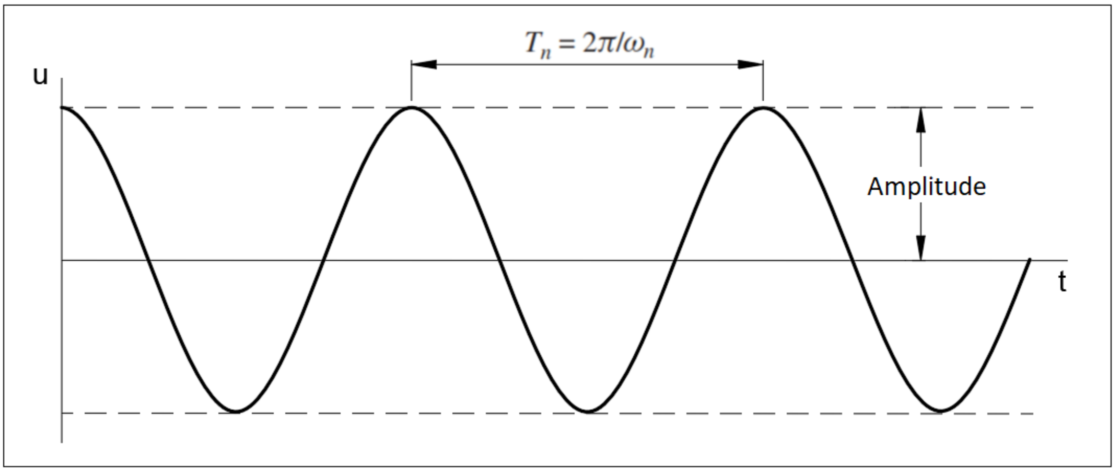

Figure 2.4. Simple harmonic motion

When one cycle of free vibration is completed in the undamped system the amount of time elapsed is described as the natural period of vibration of the system. This term is designated as T_n in the units of seconds.

$$T_n = \frac{2\pi}{\omega_n} \quad (2.9)$$

A system completes $1/T_n$ cycles in one second and this amount is called the natural frequency of vibration which equals to

$$f_n = \frac{1}{T_n} \tag{2.10}$$

The units used for f_n are hertz (Hz), meaning cycles per second, and the relation between f_n and ω_n is given below.

$$f_n = \frac{\omega_n}{2\pi} \tag{2.11}$$

When we mention natural frequency we mean both ω_n and f_n.

2.1.4. Natural frequency and mode shapes

When a system is let to freely oscillate and there is no additional external excitation, the frequency at which the system vibrates is called the natural frequency. The term natural is used because this frequency value is a natural property of the system. This property depends on the mass and stiffness of the system keeping the geometry constant. If a system is stiffer than the other, it will have a higher natural frequency provided that the two single-degree-of-freedom systems have the same mass. Additionally, if two systems having the same mass are compared, the one having a heavier mass will have a lower natural frequency value. The natural frequency of systems interests us because when the vibrating frequency of the system caused by an applied periodic force equals the natural frequency of that system a phenomenon called resonance occurs. When resonance occurs the amplitude of the system drastically increases causing devastating effects on the system. Therefore, identifying the natural frequency of a system is crucial to avoid the occurrence of resonance by keeping the frequency of the forced vibration of that system away from the natural frequency value. A system does not possess just one natural frequency value; it possesses more than one. To be more specific, a system having n degrees of freedom has n natural vibration frequencies. These are called natural modes of vibration or natural modes of vibration. The subscript n is used for the mode numbers and mode 1 is also called the fundamental mode.

Throughout free vibration in each mode shape, the system oscillates at its natural frequency of that mode and all degrees of freedom vibrate at the common phase value, changing their positions between their maximum, minimum, and zeros. The shape of the movement is characteristic of the vibration mode shape. In order to understand the concept, the first three mode shapes of a cantilever beam and the Equations for the calculation of natural frequencies of the modes are given in Figure 2.5.

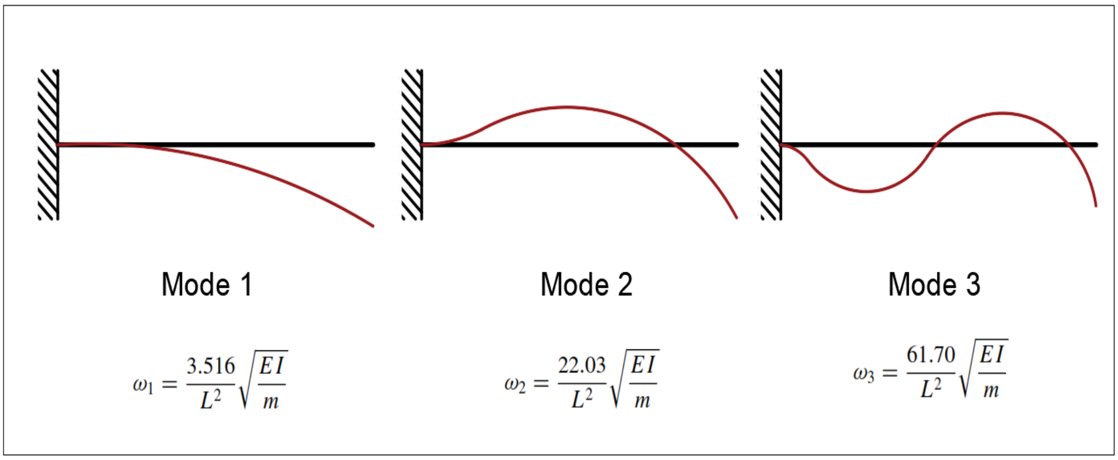

Figure 2.5. The first three mode shapes of a cantilever beam and the natural frequency Equations

2.1.5. Free vibration involving viscous damping

When a system is vibrating freely with viscous damping present, the motion is affected by some key factors that we will define. As stated previously, c is the damping constant which is generally defined as the measure of the energy released during one cycle of free vibration or one cycle of forced vibration. Here, two more concepts will be introduced are critical damping coefficient (c_{cr}) and damping ratio (ζ).

The damping ratio is an indicator of damping which is dimensionless and it is a property of the vibrating system that is dependent on the mass and stiffness of the system.

The damping ratio is referred to as

$$\zeta = \frac{c}{2m\omega_n} = \frac{c}{c_{cr}} \tag{2.12}$$

The other important term that affects the motion of a damped vibration is the critical damping coefficient. This value determines the type of oscillation that will occur in the vibrating system. We can rewrite Equation (2.12) to obtain c_{cr} and we obtain

$$c_{cr} = 2m\omega_n = \frac{2k}{\omega_n} \tag{2.13}$$

In a damped vibrating system we may observe three different types of oscillating motion related to the values of c_{cr} and ζ.

In cases where $c < c_{cr}$ or $\zeta < 1$, the oscillatory motion of the system takes place near its equilibrium coordinate with a gradual decrease in the amplitude until it reaches the rest position. This type of vibration is called underdamped vibration.

In some cases where $c = c_{cr}$ or $\zeta = 1$, the system rapidly reaches the equilibrium position without any oscillation taking place. This type of vibration is called critically damped vibration.

Finally, in cases where $c > c_{cr}$ or $\zeta > 1$, the system reaches the equilibrium position faster than a critically damped sytsem without the occurring of any oscillation as well. This type of vibration is called overdamped vibration. Figure 2.6 illustrates these three types of oscillating motions in a damped vibrating system.

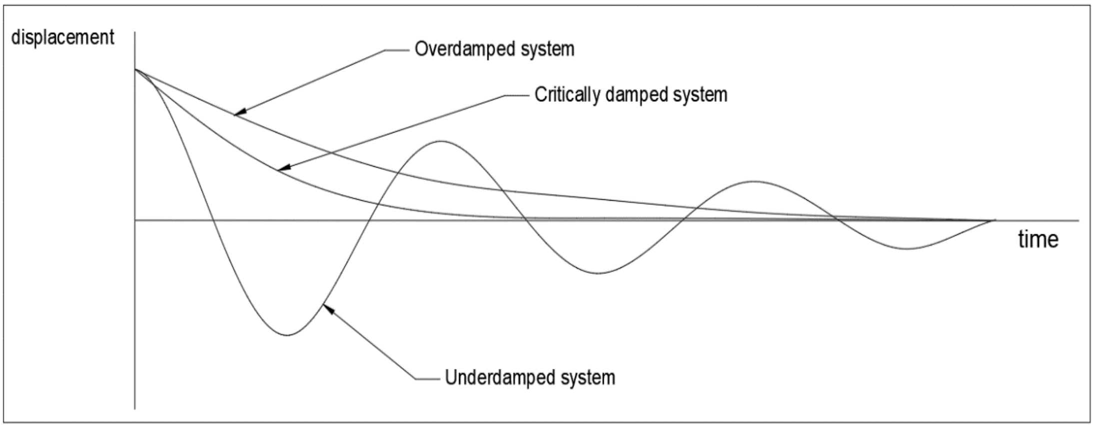

Figure 2.6. Vibration of overdamped, underdamped, and critically damped systems

Here we can see that the critical damping coefficient c_{cr} is the key value determining the minimum value of c that can damp the system without any oscillation. Therefore, it was named as a critical value that can determine if there will be an oscillatory or nonoscillatory motion in a system. Including the nanocomposite cantilever beams investigated in this thesis, most vibrating systems are in the category of underdamped systems. Therefore, the focus of this thesis will be on underdamped systems and their calculations.

2.1.5.1. Vibration of Underdamped Systems

The Equation of motion for the free vibration of an SDF system with damping;

$$m\ddot{u} + c\dot{u} + ku = 0 \tag{2.14}$$

Solving the Equation with the initial conditions $u = u(0)$, $\dot{u} = \dot{u}(0)$ and damping values of the system $c < c_{cr}$ or $\zeta < 1$ we get;

$$u(t) = e^{-\zeta\omega_n t}\left[u(0)cos\omega_D t + \frac{\dot{u}(0) + \zeta\omega_n u(0)}{\omega_D} sin\omega_D t\right] \tag{2.15}$$

and

$$\omega_D = \omega_n\sqrt{1-\zeta^2} \tag{2.16}$$

In Figure 2.7 the plotting of Equation (2.15) can be seen. The oscillating movement of the free vibration of a system without damping was given with the same system oscillating under the effect of viscous damping having the condition of ζ < 1. The initial displacement $u(0)$ and velocity $\dot{u}(0)$ of both damped and undamped oscillations in the Figure 2.7 are the same, therefore the displacement-time graph for both systems initiate at t = 0 with the same displacement value. The natural frequency of damped vibration is ω_D while the natural frequency for the undamped system is ω_n. The relation between these two frequencies depending on the damping ratio is given in Equation (2.16). Given that the natural period of damped vibration $T_D = 2\pi/\omega_D$, we get the relation between T_D and natural period of the undamped system T_n as

$$T_D = \frac{T_n}{\sqrt{1-\zeta^2}} \tag{2.17}$$

As can be seen in Figure 2.7, the undamped system oscillates with the same amount of displacement amplitude in every consecutive cycle however the damped system has a decreasing displacement amplitude in every consecutive cycle of the oscillation.

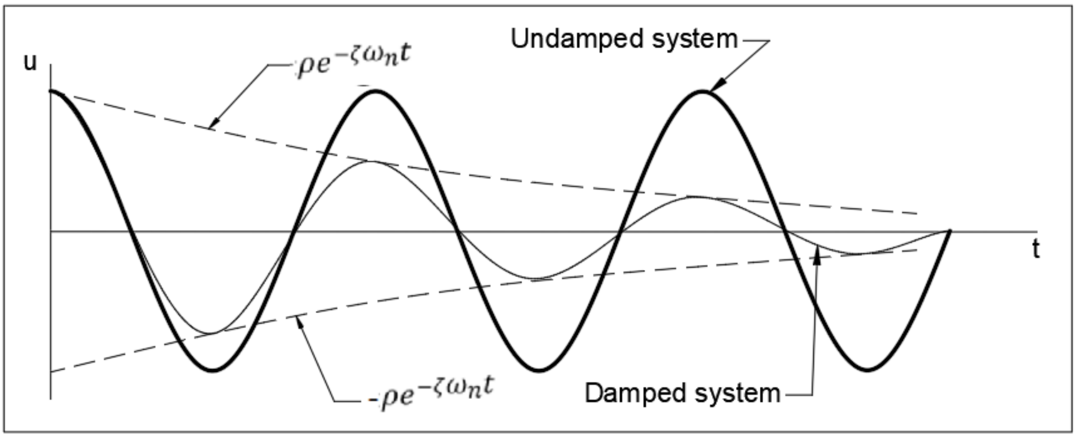

Figure 2.7. Undamped system versus the damped system and the envelope curves

It can be mathematically seen from the Equation (2.18) that the decay of the amplitude with time is of exponential form and it can be seen in the plot in Figure 2.7. The curves that are tangent to the displacement –time curves at points merely to the right of the peak values are defined as envelope curves. The exponential function of these curves is in the form of

$$u = \pm \rho e^{-\zeta \omega_n t} \tag{2.18}$$

When damping is present in a vibratory motion, it causes the natural frequency to decrease in value from ω_n to ω_D and in parallel, the the natural period value increases from T_n to T_D. In cases where damping ratio values are less than 0.2, the category which the majority of structures fall into, the decrease in ω_n and the increase in T_n due to the presence of damping becomes very small thus making it negligible [26].

2.1.6. Free Vibration of a Cantilever Beam

We should bear in mind that cantilever beams are considered to have an infinite number of degrees of freedom in vibration considerations. We shall first give the general definitions regarding a cantilever beam and its properties. The representation and general dimensions of a cantilever beam can be seen in Figure 2.8.

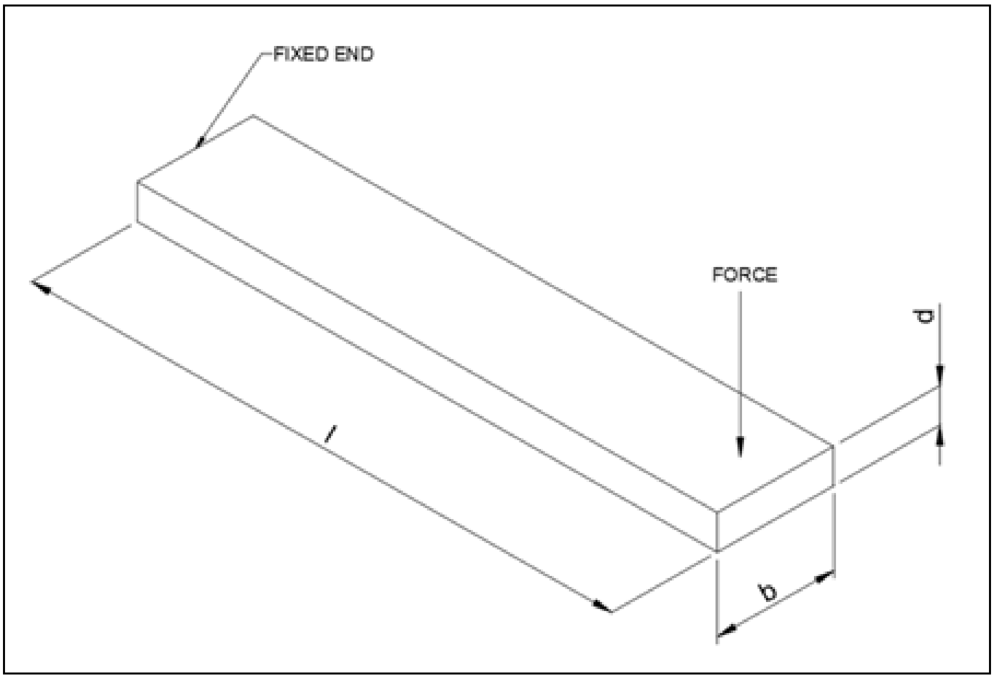

Figure 2.8. Dimensions of a cantilever beam

As can be seen in Figure 2.8. the length of the cantilever beam is represented with the letter l, the dimension of the beam parallel to the force is called its depth and it is presented with the letter d and finally, the breadth of the beam is represented with the letter b. The volume (V) of the beam can be calculated with the formula

$$V = l \times b \times d \tag{2.19}$$

To calculate the mass of a cantilever beam we shall use the relation between mass and volume which is $m = V \times \rho$ where m is the mass and ρ is the density. Thus, when we calculate the mass of the beam we use the formula

$$m_{beam} = \rho \times l \times b \times d \tag{2.20}$$

One of the key properties of a cantilever beam subjected to free vibration is the stiffness of the beam material. This property is defined by Young's Modulus of the material and it is determined by tensile tests results of the material. It is represented by the symbol E, and calculated by the ratio of stress to strain under tensile loading. Another key factor affecting the vibratory properties of a cantilever beam is the moment of inertia or the second moment of area. This feature depends on the breadth (width) of the cross-section of the beam concerning the direction of the force applied. For a rectangular section beam that a force is applied in a direction similar to the one in Figure 2.8, and the moment of inertia is calculated as

$$I = \frac{bd^3}{12} \tag{2.21}$$

Finally, as explained in previous sections the spring constant of a vibrating system is an important aspect when solving the Equations of motion in the system. For a cantilever beam, the spring constant can be calculated with the formula

$$k = \frac{3EI}{l^3} \tag{2.22}$$

Now that we have mentioned the fundamental factors of the free vibration of a simple cantilever beam, we shall be dealing with the cantilever beam types that are the subject of this thesis. Through mathematical analysis the calculation of the natural frequency of a horizontal plain cantilever beam can be calculated in Hertz mathematically as

$$f_{beam} = \frac{1}{2\pi} \times 3.515 \sqrt{\frac{EI}{m_{beam} l^4}} \tag{2.23}$$

Equation (2.23) gives the value of the first natural frequency for a plain cantilever beam similar to the representative beam in Figure 2.9, as previously discussed, various mode shapes are dependent on the degree of freedom of a vibrating system. The natural frequencies of other modes will not be discussed in the thesis since the testing equipment is only capable of measuring the 1st mode of the natural frequency of the beams manufactured, which will be discussed in the forthcoming sections.

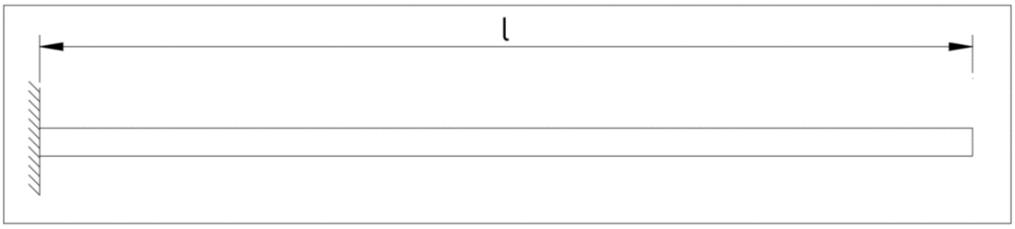

Figure 2.9. Plain cantilever beam

When a tip mass is added to the cantilever beam, the first natural frequency calculation can be made with

$$f = \frac{1}{2\pi}\sqrt{\frac{3EI}{(\frac{33}{140}m_{beam} + m_{mass})l^4}} \tag{2.24}$$

In vibration tests of cantilever beams, to measure displacement or acceleration, sensors are placed at the tip of cantilever beams and to make precise calculations the mass of the accelerometer as seen in Figure 2.10. The sensor should be taken into account thus this analytical formula should be used. Along with this analytical method, the finite element analysis will be used to crosscheck the physical test results for natural frequency calculations.

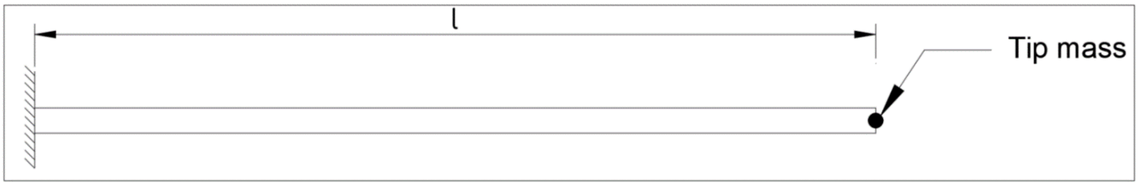

Figure 2.10. Cantilever beam with a tip mass

2.2. Literature Review

Thanks to the key advantages of AM (or 3D printing) such as design freedom, product customization, minimization of waste, capacity to build complicated structures, and fast prototyping, there has been many studies conducted regarding the many different methods of AM discussed in the previous chapter.

2.2.1 Studies on the FDM Process

A very thorough study was conducted in [27], reviewing the aspects of principal methods of AM with corresponding materials used and regarding these aspects, the study covers the different fields of industries that these techniques are being applied as the methods advance also pointing out both advantages and drawbacks that occur. Among these drawbacks are; anisotropy caused by the nature of the am process, the presence of voids in the product, and the poor surface quality due to the layered structure. Many studies are being carried out to minimize or get rid of these disadvantages which contributes to the advancement of AM technology.

Since this thesis investigates the application of the FDM method which is one of the many AM methods available, we shall focus on the studies concerning the FDM process. As stated in the previous chapter, the properties of parts fabricated using the FDM method significantly depend on the filament material and printing parameters. Many studies concerning the effect of printing parameters on the various properties of parts printed with the FDM method are available in the literature. In [21] a review of many studies on the effect and optimization of various printing parameters on tensile strength, compressive strength, flexural strength surface roughness, dimensional accuracy and build time was made that summarizes the important works on the subject. The mentioned study also discusses the many optimization techniques used in the studies so far to obtain the best output by using the optimum parameters.

2.2.2 Studies concerning the macro level composite filaments used in the FDM process

As stated in the previous paragraph along with printing parameters, the filament material also drastically affects the properties of the 3D printed product in the FDM process. The availability of various thermoplastics was discussed in the introduction section thoroughly. Today the search for novel materials to be employed in FDM technology is apparent and the use of polymer matrix composites as filament material is of trend. As mentioned in the previous chapter these composites may be short fiber reinforced, long fiber reinforced, micro-sized particle added and nanoparticle added polymer composites.

Addition of copper and iron metal particles to ABS matrix filament on a micron size scale was investigated in [28] to observe their effect on thermal and mechanical properties. Particle addition to the ABS matrix was up to 40% in volume for both Fe and Cu fillers. Thermal conductivity and heat capacity were the subjects of thermal properties of the composites and the addition of both Fe and Cu particles increased thermal conductivity while the addition of Fe particles reduced heat capacity. In terms of dynamic properties, it was observed that below glass-transition temperature, being in a solid state, a significant increase in the storage modulus of composites was observed when the volume fraction of added material increased.

As stated earlier, long fiber-reinforced filaments can also be utilized as feedstock material for the FDM method to enhance the mechanical properties of the printed part. Glass and carbon fiber-reinforced Nylon filaments were used in [29] to assess the effects of long fiber inclusion in the filament on mechanical properties. The properties that were investigated for the 3D printed composites were plane strength and stiffness in terms of tensile and compression load states. While the results showed satisfactory improvement compared to printed parts with pure nylon filament, they were far from obtaining the mechanical properties of traditional composites such as pre-pregs. This was linked to the porosity of the nylon parts produced by the FDM method and also the limited quantity of fibers due to the filament fabrication process.

A benchmarking effort was made in [30] to compare the short fiber reinforced filaments with continuous fiber-reinforced filaments of nylon matrix and carbon fiber reinforcement. The results showed that the use of continuous fiber-reinforced filaments showed a significant increase compared to the pure nylon filaments especially in stresses along the same direction with fibers just as conventional unidirectional epoxy matrix composites. However, the method has a drawback of filament deposition limitations, especially in steep angle turns thus restricting the design options of the printed material. On the other hand, the use of short carbon fiber (around 100 microns) reinforced filaments resulted in more prominent printing capabilities however the increase in mechanical properties compared to pure nylon parts was narrowly better. It was proposed that the length of the short fibers could be increased above the critical length to achieve mechanical properties close to that of continuous fiber-reinforced filaments and the advantage of better printability of short fiber filament can be attained.

2.2.3 Studies concerning nanocomposite filaments used in the FDM process

Apart from short fiber-reinforced, long fiber-reinforced, and micron-sized particle-added polymer composites, this thesis includes the use of nanoparticle-added polymer composite filaments as feedstock material to be used for the FDM method. The addition of nanoparticles into the filament material during the extrusion process is a promising field of research thanks to its potential to enhance existing thermoplastics' properties in distinctive ways. Compared to micro-sized particulate additives, nano-sized particles have a higher volume-to-surface ratio enabling the particles to cover broader surfaces and this increases their potential to affect the properties of the created composite. Many studies have been carried out to assess the effects of nanoparticle addition to existing filament materials on various aspects of products such as mechanical, dynamic, thermal, chemical, and electrical properties.

The investigation of the effect of various nanoparticle-sized additive materials on different polymers used as filament material for the FDM method is the subject of trending research recently. This type of research is in its developmental phase. As a novel study, [31] investigated the effect of 10% Graphene nanoparticle addition in weight to PLA matrix filament material that was commercially available in the market compared to pure PLA filament material that was also purchased from the market. X-ray computed microtomography analyses were carried out and the dimensional accuracy of the fabricated samples was found to be very satisfactory. Scanning Electron Microscopy (SEM) results showed that the nanoparticles of Graphene were uniformly dispersed in the PLA matrix. The research regards Graphene as a multifunctional additive therefore many properties were investigated. The volume resistivity of specimens was examined and it was found that the direction of the measurement drastically affected the values compared to the pure PLA and this was attributed to the build direction of the FDM specimens. Dielectric properties were also studied and it was found that the nanoparticle-added PLA samples showed a higher dielectric constant value than that of plain PLA samples. Electromagnetic interference (EMI) shielding efficiency (SE) of the samples was also compared and nanocomposite samples displayed much greater values.

As of dynamic mechanical properties, the storage modulus change with temperature was also examined and a 20-30% increase in storage modulus value was recorded in graphene-added PLA samples below the glass transition temperature. Finally, as for mechanical properties, elastic modulus, tensile strength, and strain at break values of plain PLA and graphene-added PLA samples were tested. The PLA samples having Graphene nanoplatelets exhibited a 30% increase in elastic modulus values and they also possessed an ultimate tensile strength value of 27% more than that of pure PLA samples. However, the strain at the break value of the PLA/Graphene samples were slightly lower than plain PLA samples.

Being one of the most frequently used materials in the FDM method, PLA was used in [32] as the matrix material and graphene was used as reinforcement material in pursuit to investigate other properties such as nano-hardness, elastic modulus, wear resistance, and creep resistance of the composite filament. As a result of the tests all values of the nano-hardness, elastic modulus, displacement resistance, wear resistance and creep resistance properties of the nanocomposite specimens were higher than the pure PLA specimens. The increase of the values in terms of percentage was 18%, 11%, 25%, 14%, and 21% respectively. The porosity of PLA-Graphene structures was observed to be greater in contrast to pure PLA parts which made them suitable for biochemical applications thanks to higher porosity while having better mechanical properties.

Other polymer filament materials were also employed as the matrix material in previous studies to develop novel filament materials with enhanced properties. As a distinctive material, polyetheretherketone (PEEK) was employed in [33] as the matrix material and both Carbon nanotubes and graphite nano-plates were used to enhance the electrical conductivity of the filament material while some mechanical properties were investigated as well. The weight percentage of carbon nanotube addition was chosen as 3-4% on the other hand the weight percentage of graphite nano-plates addition was chosen as 1-3% for the production of nanocomposite filaments. The test results revealed that the elastic modulus, ultimate tensile strength, electrical conductivity, and thermal conductivity properties were enhanced with the nanoparticle inclusion however ductility and elongation at break values decreased.

To fabricate multidirectional embedded strain sensors with the FDM method with ease, pure TPU and TPU/multiwall carbon nanotubes (MWCNT) were used as filament material and the effects of MWCNT addition were investigated in [34]. Uniaxial and biaxial sensors were fabricated with the FDM method using TPU and TPU/MWCNTs materials. Following that, a series of cyclic strain loads were applied to the sensors. The sensors responded to strains as high as 50% with outstanding piezo-resistive performance and cycle repeatability in both axial and transverse directions, according to the results.

2.2.4 Studies concerning the use of ABS as the matrix for nanocomposite filaments used in the FDM process

Since this thesis employs ABS as the matrix material for the fabrication of two different nanocomposite filaments of Carbon black nanoparticle additives and Calcium Carbonate nanoparticle additives, it is essential to review the efforts in the literature which use ABS as the matrix material as well. Many studies were carried out investigating ABS matrix nanocomposites having various additives and different properties of the specimens were investigated.

Aiming to create a novel nanocomposite, [35] employed ABS as the matrix material while a nano-filler of Graphene Oxide (GO) particles was employed and the characterization of the new filament was carried out by inspecting some aspects such as mechanical properties, printability and thermal properties. In producing the filaments dry mixing and solvent mixing methods were used separately. The tensile tests showed that the addition of nano-sized Graphene Oxide particles provided significant improvement in tensile strength and Young's Modulus however the elongation at break values decreased where further research was recommended for the improvement of this aspect. In general, the printability of the pure ABS and ABS/GO specimens were similar however the ABS/GO filament produced with the dry mixing method caused clogging in the extruder head which led to bad prints. In terms of thermal properties, the glass transition temperature of pure ABS and ABS/GO filaments produced with both methods were found to be very close. This enabled the use of the same extrusion temperatures in the printing process with pure ABS filaments.

In a unique effort [36] facilitated the addition of multiwall carbon nanotubes (MWCNTs) to the ABS matrix filament fabricated with a twin-screw micro-compounding extruder possessing a backflow facility then the compound was processed with a single screw extruder into 1.7 mm filament. According to the SEM images MWCNTs were uniformly distributed in the ABS matrix with this filament fabrication method. The specimens were produced using a commercial printer and the tensile tests along with electrical conductivity tests were carried out. The raster angle was also investigated along with the MWCNT loading percentage in the matrix. According to the tensile tests, the addition of 7% MWCNTs with [0,90] raster angle provided a 288% increase in ultimate tensile strength value compared to pure ABS. On the other hand, the highest electrical conductivity value of 232 e^{-2} S/cm was obtained with a 10% MWCNT addition. This value was a drastic increase in electrical conductivity.

Aiming to obtain a nanocomposite filament, [37] used ABS as the matrix material and organically modified montmorillonite (OMMT) as the reinforcement material, the mechanical and thermal properties of parts fabricated with both the FDM method and injection molding method were compared using the new nanocomposite polymer filament to understand the effect of OMMT inclusion in the matrix. Among these investigated mechanical properties were tensile strength, flexural strength, thermal expansion, and storage modulus regarding dynamic properties. The outcomes of the experiments revealed that when the FDM method was used with the filament having 5% OMMT addition in terms of weight, the tensile strength of the nanocomposite specimens was increased by 43% relative to the pure ABS specimens. On the other hand, the specimens fabricated with the injection molding method having 5% weight OMMT addition showed an improvement of 28.9% in tensile strength value compared to pure ABS injection molded specimens. Furthermore, it was concluded that the increase in OMMT percentage in the composite material leads to a decrease in the linear thermal expansion value. This enables a decrease in the warpage of the 3D printed specimens and results in less deformation of the parts.

Using graphene nanoplatelets as the reinforcement material with ABS polymer matrix, [38] aimed to fabricate a composite filament for an FDM printer. An initial effort was carried out to detect the optimum weight percentage value of the Graphene filler among 2%, 4%, and 8%

in terms of weight. The addition of 4% Graphene nanoplatelets was found to be optimal when elastic modulus, ultimate tensile strength, and melt flow index values were considered. The values of elastic modulus, dynamic storage moduli, and thermal stability were improved while elongation at break value was decreased with the Graphene nanoplatelet addition. Another highlight of the study was that the most important parameter for the maximum increase in mechanical properties was the selection of build orientation which gives the best values when the deposition of the beads is parallel to the load direction.

Experimenting the use of Zinc Oxide (ZnO) additives both in nano and micro-scaled dimensions for an ABS matrix composite filament production [39] studied the mechanical properties of both specimens. In different proportions, Acrylonitrile Butadiene Styrene (ABS) matrices were mixed with zinc oxide nanoparticles (ZnO nano) and zinc oxide microparticles (ZnO micro), and printable filament having 1.75 mm diameter was extruded. International standards were followed for producing tensile and flexion specimens using composite filaments in a commercial 3D printer. When compared to pure ABS specimens, the results demonstrated a 14 percent increase in tensile strength at a 5 percent weight concentration in both nanocomposite and micro-composite materials. Additionally, flexural strength increased by 15.3 percent in ABS/ZnO nanoparticles at 0.5 percent weight and by 17 percent in ABS/ZnO micro-sized particles at 5 percent weight. The ABS/ZnO micro composite structures outperformed the ABS/ZnO nanostructures in terms of overall mechanical strength when the two composites were compared.

In [40], ABS was chosen as the matrix material for the novel nanocomposite and Titanium Dioxide (TiO_2) and Antimony (Sb) doped Tin Oxide (SnO_2) nanoparticles (NPs), hereafter described as ATO, were selected as fillers having various weight % rates. Tensile and flexural tests were carried out to detect the nanoparticle addition effect on these properties. Comparing filled ABS to unfilled ABS, it was found that TiO_2 filler increased overall tensile strength by 7%, flexure strength by 12%, and micro-hardness by 6%. For ATO filler, the equivalent values were 9%, 13%, and 6%, respectively. TiO_2 and ATO NPs' sizes were determined by atomic force microscopy (AFM) to be 40 nm and 52 nm, respectively. To confirm the polymer structure and the incorporation of TiO_2 and ATO Nano-crystallites in the polymer matrix, Raman spectroscopy was carried out on the TiO_2 and ATO NPs as well as the 3D printed nanocomposites.

In addition to strength, [41] examined the thermal conductivity and mechanical characteristics of composites made from 3D-printed and injection-molded ABS and Boron Nitride (BN). For heat dissipation and packaging applications in electronics, the thermally conductive yet electrically insulating composite material offers a special combination of features. Melt mixing on a twin-screw compounder was used to create the materials, which were subsequently extruded or injected into filament for 3D printing using fused deposition modeling (FDM). The infill orientation of the 3D printed composites was changed to explore the influence on characteristics. Compositions of up to 35 weight percent BN in ABS were created. While 3D printed samples with 35 wt.% BN displayed a value of 0.93 W/ m-K, more than 5 times the conductivity of pure ABS, injection molding yielded a maximum in-plane conductivity of 1.45 W/ m-K. Anisotropic thermal conductivity results, with through-plane thermal conductivity being 3 times lower for injection molding and 4 times lower for 3D printing. The flexural modulus was very slightly increased by the addition of BN flakes, while the flexural strength and impact toughness were significantly reduced. It is demonstrated that while BN exhibits significant potential as a filler material for quick prototyping of thermally conductive composites, injection molding still generates components with excellent thermal and mechanical characteristics.

2.2.5 Studies concerning the use of $CaCO_3$ as reinforcement for various nanocomposite filaments used in the FDM process

This thesis is based on the production of two nanocomposite polymer filaments of ABS matrix, one having nano Carbon Black additive particles and the other having nano Calcium Carbonate additive particles. It is therefore essential to review the studies carried out with the use of the nanocomposite additives mentioned.

Recently, [42] employed commercially available calcite powders and three different synthetic $CaCO_3$ polymorphs (aragonite, calcite, and vaterite) as fillers to obtain polymeric composite filaments having Polypropylene random copolymer (PPR) as the matrix material. The evaluations were made based on the fabricated filaments themselves, not 3D printed specimens. Based on the analysis of data from various testing methods, it was seen that each type of $CaCO_3$ polymorph used has a significant impact on the filament properties. The results suggested that only aragonite-added filaments had shown significant improvements in terms of mechanical properties.

Employing bio-materials [43] used bamboo powder (BP) reinforced PLA composite filaments treated with Nano $CaCO_3$, cellulose nanofibers (CNF), and microcrystalline cellulose (MCC) using impregnation modification technology. Compared to pure PLA/BP filament, all other nano-treated composite filaments caused an increase in the storage modulus of the specimens below the glass transition temperature. Above the glass transition temperature, the improvement in the storage modulus was smaller. The tensile strength of the composite filaments which were nano-treated with $CaCO_3$, CNF, and MCC produced with ‘’one step method’’ increased by 40.33%, 12.32%, and 32.35% respectively compared to pure PLA/BP samples. The loss modulus and loss factor values of all composite filaments were higher than that of PLA/BP filament.

Parallel to this thesis, the studies carried out using ABS as matrix material and nano $CaCO_3$ particles as reinforcement material are also listed below. It is important to review these studies to find out which properties of these composites were investigated.

Two composite filaments were fabricated in [44] where one of them included ABS reinforced with micron-sized calcium carbonate ($CaCO_3$) particles while the other included ABS matrix reinforced with nano-sized $CaCO_3$ particles employing the melt compounding method. In comparison to plain ABS, the micron-sized ABS composites were shown to have a greater elastic modulus but a lower tensile and impact strength. On the other hand, given a specific nano-sized $CaCO_3$ particle addition ratio, nano-sized $CaCO_3$ improved the modulus of ABS while maintaining or even increasing its impact strength. SEM analysis showed that nano-sized particles were dispersed in the composites at significantly smaller sizes than their micron-sized equivalents. The main causes of nano $CaCO_3$/ABS composites' improved mechanical properties are thought to be their greater interfacial area and cavitation-induced shear yielding in the ligament.

Various inorganic Nano fillers were compounded with ABS in [45], to obtain different nanocomposite filaments to evaluate their effects on mechanical anisotropy, mechanical strength, and thermal stability of the 3D printed samples. The filler materials were nano $CaCO_3$, nano Montmorillonite, nano SiO_3, and nano MWCNTs for the individual filaments to be fabricated and specimens to be tested. In conjunction with slight amounts of nanofillers, all of the mechanical parameters of the composite samples improved significantly when compared to pure ABS counterparts. An improvement in the tensile strength and flexural strength of pure ABS was obtained from 29.5 to 37.1 MPa and from 54.8 to 64.2 MPa respectively when nano montmorillonite was incorporated into the ABS matrix. On the other hand, the addition of nano $CaCO_3$ had the most powerful effect on mechanical anisotropy reduction among other additives making a change from 42.1% to 23.9%.

As a recent study [46] investigated the effects of internal architecture on the fracture behavior of 3D printed ABS/$CaCO_3$ nanocomposite samples. The melt-blending method was used to create the nanocomposite filaments. The standard tensile, compact tension, and special fracture test samples, referred to as Arcan specimens, have been 3D printed using four alternative internal designs and consistent extrusion conditions. Arcan samples underwent mixed-mode fracture tests using a uniquely designed fixture. The fracture toughness of such materials was determined by finite element calculations utilizing the J-integral approach. The addition of $CaCO_3$ nanoparticles has caused a significant increase in the fracture loading of the samples. Although this increase was not uniform for all filling patterns, it was more noticeable for samples with linear and triangular structures. Fractographic observations show that the addition of $CaCO_3$ nanoparticles to the matrix increases the fracture loading by producing uniformly distributed microvoids as a result of the blunting effect of the nanoparticles and a 3D stress state at the crack tip in samples with linear and triangular structures. Fractographic observations show that the addition of $CaCO_3$ nanoparticles to the matrix increases the fracture loading by producing uniformly distributed microvoids as a result of the blunting effect of the nanoparticles and a 3D stress state at the crack tip in samples with linear and triangular structures.

The subject of [47] was investigating the effect of additive content, normal load, and sliding speed parameters on the tribological behaviors such as coefficient of friction (COF) and wear rate of ABS specimens fabricated with filaments compounded with micron-sized $CaCO_3$ particles. The experimental design was based on Taguchi L_{27} orthogonal array and the experiments were conducted with a multi-tribotester (block-on-roller configuration). Employing grey relational analysis, the ideal design parameter combination for a specified wear rate and minimum coefficient of friction was evaluated. It was discovered that 5% filler content, 35 N of load, and 120 rpm of speed make up the ideal parameter combination. ANOVA is also utilized to determine the most important element that influences the tribological qualities. The normal load is the most important element, followed by sliding speed and filler content.

2.2.6 Studies concerning the use of Carbon Black as reinforcement for various nanocomposite filaments used in the FDM process

The other nanoparticle additive employed in this thesis is Carbon Black. Below are the studies conducted using Carbon Black additives to form composite filaments for the FDM method.

As a recent study, [48] blended thermoplastic polyurethane (TPU) with Carbon Black particles (CBP) to fabricate composite filaments to be used in the FDM method. These filaments were employed to 3D print flexible strain sensors with 88% TPU and 12% CBP content. Various unique periodic sensor configurations were designed to maximize sensor flexibility. The experimental test findings were roughly in agreement with the conclusion drawn from the geometric structural calculation and numerical simulation for sensitivity evaluations of the flex sensors with various configurations. The as-printed sensor's successful sensing abilities with its S-shaped zigzag periodic design and TPU film substrate were demonstrated successfully, demonstrating the sensor's viability for monitoring human health.

As a study concerning Carbon Black [49] purchased a commercially available PLA filament reinforced with Carbon Black (CB) called conductive PLA and the mechanical and electrical properties of the material were investigated. Tensile test specimens were 3D printed and tested with the purchased filament and additionally, the electrical resistivity of the filament was measured with various lengths. Test results revealed that conductive PLA only displays 66% of the value of conventional PLA in terms of tensile strength. On the other hand, in terms of electrical resistivity, it was observed that if the extrusion temperature during printing is increased the resistivity value decreases. On the other hand, the temperature at which the resistance measurements were made also affects the resistance values. When the ambient temperature value increases the resistance value also increases.

As a novel study [50] investigated the deposition of polymers on synthetic fabrics using 3D printing as a novel printing technology. Using the fused deposition modeling (FDM) technique, the adhesion of polymer and nanocomposite layers that were 3D printed directly onto textile fabrics were analyzed. The polymers were printed in different series of experimental designs: nylon on polyamide 66 (PA66) fabrics, polylactic acid (PLA) on PA66 fabric, PLA on PLA fabric, and finally Nano sized carbon black/PLA (CB/PLA) and multi-wall carbon nanotubes/PLA (CNT/PLA) nanocomposites on PLA fabrics. The findings revealed that several 3D printing parameters including extruder temperature, platform temperature, and printing speed, may significantly affect the force of polymers' adherence to textiles during direct 3D printing. The results showed that the adhesion force of PLA and PLA nanocomposites including PLA carbon black was high on the textiles.

In order to investigate a different aspect of the nanocomposite filament such as tribological properties [51] employed PLA as the matrix and Carbon Black (CB) and Alumina (ALM) nano fillers. Composite filaments were fabricated in various combinations of ALM and CB addition ratios such as 0/100, 25/75, 50/50, 75/25 and 100/0 included in PLA matrix of total 3% in weight. Thermal, mechanical and tribological properties of the nano composites were evaluated related to the amount of additives and their ratios. According to thermogravimetric analyses, each nanofiller enabled a gradual improvement in thermal stability of the composites. Improved mechanical and wear characteristics were demonstrated by the nanocomposites containing 25% wt ALM and 75% wt CB, indicating that the two nanofillers have good function together and that CB might function as a compatibilizer between PLA and ALM.

As another aspect of the nanocomposite material to be explored, [52] studied microwave absorption performance and filaments of polypropylene (PP) reinforced with carbon black (CB) was fabricated to see the effect of CB% in weight on the mentioned characteristic. The results exhibited excellent microwave absorption and a broad effective bandwidth when 10% CB in weight was added into the matrix as long as the particles were uniformly distributed in the matrix with negligible agglomeration. The study showed that using such nanocomposite filaments for the FDM method in the production of microwave absorption materials industry enables great flexibility in designing and manufacturing these products.

As related to this thesis, we should also consider the studies carried out to investigate various properties of the composite filaments having ABS as the matrix material and Carbon Black as the reinforcement material.

The use of Carbon Black additive particles is best known for their effect on electrical properties and [53] aimed to 3D print a low-cost concave capacitive sensor with the use of an ABS/CB nanocomposite filament. The sensor was 3D printed with the fabricated ABS/CB nanocomposite filament and the sensor's capacity to predict the void fraction of water-air two-phase flow was tested by measuring the capacitance values. These values were also compared to the capacitance values of conventional copper sensors. The researchers also investigated the influence of printing parameters such as the thickness and width of the sensors on the capacitance value. A prediction model was developed and validated by using regression analysis.

As a very recent further study [54] investigated the electromagnetic shielding (EMI) performance of 3D printed ABS/CB composites. The test samples were 3D printed with thickness values ranging from 0.2 mm to 2 mm and they were tested in the frequency range of

1 GHz – 12 GHz values. The maximum effectiveness in terms of EMI shielding was obtained in the specimen having a 2 mm absorber thickness at a 2.4 GHz frequency value. The mechanical and electrical properties of the composite were characterized and results showed that the increase in CB content in the composite provided an increase in electrical conductivity while this increase caused a reduction in tensile and impact strength values.

As a similar topic in the field of electrics [55] studied the resistivity and resistivity anisotropy of 3D printed ABS/CB composite parts. The addition of CB into the ABS matrix affects the resistivity of the composite however when the samples are 3D printed the printing parameters play a crucial role in resistivity and its anisotropy. For cubic samples, it was investigated how the layer thickness, raster width, and air gap of the FDM process parameters affected the resistivity in both the vertical and horizontal directions. An impedance analyzer was used to assess the resistivities of printed components in various parameter configurations. Finite element models were then developed to examine the connection between resistivity and interior structure. It was concluded that resistivity values could be arranged in certain ranges in both horizontal and vertical directions along with resistivity anisotropy alteration in a certain range too. This would enable manufacturers to 3D print complex-shaped parts with desired resistivity and resistivity anisotropy values.

In [56] an ABS/CB nanocomposite filament was fabricated and the strain-sensing characteristics of the 3D printed specimens were investigated. To create a functionalized composite that can identify changes in stress or strain in engineering elements, the impact of printing configuration on the strain-sensing behavior of the composite was examined. The measurements throughout sample thickness were determined to be the most appropriate for generalizing the samples' resistivity. The researchers deduced that the printing parameters influenced the strain-sensing behavior of the specimens and researchers considered variations in raster angle and gap width to find the best combination of these parameters in strain-sensing characteristics. After numerous testing, having a combination of using a negative gap between rasters and a raster angle of +/- 45^{o} configuration significantly intensified the detected signals thus making the combination most suitable for sensing processes.

2.2.7 Studies investigating the free vibration behavior of composite cantilever beams manufactured with methods other than FDM

Similar to our study [57] investigated the damping and stiffness characteristics of carbon nanotube-epoxy composite cantilever beams that are designed to be used in environments subjected to structural vibration. The effect of nanotube fraction, nanotube type and frequency dependence on natural frequency and damping ratio was investigated. Both single-walled and multi-walled nanotubes were mixed with epoxy resin to manufacture composite cantilever beams in different nanoparticle weight fractions. It was evident that the improvement in damping ratio values was far more significant than the improvement in natural frequency values. It was also observed that multi-walled carbon nanotubes provided better improvement in damping ratio than the single-walled carbon nanotube particles. Damping ratio values were increased as high as 700% with the use of multi-walled carbon nanotubes compared to the pure epoxy beam.

As a resembling study [58] investigated the damping behavior of simple and sandwich beams of Aluminum, epoxy and various CNTs in free vibration. In order to compare the behavior of composite beams, simple and sandwich beams containing just neat epoxy were also manufactured. A weight fraction of 5% CNTs is used in every beam and free vibration tests were carried out. Damping ratio values were obtained by using the logarithmic decrement and half-power bandwidth methods. The results indicated that the best enhancement in damping ratio values were obtained in specimens containing short aspect ratio multi-walled non-functionalized nanotubes.

Furthermore [59], investigated the damping characteristics of CNT reinforced epoxy cantilever beams by performing numerical and experimental calculations. To predict the frequency-dependent damping properties of CNT reinforced epoxy nanocomposites and include them into the finite element model for composite beams, a modified Biot model is presented. The proposed finite element model predicts the natural frequencies and modal damping ratios of epoxy beams reinforced with CNT. Following fabrication, CNT reinforced epoxy beam specimens are used for dynamic mechanical analysis and vibration tests. It was concluded that the offered Biot model is more accurate than the original one in predicting the loss factors of CNT reinforced epoxy nanocomposites according to comparison studies made between theoretical and experimental data. It is discovered that when the CNT weight ratio increases, the damping ratios related to the first three vibration modes of composite beam specimens initially improve and subsequently decrease. The highest value of the first mode damping ratio with 0.4 wt% CNT reinforcement is 0.591%, which is 41% better than that of pure epoxy.

2.2.8 Studies investigating the free vibration behavior of pure and composite parts manufactured with the FDM process

As stated previously, this study focuses on the fabrication of individual nanocomposite filaments with CB reinforcement and $CaCO_3$ reinforcement particles on the ABS matrix. Other than the studies mentioned above the effect of these nanoparticles on the vibrational characteristics such as natural frequency and damping ratio values were investigated. There is a gap in the literature about ABS/CB and ABS/$CaCO_3$ composites used in the FDM method in terms of their effects on vibrational properties. Since there is no such study on this particular topic, it would be beneficial to review similar studies carried out on the free vibration characteristics of pure and composite parts with the FDM method.

As one of the similar studies regarding vibration [60] focused on the influence of printing orientation on the vibrational characteristics of 3D printed PLA cantilever beams. The main purpose of the study was to estimate the complex modulus of the 3D printed cantilever beams with respect to the printing orientation. A dynamic mechanical analyzer was employed to measure the mechanical properties of the cantilever beams printed in various printing directions. Temperature-dependent complex modulus and natural frequency values of the printed beams were estimated employing the curve fit method. Finally, the variability in the vibration behavior was observed as a function of the printing orientation.

Pure PETG and carbon fiber-reinforced PETG composite filaments were used in [61] where compression, cyclic compression, Nano-indentation, and modal tests were carried out with the printed specimens to find the effects of carbon fiber inclusion in the matrix. The composite filament used in the study contained 20% carbon fiber and both specimens were printed with a commercial printer with the same printing parameters used. According to test results, there was a significant decrease in compressive strength value in Carbon/PETG specimens compared to pure PETG specimens. On the other hand, in terms of the vibration behavior of the specimens, it was observed that the inclusion of carbon fiber resulted in an increase in the frequency value in the fundamental mode. Aside from that, it was concluded that carbon fiber content caused a decrease in the damping value of the specimens.

3D printed polymeric functionally graded plates with varying stiffness and density through their length were fabricated in [62] to investigate the free vibration behavior studied for. An analytical model was used based on the Higher Order Sher Deformation Theory and the problem was modeled using ABAQUS FE software. To verify the numerical results, the plates were 3D printed and experiments were carried out on the plates with a portable digital vibrometer to measure the first natural frequency values. Results showed that the presented analytical formulation gives sound results when compared to physical test results.

Numerous cantilever beam specimens were 3D printed with varying parameters such as raster angle, air gap, build orientation, and the number of contours as input variables in [63] and machine learning algorithms were employed to develop a prediction model for natural frequency values of the beams. For the experimental design procedure, the I-optimal design of experiments was used and an artificial neural network (ANN) model was trained to employ the Bayesian regularization function. This trained model was validated by multiple physical vibration test runs of the 3D printed cantilever beams and the model was able to make predictions having almost 5% error. It was deduced from the test results that having the build orientation along the y-axis, choosing a lower raster angle and a lower air gap value along with having additional contours results in higher natural frequency values in the test specimens.

PLA was used as the matrix material and Graphene as the reinforcement material in [64] to investigate the mechanical and dynamic properties of the 3D printed nanocomposite specimens. Test specimens of pure PLA and PLA/Graphene composite form having 10% Graphene in weight were 3D printed with other parameters left constant with a commercial

FDM machine. The characterization of the specimens was carried out by performing compression tests, cyclic compression tests, nanoindentation tests, and modal tests. Test results revealed that the Graphene inclusion in the PLA filament led to an improvement in the modulus, strength, and hardness values of the specimens. In terms of vibrational characteristics, 10% Graphene content increased the natural frequency value and damping ratio of the specimens compared to their pure PLA counterparts.

The blending of two thermoplastic polymers was studied in [65] where PC and ABS were mixed and melt extruded for filament fabrication and 3D printed specimens from this material were characterized in terms of mechanical and vibrational properties. The PC-ABS specimens were compared to pure ABS and pure PC specimens in tensile tests and the fractured surfaces were examined via Field Emission Scanning Electron Microscope (FESEM) to observe the bonding between layers and the fracture that occurred in the raster. Also, three types of beam test specimens were prepared to perform modal analysis for natural frequency detection. Test results showed that compared to pure ABS and PC, PC-ABS blend specimens have higher elastic limits and load-carrying capacity while the natural frequency values of the PC-ABS blends are also higher than the other specimens.

PETG was melt extruded with short fiber carbon [66] and a composite filament was fabricated. Test samples were 3D printed with pure PETG and PETG-Carbon fiber (CF) composite filaments and tensile tests were performed. According to these tensile test results, the modulus of elasticity of the PETG-CF specimens was 29% higher and the ultimate tensile strength value was 12% higher than that of pure PETG specimens. Vibration tests were also performed on 3D printed cantilever beam specimens and PETG-CF specimens displayed natural frequency values of 17% higher than the pure PETG samples. The natural frequency values acquired from the tests were also validated by using the tensile test values and incorporating them into ANSYS modal analyses of the cantilever beam models.

A novel approach was exhibited in [67] where the effect of manufacturing micro-structure on the elastic and vibrational properties of 3D printed parts employing FDM was investigated. Three distinct material directions of fiber direction, intra-layer direction, and inter-layer direction were identified to characterize the orthotropic behavior of FFF 3D printing material based on the findings of scanning electron microscopy. A constitutive model representing the orthotropic elastic 3D printing material was built employing the experimental results and plane stress rotation formula. The findings of the experiments (which involved 27 various types of specimens) indicate that the highest difference in Young's moduli between the different directions of materials is 1104.684 MPa, which is even greater than Young's modulus in the intra-layer direction. Other than tensile specimens, test specimens of plates having six different printing directions and three different layer thicknesses were 3D printed and their natural frequencies were determined experimentally. These specimens were also modeled in computer software and the natural frequencies were also calculated numerically. According to simulation data, the first five fundamental natural frequency modes were considered, and the highest differences in natural frequencies across plates with various printing orientations are 10.645 Hz, 39.588 Hz, 66.710 Hz, 123.780 Hz, and 185.720 Hz. When compared to the first five out-of-plane natural frequencies of these plates, these discrepancies are rather considerable. To confirm the accuracy of the simulation procedure, vibration experiments using FFF 3D printing plates also were conducted. All relative errors of the natural frequencies between the simulation and the experimental findings are discovered to be extremely small. As a result, one may validate the impacts of manufacturing microstructure on the vibration characteristics by using finite element models that are accurate enough.

A parametric FE model for simulating the particular impact of infill-related factors on the natural first frequency of cantilever beam-like sections was presented and established in [68]. The impact of infill density and infill line width on natural frequency was investigated. Using the chosen set of parameters, a FE script was developed and executed which automates the construction of the model geometry to obtain the calculated natural frequency value. Test specimens were 3D printed according to the developed parametric model and these specimens were physically tested for natural frequency detection. To validate the developed script, the modal analysis findings were contrasted with the experimental results. A linear relationship between the weight of the part and the first natural frequency was derived based on the experimental findings. This is also in agreement with cantilever beam theory and it was a concluded that infill percentage, which is directly related to the mass of the 3D printed part, is the most influential parameter among printing parameters. As the number of contours decreases the natural frequency value also decreases according to the experimental findings. It was also inferred from the test results that the infill line width and infill pattern did not influence the natural frequency.

Developing a numerical model for estimating the vibration fatigue life of 3D printed y-shaped PLA specimens was the subject of [69]. Three different spectral methods were used in numerical calculations and elastic modulus and damping ratio values of the material were obtained by physically performing dynamic mechanical analysis. These constants were used in numerical modal calculations. Furthermore, to obtain the S-N curve of the material, dog bone specimens were 3D printed and tested with a tensile fatigue tester. To validate the numerical model based on previously used vibration fatigue models for metal materials in the literature, physical tests were also carried out. Y-shaped PLA specimens were printed and tested with an electrodynamic shaker till the failure was observed. Experimental results and numerical results were compared and a maximum of 10% error was detected.

As can be seen from the review above, no studies were carried out to investigate the effect of CB and $CACO_3$ content in 3D printed ABS nanocomposites on the free vibration characteristics. Our research aims to contribute to the literature with its findings.

3. MATERIALS AND METHODS

3.1. Production of the nanocomposite filaments

To manufacture the cantilever beams for testing, nanoparticles and ABS granules had to be procured and with the use of these materials, filaments had to be fabricated to be used in the 3D printer as the raw material. First, ABS granules were purchased from a plastic company named Epsan Plastik Ltd. (Turkey). The density of the ABS granules was 1.08 g/cc and the melt flow index of the granules was approximately 6.8 g/10 mins (230 ^{o}C / 2.16 kgf according to ISO 1133-1/2). The glass transition temperature of the ABS granules was 105 ^{o}C. The ABS granules can be seen in Figure 3.1.

Figure 3.1. Pure ABS granules procured from the market

The ABS granules were blended with two types of nanoparticles to fabricate two different nanocomposite filaments, one being Calcium Carbonate ($CaCO_3$) and the other Carbon Black (CB). Calcium Carbonate nanoparticles with the crystalline structure of rhombohedral shape and a particle size range of 40 – 80 nm with an approximately 40 m^2/g specific surface area value were purchased from a Jiangsu XFNANO Materials Tech Co. Ltd. Company (China). There weren’t any modifications performed on the nanoparticles for filament production.

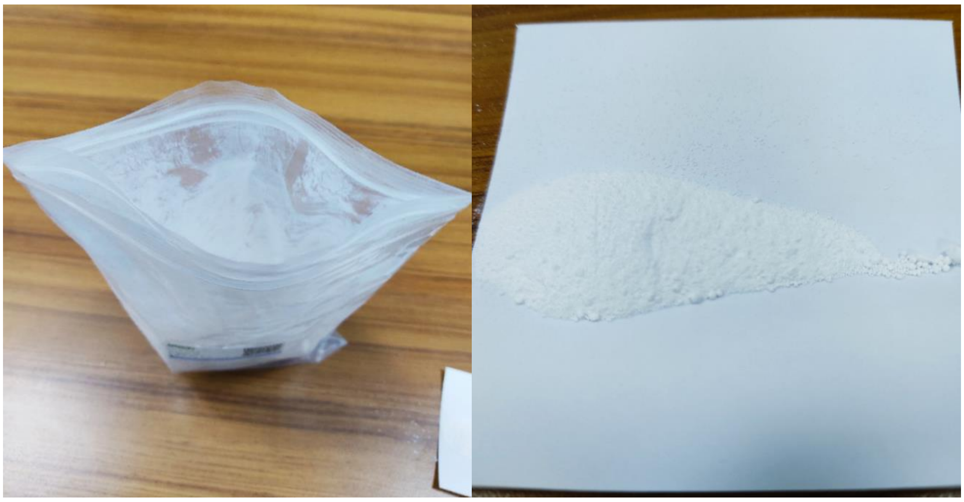

Figure 3.2 $CaCO_3$ nanoparticles used in the filament production

Carbon black nanoparticles were also purchased from Jiangsu XFNANO Materials Tech Co. Ltd. Company (China). The size of Carbon Black nanoparticles was between 35-40 nanometers. Nano Carbon Black particles can be seen in Figure 3.3.

Figure 3.3. Carbon Black nanoparticles used in the filament production

For the production of the nanocomposite filaments containing different weight fractions of $CaCO_3$ and CB nanoparticles, a long procedure was undertaken. As seen in Figure 3.4, firstly, the nanoparticles and ABS granules were dried in a vacuum oven. This is done to avoid any water content in both materials, especially for ABS, since the material is hygroscopic. If not stored in proper conditions, ABS filaments can get high amounts of moisture content causing the 3D print quality to decrease in many aspects. After the drying session, granules and nanoparticles are mixed in a mechanical mixer to get a uniform distribution of the particles. After a certain time of mixing, the mixed content is loaded in the hopper of a twin extruder for master batch preparation of the filaments. Here the ABS granules mixed with 5% nanoparticles are melt extruded in the extruder. The four heaters of the twin extruder were set to 200, 220, 220, and 230 ^{o}C temperatures. The extruded filament having a 5% nanoparticle content was shredded in a mechanical shredder where granules of the main compound called the master batch were obtained by the pelletization process. The layout of the master batch preparation process can be seen in Figure 3.4. The max weight percentage content of nano-$CaCO_3$ was 5% because the higher content of $CaCO_3$ nanoparticles caused a brittle behavior in the filaments making the winding process very hard.

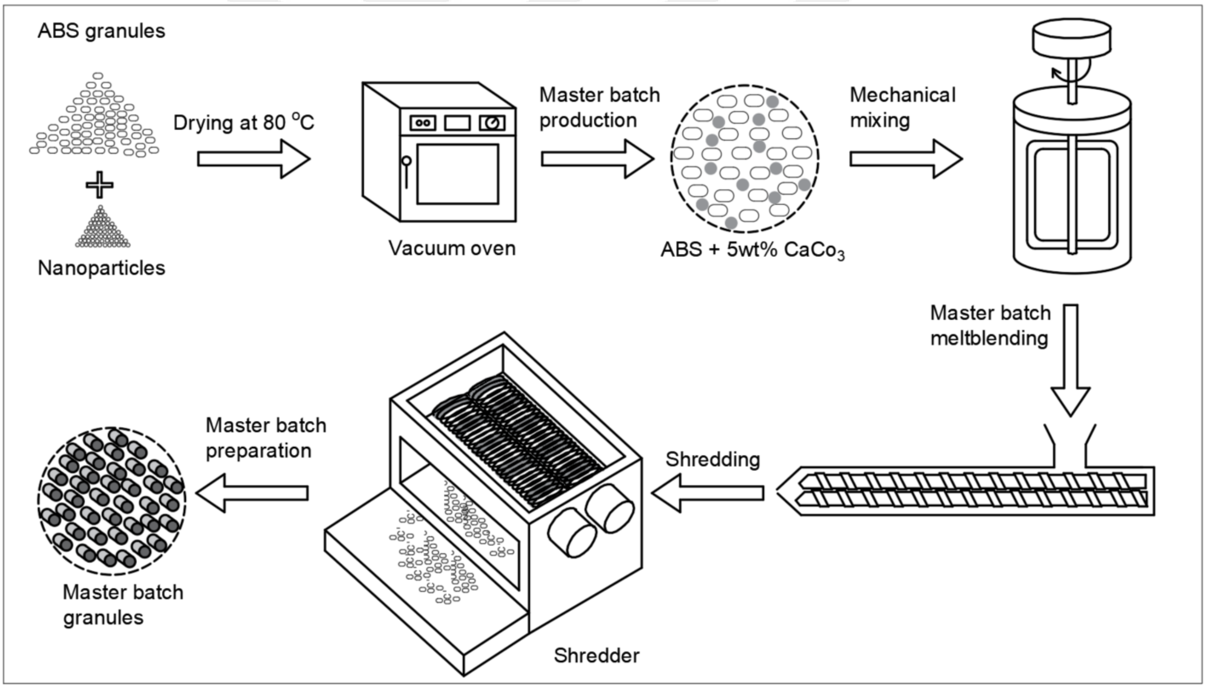

Figure 3.4. The preparation process of the master batch granules for nano $CaCO_3$ filament

Besides the agglomeration of the nanoparticles led to a deterioration in the mechanical properties of the filament material.

Once the master batch was obtained, filaments having 1%, 2% and 3% and 5% nanoparticle content in weight could be obtained by mixing the master batch with a certain calculated weight of pure ABS granules. After mixing the master batch with pure ABS granules, the mixture was dried in the vacuum oven to avoid any moisture content in the mixture. The dried mixture was then fed to the hopper of the single extruder and the filaments with 1.75 mm diameter that was used in the 3D printer were wound on spools. All heaters of the filament extruders were set to 210 ^{o}C being the optimum temperature after some trial extrusions. The diameter of the filaments was continuously monitored with the help of a digital thickness gauge with rollers. Preparation of the final nanoparticle filament to be used in the 3D printing process in Figure 3.5.

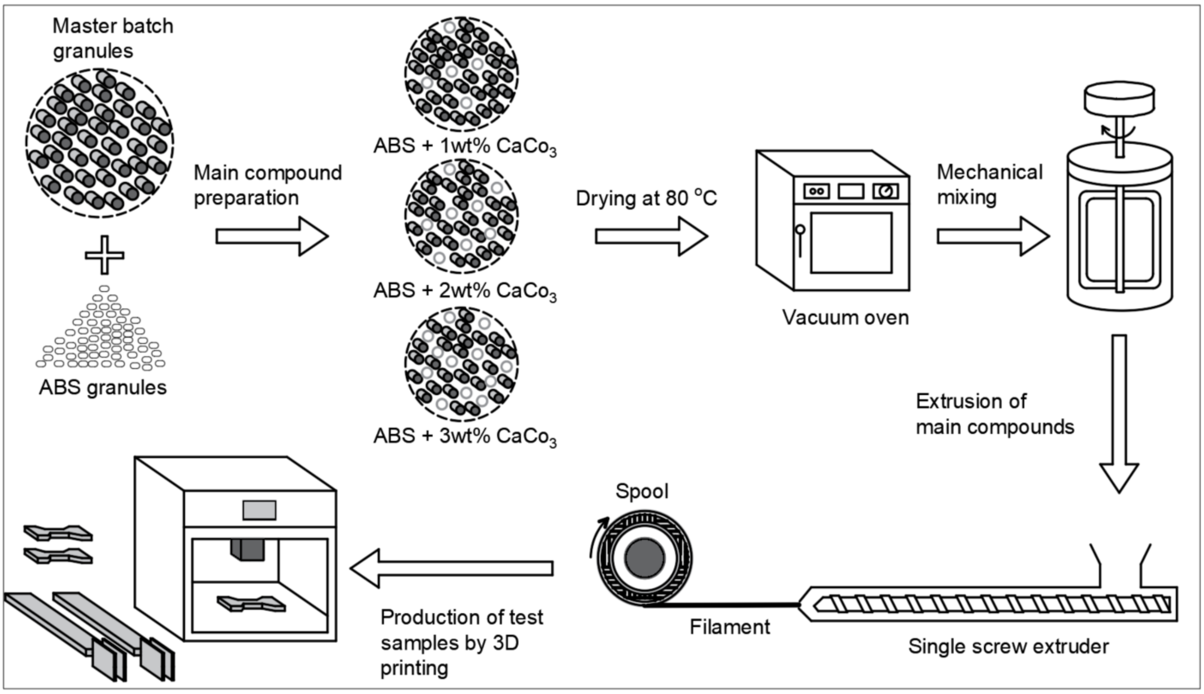

Figure 3.5. Preparation of the final nanoparticle filament to be used in the 3D printing process

The setup for final extrusion and filament winding on the spool by the single extruder can be seen in Figure 3.6. The roller thickness gauge used for monitoring the diameter of the extruded filament can be seen in Figure 3.7.

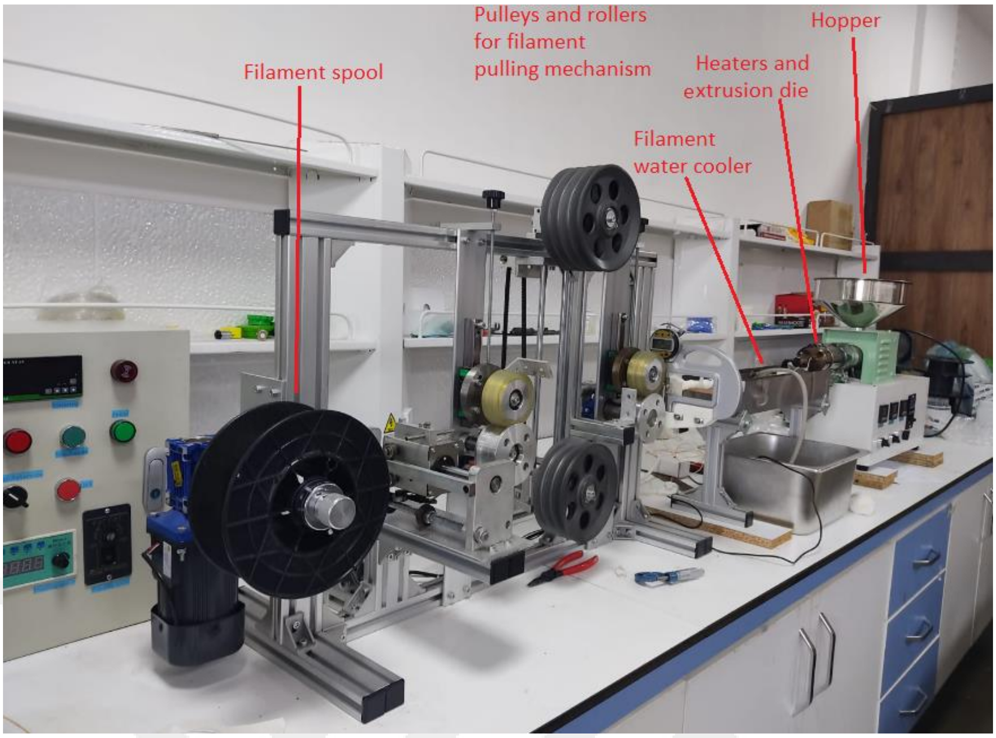

Figure 3.6. Filament extrusion and winding setup

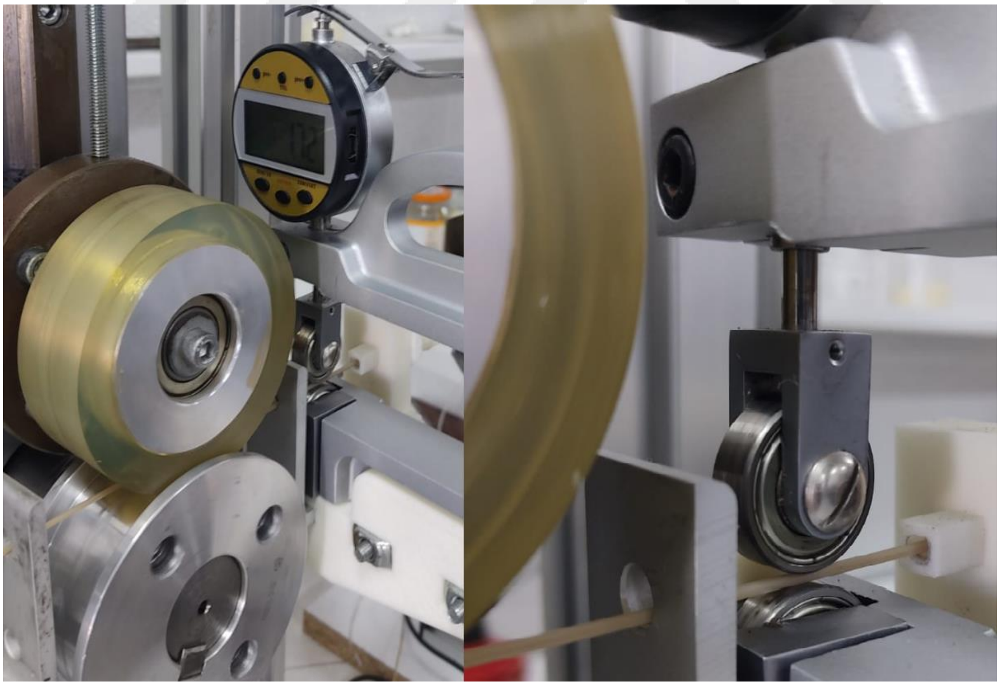

Figure 3.7. Filament diameter measurement in the extrusion process with roller thickness gauge

The process was carefully monitored to obtain the 1.75 mm filament diameter. If this value is not attained uniformly with some tolerance, the nozzle of the 3D printer cannot operate properly leading to the failure of the printing operation. The spool of an ABS filament containing nano-$CaCO_3$ produced in-house can be seen in Figure 3.8.

Figure 3.8. Filament spool fabricated with 3wt% $CaCO_3$ nanoparticles

The same production process was used for ABS filaments containing CB nanoparticles. The weight percentage of the various filaments with CB nanoparticles was 0.3%, 0.6%, 1%, and 2%. The four heaters of the twin extruder were set to 230, 240, 240, and 220 ^{o}C temperatures. The extruded filament having a 2% nanoparticle content was shredded in a mechanical shredder just like the $CaCO_3$ samples as explained above. After the master batch was obtained by the pelletization process they were dried in a vacuum oven and extruded in a single screw extruder.

The filaments were wound on a spool and used for the 3D printing of test samples. The maximum weight percent of CB nanoparticles was kept at 2% since nanoparticle content more than this value caused the filament to be brittle and made the extrusion of the filament impossible due to unstable winding. An ABS filament containing Nano CB particles can be seen in Figure 3.9.

Figure 3.9. Filament spool fabricated with ABS + 2wt% CB nanoparticles

One filament was also fabricated from pure ABS granules only to compare the effect of nanoparticle content in blended filaments on vibrational and mechanical properties. The filament was produced only using the single screw extruder since there were no nanoparticles to be included.

3.2. Production of the cantilever beams

The cantilever beams and tensile test samples were 3D printed with filaments containing CB and $CaCO_3$ nanoparticles. For the 3D printing process, Flashforge Creator 3 (Zhejiang Flashforge 3D technology Co, LTD ® China) brand 3D printer was used. The printer is a double extruder printer that is a known brand in the industry. The actual printer used in the production of the test samples can be seen in Figure 3.10. Technical specifications of the Flasforge Creator 3 printer are given in Table 1.

All the beam samples were designed with CAD software and saved in '.stl' format which was exported to the software named Flashprint, which is a software that Flashforge Creator 3 is compatible with. The printing parameters used for the production of the beams and tensile test specimens are given in Table 2.

Figure 3.10. Flashforge Creator 3 3D printer used for the production of test specimens

Table 3.1 Flashforge Creator 3 Technical Specifications

Number of Extruders	2, Independent
Extruder Diameter	0.4 mm
Maximum Extruder Temperature	300 ^{o}C
Maximum Platform Temperature	120 ^{o}C
Printing Speed	10-150 mm/s
Supported Filament Types	PLA/ABS/PVA/PETG/HIPS/PA-PC/WOOD/ASA/PA-CF/PA-GF
Print Volume	300*250*200 mm
Layer Resolution	0.05-0.4 mm
Print Resolution	$\pm$0.2 mm

Table 3.2. The printing parameters that were set for the 3D printing of the nano-$CaCO_3$ specimens

Nozzle Temperature	300 ^oC
Bed Temperature	90 ^oC
Printing Speed	60 mm/s
Filament Feed Rate	1.25 mm/s
Layer Thickness	0.30 mm
Filling Ratio	60 %
Printing Pattern	Triangular

The 3D printed cantilever test specimen of pure ABS filament can be seen in Figure 3.11. The filament that was used for the production of pure ABS cantilever beam was produced in house with pure ABS granules by material extrusion.

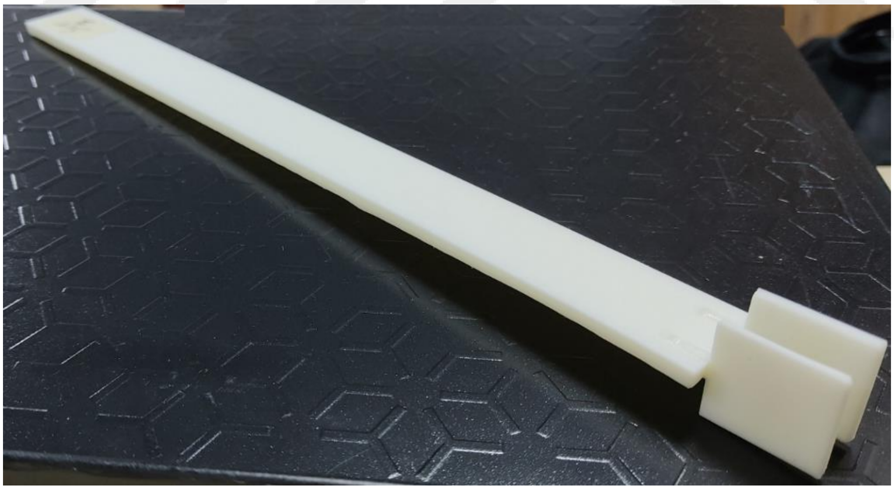

Figure 3.11. Cantilever beam of pure ABS fabricated by the 3D printer

Cantilever beam test specimen of ABS + 1wt% CB can be seen in Figure 3.12. The tensile test specimen geometry that is viewed in the Flashprint software can be seen in Figure 3.13. The tensile test specimen of pure ABS that was 3D printed can be seen in Figure 3.14.

Figure 3.12. One of the nanocomposite cantilever beams of ABS + 1wt% CB

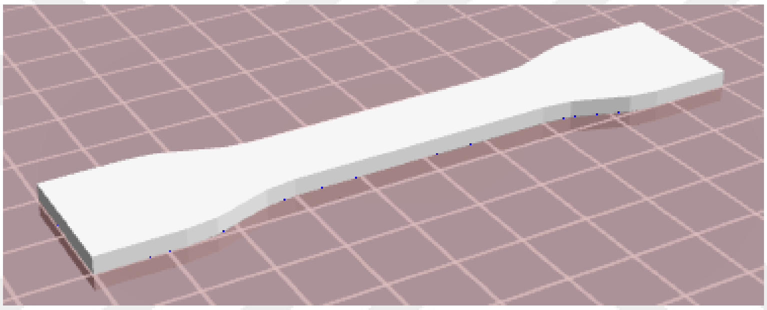

Figure 3.13. Tensile test specimen viewed in Flashprint software

Figure 3.14. Tensile test specimen of pure ABS fabricated by the 3D printer

For every weight fraction of ABS + CB and ABS + $CaCO_3$ beams along with the pure ABS beam, three specimens for each weight fraction was 3D printed for vibration testing. Every specimen was tested 3 times and average values of the results were calculated.

3.3. Experimental setup

For the experimental part of the thesis, Nano composite cantilever beams were 3D printed and tested with test equipment designed to test the free vibration of steel cantilever beams. The test gear is Tecquipment® TM166 (TecQuipment Ltd.) model with the name "free vibrations of a cantilever". This is an educationally designed testing equipment used in the Alparslan Türkeş Science and Technology University laboratories. The test setup can be seen in Figure 3.15.

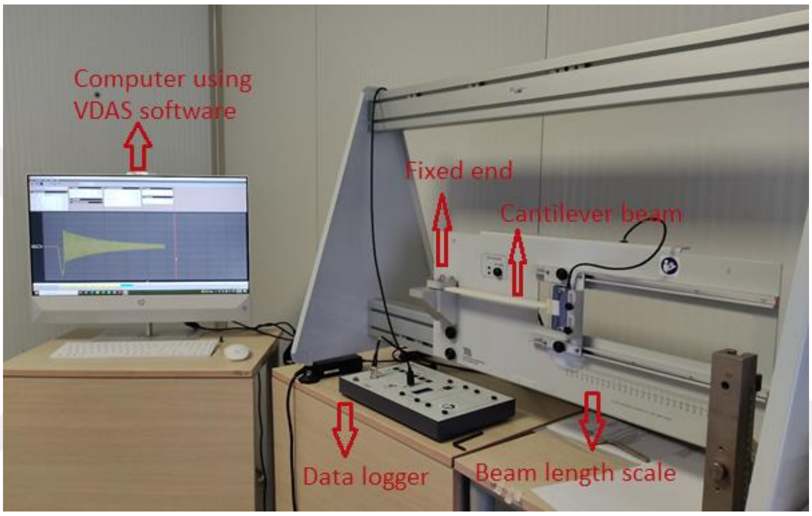

Figure 3.15. Test setup used for the vibration tests of the 3D printed nanocomposite cantilever beams

TM166 has a standard cantilever beam made of tool steel and the testing gear uses a magnetic sensor close to the end tip of the specially designed cantilever beam. As can be seen in Figure 3.16. the tip of the beam is split into two pieces and is rotated 90 degrees horizontally.

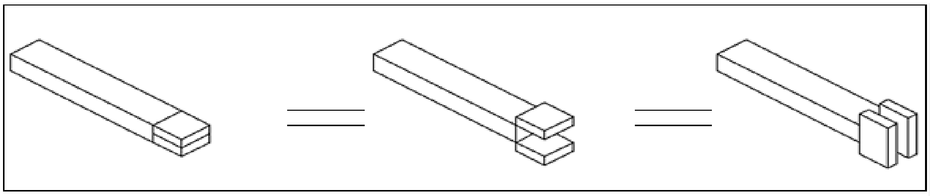

Figure 3.16. Cantilever beam belonging to the vibration test equipment which is considered equivalent to the standard beam

This is done in purpose so that the magnetic sensor can be positioned in between the horizontal steel faces of the tip of the cantilever beam seen in red color. The steel beam used in the test equipment can be seen in Figure 3.17.

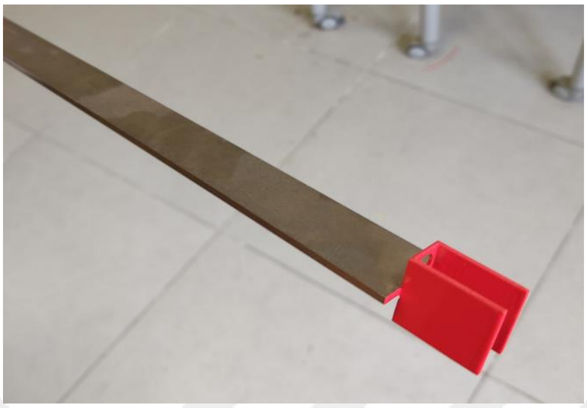

Figure 3.17. Original steel cantilever beam used on the test equipment

The sensor is a non-contacting displacement sensor that detects the movement of the steel faces of the tip of the cantilever beam. This is done by the induction of a small magnetic field on the tip of the beam and the strength of the magnetic field is almost linearly proportional to the displacement value. In fact, the sensor genuinely measures the angular change in displacement but for small angles, the linear displacement is equivalent to the angular displacement according to simple harmonic motion theory. As long as the tip of the cantilever beam is positioned within the dotted lines of the sensor, the results are accurate and linear. The correct positioning of the cantilever beam can be seen in Figure 3.18.

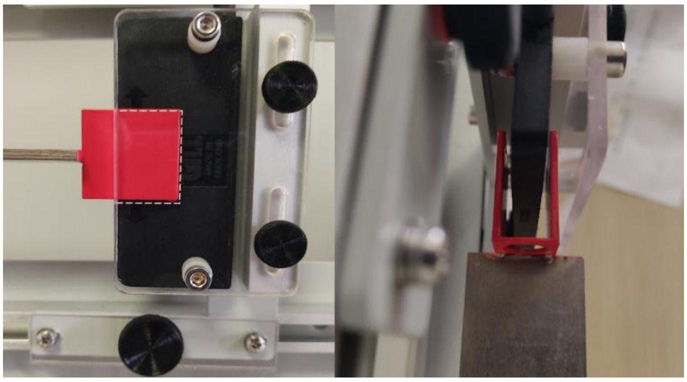

Figure 3.18. The position of the activators relative to the sensor when the beam is fitted correctly

The design of the tip of the cantilever beam can be included in the effective length of the cantilever beam and is considered as a part of the beam which will not contradict the theory. The position of the sensor can also be adjusted both horizontally and vertically so that more accurate results can be obtained. There is also a knob with a LED light that is used for precise vertical position calibration of the beam displacement measurements. For every test run, the position of the cantilever beam should be calibrated to zero position to get more precise measurements.

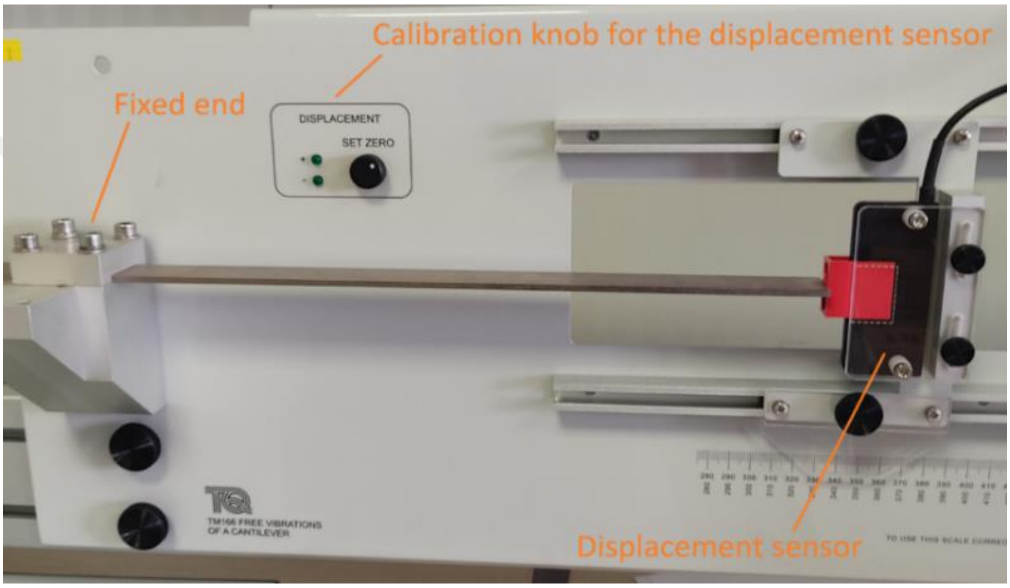

Figure 3.19. Original test setup with the steel cantilever beam assembled

To use this equipment in the free vibration tests, the cantilever beam design was adapted to the dimensions and the special geometry of the test setup. The beam was modeled in ANSYS ® Spaceclaim 3D design modeler software the cantilever beam can be seen in Figure 3.20.

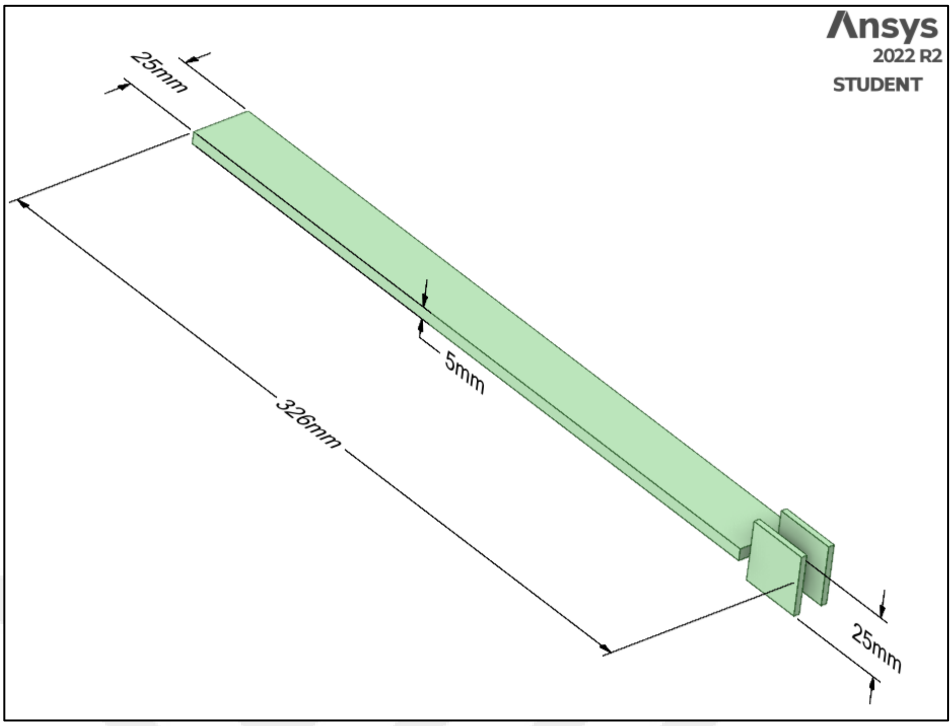

Figure 3.20. Modelled cantilever beam in ANSYS ® Spaceclaim software

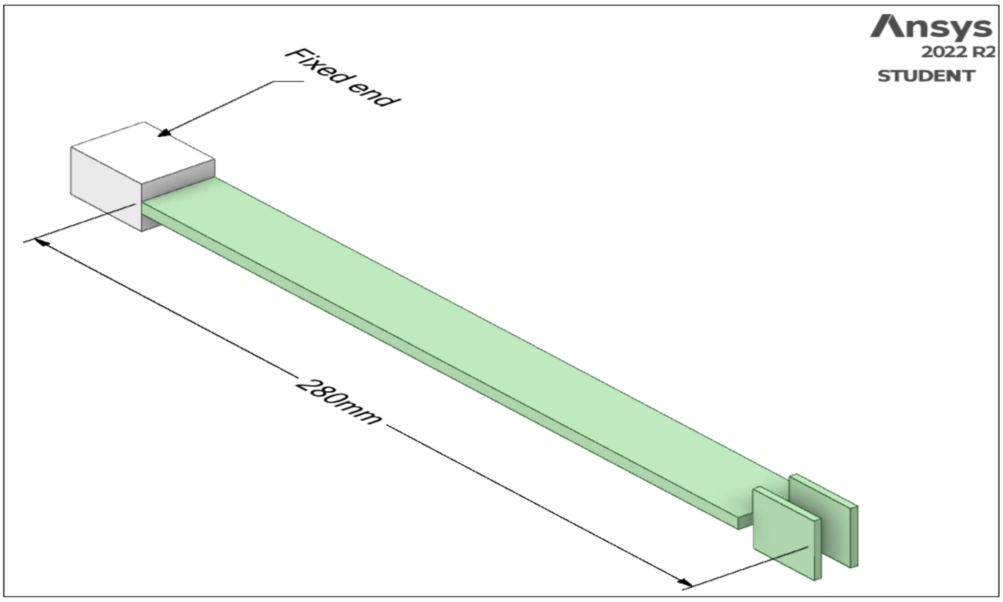

Figure 3.21. Cantilever beam assembled to the test equipment with an effective beam length of 280 mm which is the length that is the overhang part from the fixed end

As the ASTM E1876 standard suggests, the thickness and the width of the rectangular cross-section of the beam should at least have a 1:5 ratio respectively. The thickness of the test specimens is 5 mm while the width is 25 mm which satisfies the 1:5 ratio suggested. Another suggestion of the standard is that the ratio of the length of the cantilever beam dimension to the minimum dimension of the cross-section should be at least 5. The standard assumes that ratios of 20 to 25 are preferred for calculations to be easy. In our case, this ratio is 280 mm beam length divided by 5 mm minimum cross-section dimension which makes 56. The 3D printed prototype was assembled into the testing equipment to check the dimensions, especially the clearance between both tips and the magnetic sensor. The assembled prototype beam on the test rig can be seen in Figure 3.22.

Figure 3.22. Prototype cantilever beam assembled to the test equipment

Since this thesis is concerned with ABS cantilever beams, these beams are not able to interfere with the magnetic field induced by the sensor because they are built up of a thermoplastic material. Therefore, sheet metal parts working as an activator for the sensor were assembled to the inner surfaces of the tip of the designed cantilever beam. The assembly of the sheet metals added to the tip can be seen in Figure 3.23.

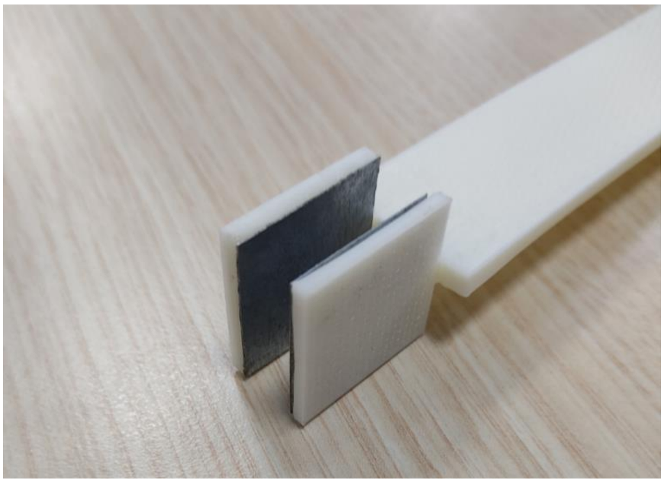

Figure 3.23. Steel sheets assembled on the tip of the 3D printed polymer cantilever beam

For the determination of the thickness of the sheet metal activators, some different thicknesses were used and tested because there was the problem of a small gap between the activators and the sensor. When sheet metal activators with small thickness values such as 0.1 mm were used the magnetic sensor couldn’t detect the movement of the beam precisely, and when the thickness of the activator was bigger such as 1 mm, the sensor had good detection of the displacement however the clearance between the activators and the sensor became small causing contact between the surfaces which interferes with the vibration movement. After testing sheet metal activators of various thickness values, the most suitable thickness was determined. As seen in Figure 3.24, sheet metals of 0.35 mm thickness were glued to the inner faces of the tip of the cantilever beam and this thickness value proved to be the optimum value enabling the sensor to take precise measurements while giving enough clearance between the sensor and the activators so that it does not interrupt with the movement of the beam. The addition of the sheet metal activators creates a point mass of 1.25 grams which is added to the cantilever beam and the mass of these sheet metals was taken into account in both analytical and numerical calculations of the natural frequency values.

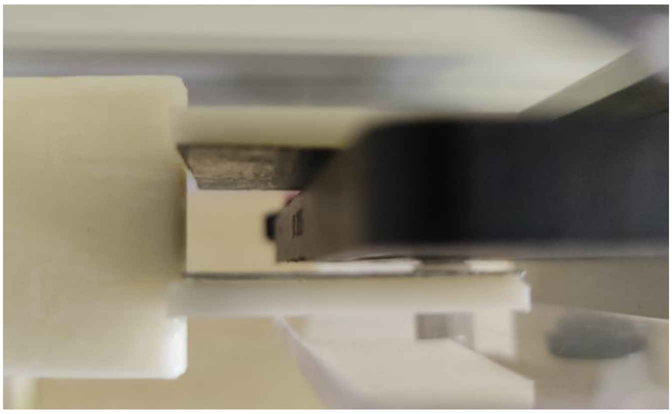

Figure 3.24. Positioning of the sheet metal activators at the tip of the beam

The test equipment has its own data acquisition system and there is a built in software for visually displaying and storing the experimental data called VDAS (Versatile Data Acquisition System). The time-displacement graph is shown live on the screen during the experiment runs. The data captured is recorded in a Microsoft ® Excel file with displacement values in millimeters and time values in seconds. It is important to choose the right sampling frequency when carrying out data acquisition in certain frequencies. According to the Nyquist sampling theorem, the sampling frequency should be at least twice the highest frequency of the vibrating body. This is the minimum limit to convert the analog signal to a digital signal that is the closest to the signal of the real vibrating body. If this is not provided a phenomenon called aliasing occurs causing the signal to have deteriorated. The more the sampling frequency is the more precise the graph of the motion gets however when the sampling frequency is very high the amount of data collected increases tremendously taking up too much memory space in data logger devices. An optimum value of the sampling frequency should be selected for better results. After making some testing, for our experiments, the sampling frequency was chosen to be 125 Hz which gave us accurate graphs of time displacement while enabling us to take enough data to make good calculations of damping. In our case, the highest frequency is the natural frequency of the beam, and generally, our sampling frequency was at least 10 times the natural frequency values which are also conforming to the vibration testing industry practices regarding time domain data acquisition. The software has analog to digital converters and during the conversion, it uses low pass filters to prevent aliasing distortion.

The beams were fixed in one end with four bolts which provided good stabilization of the fixed end. The other end of the beams with activators was placed carefully on the indicated area of the sensor where accurate measurements can be made. The length of the beam can be adjusted according to a scale mounted on the test gear, and the length of the beams was adjusted to 280 mm effective beam length value. This value will be used in numerical and analytical calculations.

To test the free vibration behavior of a cantilever beam, a known initial displacement should be provided and it should be released carefully without any additional force applied. The beam then oscillates freely until the motion stops due to the damping effect. During the movement, the sensor collects data and this data can be used in vibration calculations. For the tests of the cantilever beams in this thesis, an initial displacement of 5 mm value was given on each test. This value was chosen according to the limits of the displacement sensor since the user manual suggests a 5 mm initial displacement value. To make sure the initial displacement of 5 mm was obtained horizontally, a support structure 5 mm shorter than the tip of the beam was mounted on the test desk and the clearance was measured with a 5 mm gauge block. This value could also be seen on the screen of the VDAS software and verified and before every test run the sensor was set to zero with the help of the set zero knobs for calibration. The support structure used for adjusting the initial displacement value can be seen in Figure 3.25.

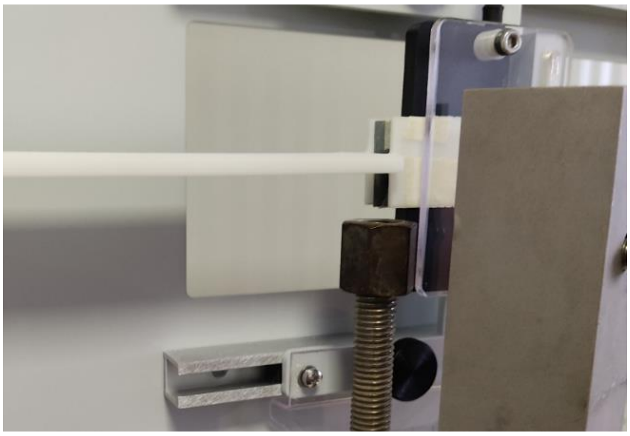

Figure 3.25. Adjustment of the initial displacement value

As can be seen in Figure 3.26 the test starts with the push of a button to initiate recording the data, then an initial displacement of 5 mm is provided on the tip of the beam. The beam is released slowly without exerting any extra force and the beam oscillates freely until the motion has come to a halt due to damping. In the graph, the motion is not finished and this is due to the memory limitations of the data logger however this much data is sufficient to calculate the natural frequency and damping values of the free vibration. As mentioned earlier the optimum value of the sampling frequency was determined to get decent measurements.

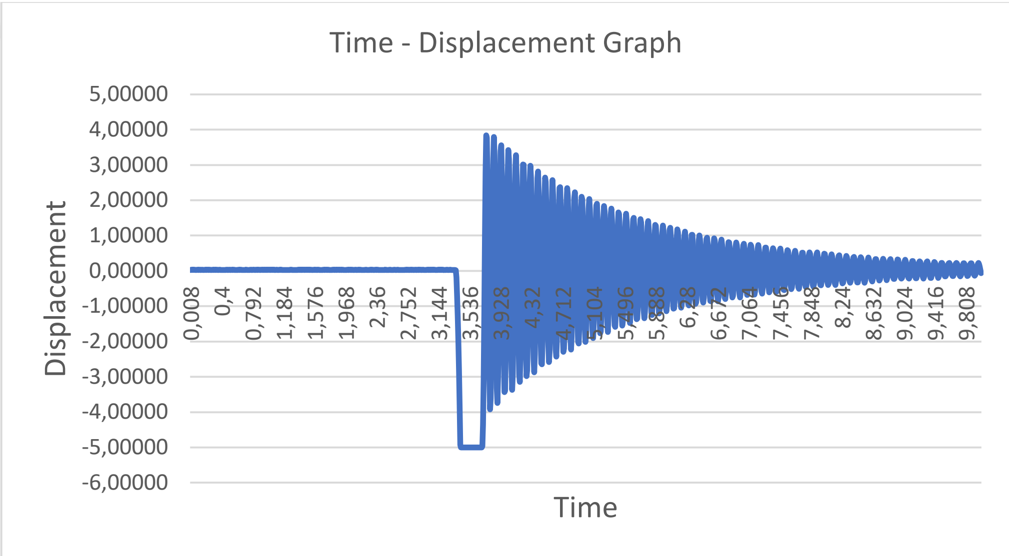

Figure 3.26. Plot of a sample test displaying the 5 mm initial displacement and free vibration

3.4. Experimental Vibration Calculations

Following the 5 mm initial displacement, the beam oscillates until its completely damped, and the test data is stored in file. The file can also be exported to a Microsoft ® Excel file. The Excel data of the displacement time values were exported to a MATLAB ® code written. This code first plots the time - displacement graph of the free vibration of the cantilever beam using the excel data file. To get appropriate results and make the right calculations in MATLAB ®, the excel data file was rearranged. This was done by erasing the first zero displacement data of the file including the 5 mm displacement data until the first positive peak point of the oscillation data. This can be seen in Figure 3.27. A sample time-displacement data plot drawn by the MATLAB ® code can be seen in Figure 3.28.

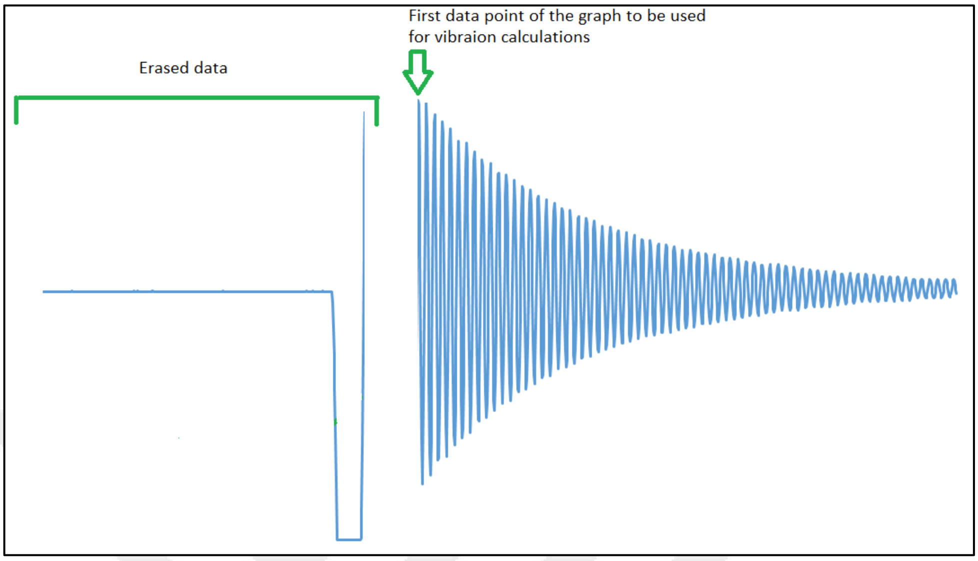

Figure 3.27. Rearrangement of the raw test data file

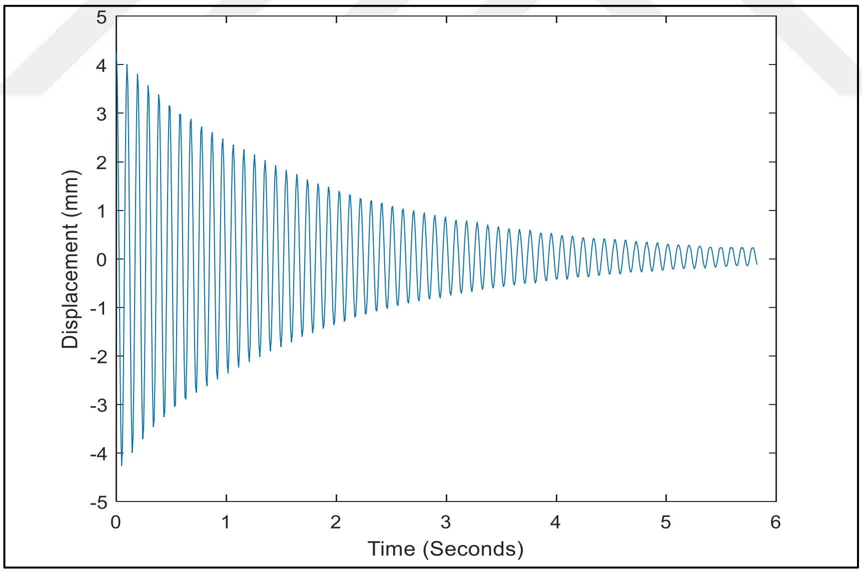

Figure 3.28. Time – displacement plot of a test data processed by MATLAB ®

Then an FFT analysis was performed using the FFT tools of MATLAB. With the use of the FFT analysis the time domain data is converted to the frequency domain and the code plots frequency – amplitude graph of the test data. With this information, the damped natural frequency of the cantilever beam used in the test can be obtained. A frequency domain plot of a prototype test of a pure ABS cantilever beam can be seen in Figure 3.29.

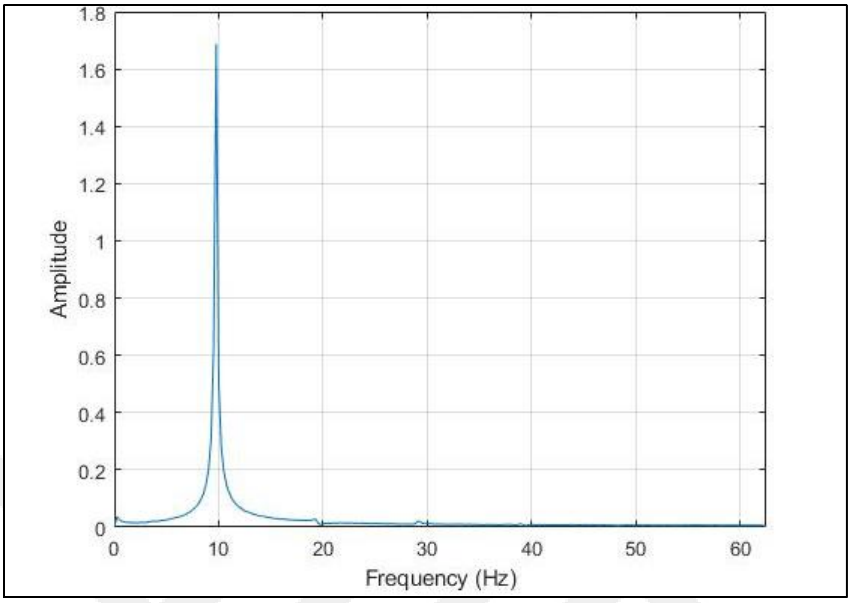

Figure 3.29. Frequency – Amplitude graph of a test file after FFT analysis in MATLAB ®

After the calculation of the damped natural frequency experimentally, the damping ratio should be calculated to calculate the undamped natural frequency value. In general, the damped natural frequency value is assumed to be the same as the undamped natural frequency value in cases where the damping ratio is smaller than 0.2. However, although there is a small difference between the two values, both values were calculated in this thesis.

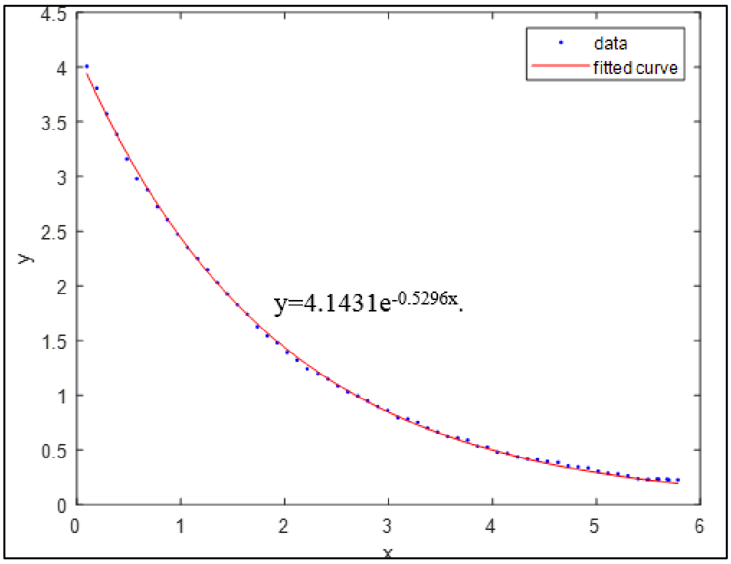

Figure 3.30. Curve fitting method applied to the positive max points of a prototype test plot

As stated in the previous section, two envelope curves are drawn tangent to the time - displacement plot and they touch the peak points of the positive and negative sides of the graph. These curves are in exponential form and the function is formulated as $u = \pm\rho e^{-\zeta\omega_n t}$. Here, ρ is the amplitude, ω_n is the natural frequency and t is time. A curve fitting performed by the MATLAB code and the Equation of the envelope curve can be seen in Figure 3.30. When curve fitting is performed, the constants of the function get calculated and the numerical values of ρ and $-\zeta\omega_n$ are obtained. Since what we get from FFT analysis is the ω_d, we need to express this value in terms of ω_n. The way to do that is by remembering the relationship between these two frequency quantities which is the Equation $\omega_D = \omega_n\sqrt{1-\zeta^2}$. We then can express ω_n in terms of ω_D which is

$$\omega_n = \frac{\omega_D}{\sqrt{1-\zeta^2}} \tag{3.1}$$

Given that we get the envelope curve function $y = -be^{-ax}$ the MATLAB code estimates the function with the given peak points by fitting a curve in the exponential form and gives us the numerical values of b and a. Here b equals the value ρ and a equals the value $\zeta\omega_n$. To solve for ζ we should use (1) and express ω_n in terms of ω_D and write the Equation

$$a = \zeta \frac{\omega_D}{\sqrt{1-\zeta^2}} \tag{3.2}$$

Since a is a numerical value obtained by the experimental curve fitting, Equation (2) can be solved for ζ. When ζ is specified we can also use the relation $\omega_D = \omega_n\sqrt{1-\zeta^2}$ and calculate the natural frequency of the cantilever beam. In the calculations curve fitting was applied to the positive side of the time – displacement plot since the negative side of the envelope curves also provided very close values.

All the natural frequency and damping values of the nano Carbon Black – ABS beams and nano Calcium Carbonate – ABS beams were calculated experimentally using the method explained above in this thesis.

3.5. Numerical Vibration Calculations

3.5.1. Obtaining the material properties for numerical calculations

We can calculate the natural frequency of a cantilever beam by analytical formulas as well. As given in the previous section, the natural frequency of a cantilever beam can be calculated with Equation (2.23). However, we need to know Young's modulus, mass, and moment of inertia values. Since nano composite polymers were fabricated and used in the 3D printing process of the cantilever beams, the young's modulus value of the materials can only be obtained by performing tensile tests. For tensile tests, dogbone specimens were 3D printed with the same nano composite $CaCO_3$ and Carbon black filaments manufactured with the single screw extruder in our laboratory. The test specimens were 3D printed complying with the dimensions according to ASTM D638-14 test standard. The dimensions of the dogbone tensile test specimens can be seen in Figure 3.31.

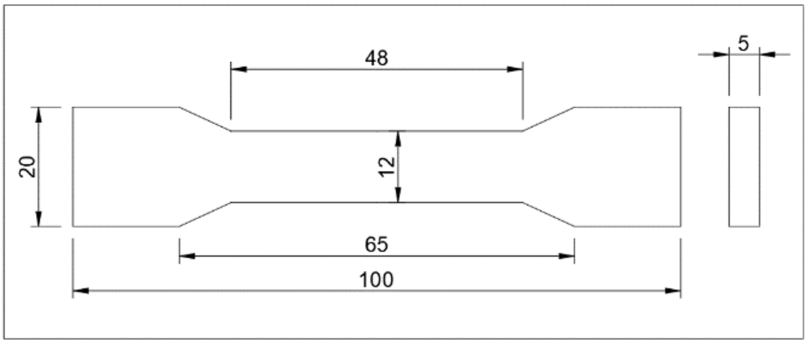

Figure 3.31. Dimension in mm of the dogbone test specimens with nano $CaCO_3$ particles

The test specimens were 3D printed with the same printing parameters (layer thickness, extrusion temperature, infill geometry, etc…) used in the production of the cantilever beams. A 3D printed tensile test specimen of Carbon Black material can be seen in Figure 3.32. Tensile tests were carried out at room temperature with a Shimadzu AGS-X 100 kN tensile testing machine with a constant 1 mm/min loading rate

Figure 3.32. A 3D printed ABS+1wt% nano carbon black –tensile test specimen

The test setup for that was used for tensile testing can be seen in Figure 3.33.

Figure 3.33. Shimadzu AGS-X tensile testing machine used for the tensile tests

3.5.2. Numerical calculations with ANSYS

Obtaining the Elastic modulus from the tensile tests, the numerical analysis of the cantilever beam model can be made with the help of the ANSYS modal analysis tool which is used for vibration analysis. A modal analysis system was created by dragging and dropping from the toolbox menu of the ANSYS workbench as seen in Figure 3.34.

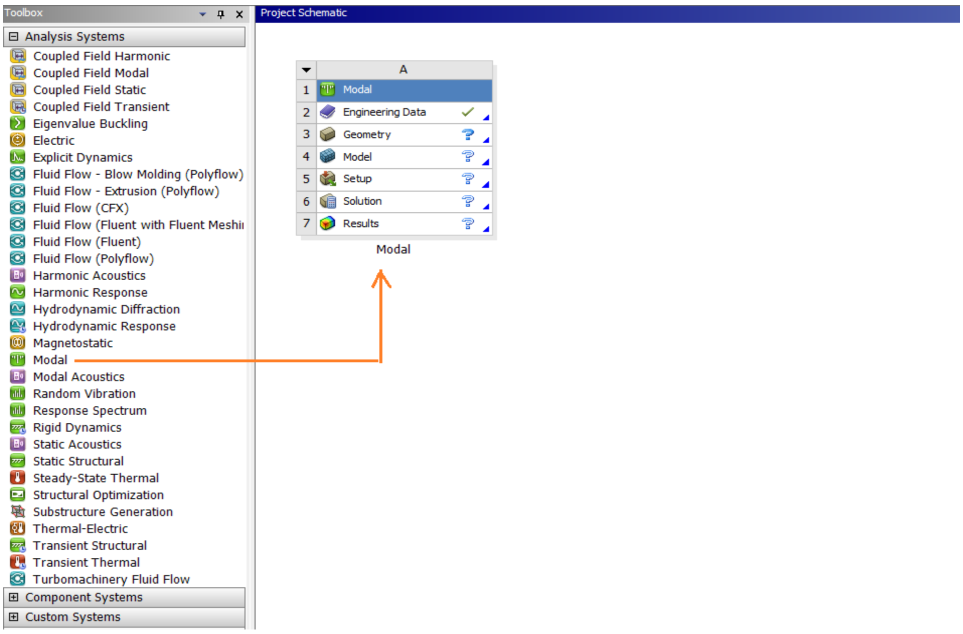

Figure 3.34. Creation of a modal system for vibration analysis

After the creation of the modal system, Engineering Data was selected to create a new material. Then create a new material was clicked on the line below the default structural steel material as seen in Figure 3.35.

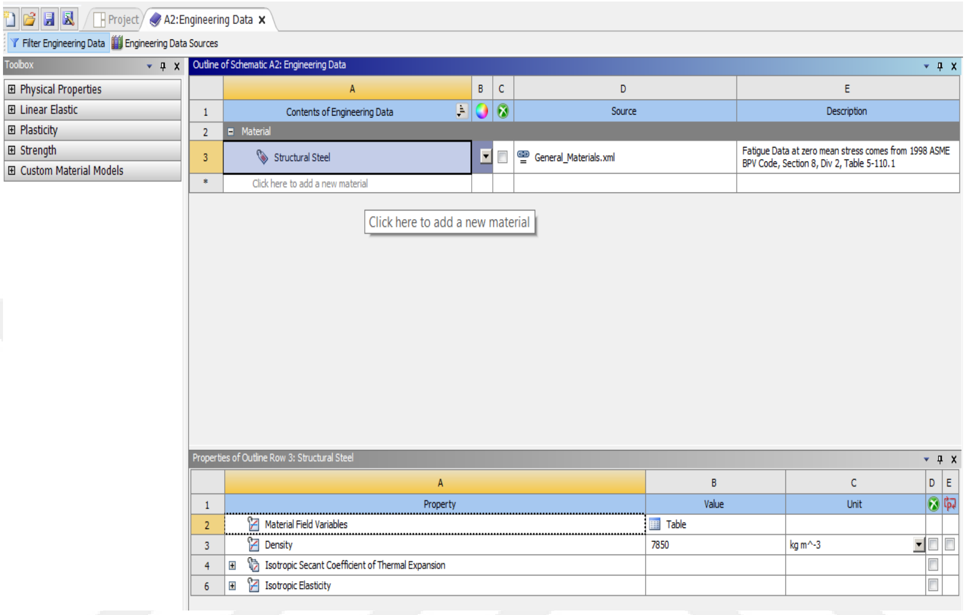

Figure 3.35. Creation of new material in the Engineering Data section

As seen in Figure 3.36 a new material was created with the name Pure ABS. specified in the engineering data section as well.

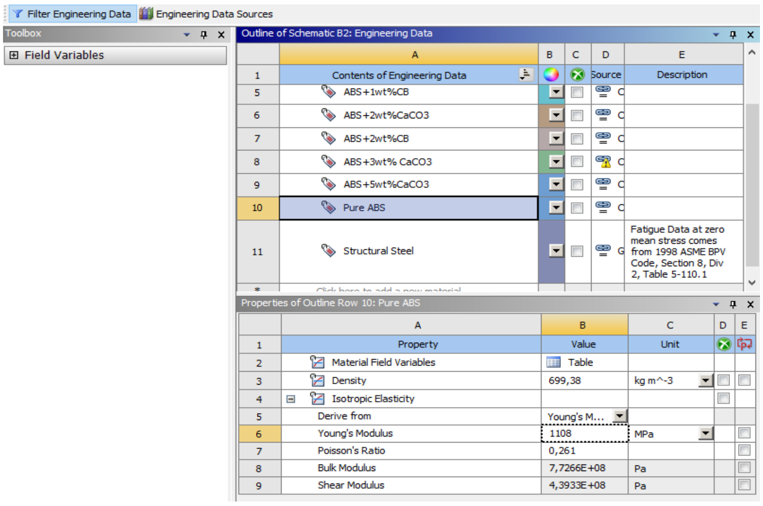

Figure 3.36. Pure ABS cantilever beam properties

This material is the in-house manufactured ABS using the pellets of ABS produced in a single screw filament extruder. The tensile test specimens were 3D printed with this filament and the engineering constants calculated by the tensile test results will be used for precise numerical analysis. For all the different nanoparticle ratios of the cantilever beams of CB and $CaCO_3$, new materials were created in ANSYS for their modal analysis. The properties of the beams were considered as isotropic material although these beams exhibit orthotropic behavior due to their production method which is AM. However, in the case of the thesis, the vibration of the cantilever beams is tested in mode 1 due to the limitations of the test setup. The sensor near the tip of the beam detects the vertical displacement of the beam tip and with this data, the mode 1 vibration of the cantilever beam can be detected. In calculations of the mode 1 vibration, as can be seen in Equation (2.23), the elastic modulus of the material in the tensile test direction is required for the analysis. Poisson's ratio was also calculated from the tensile tests and it was The densities of the beams were calculated by weighing them on a precision scale (Figure 3.37) and dividing the mass by the volume.

Figure 3.37. Weighing of the 3D printed beams

All beams produced were weighed on a precision scale and their densities were calculated since the volume of the beams is known. For every beam, Young's modulus and Poisson's ratio values were calculated according to the tensile tests. All the data were entered in the engineering data section of ANSYS and a new material for every beam was specified and assigned to the beam for every numerical calculation as seen in Figure 3.38.

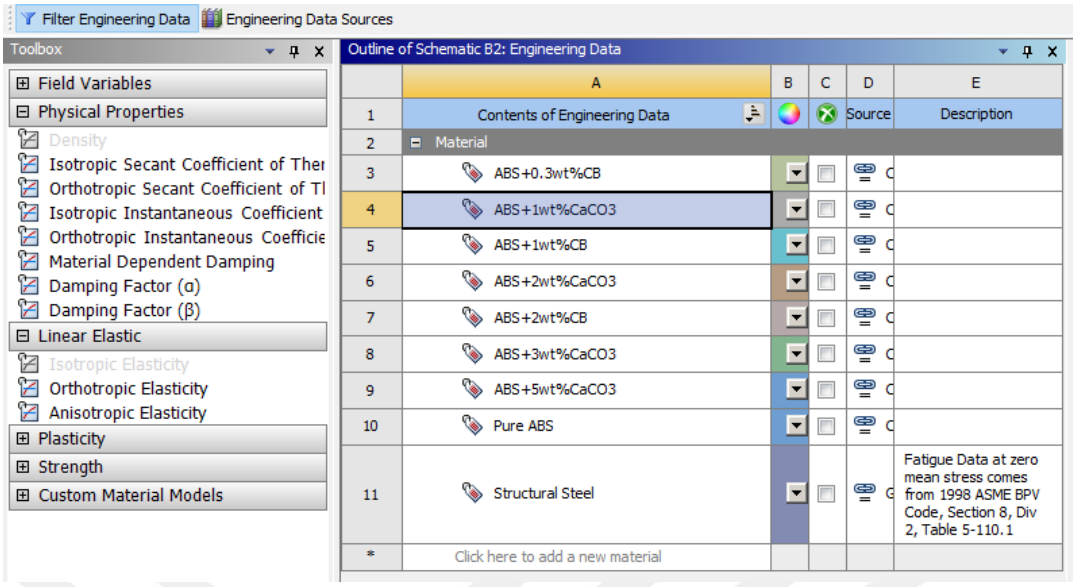

Figure 3.38. All nanocomposite materials specified in the Engineering Data section of ANSYS

The next step was to share the geometry of the cantilever beam file which was created with ANSYS design modeler as well. The file is dragged and dropped to the workbench space and the geometry was shared with the modal system as seen in Figure 3.39.

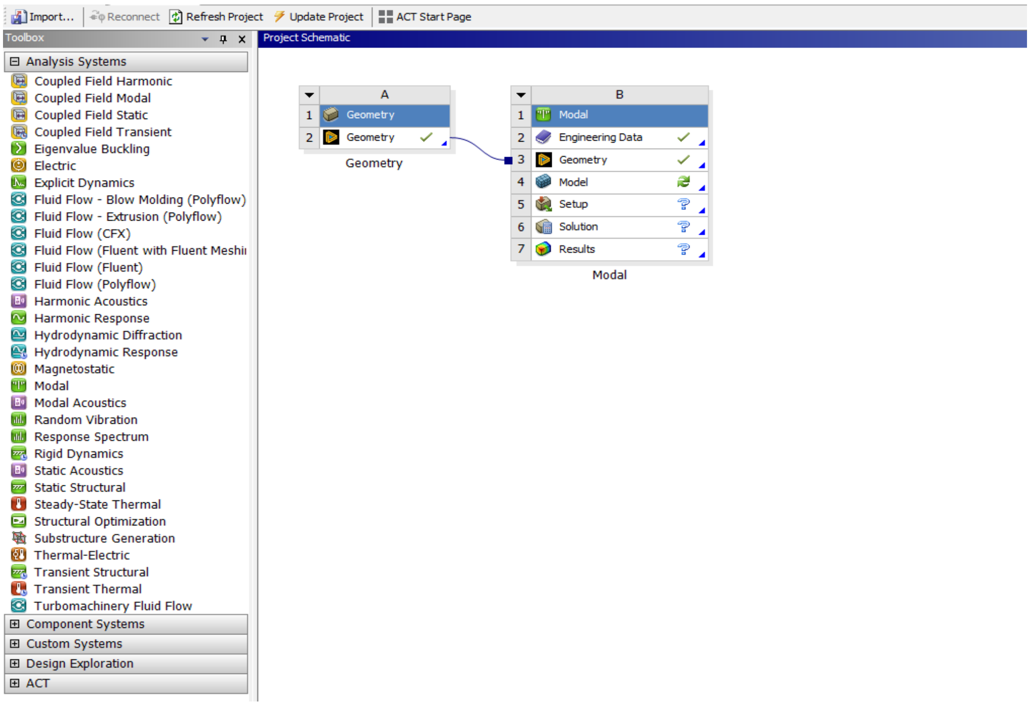

Figure 3.39. Sharing the geometry with the modal system

Once the geometry was shared with the modal system, the modal analysis settings and adjustments were to be made. The modal tool was opened by double clicking and the screen which can be seen in Figure 3.40. The three-dimensional model can be seen as the geometry of the system to be analyzed. As stated in the previous subsections, galvanized steel sheets were assembled to the inner vertical faces of the tip of the beam to be used as activators. The mass of these sheet metals affects the natural frequency value since they are very close to the tip and they have an influence on the deflection value of the tip. Therefore, to make an accurate numerical analysis, the mass of these activators was considered in the analysis. The mass of the sheet metals was assigned as point masses on the surfaces they were assembled. The actual sheet metals were weighed with a digital precision scale and the mass values were 1.5 grams each.

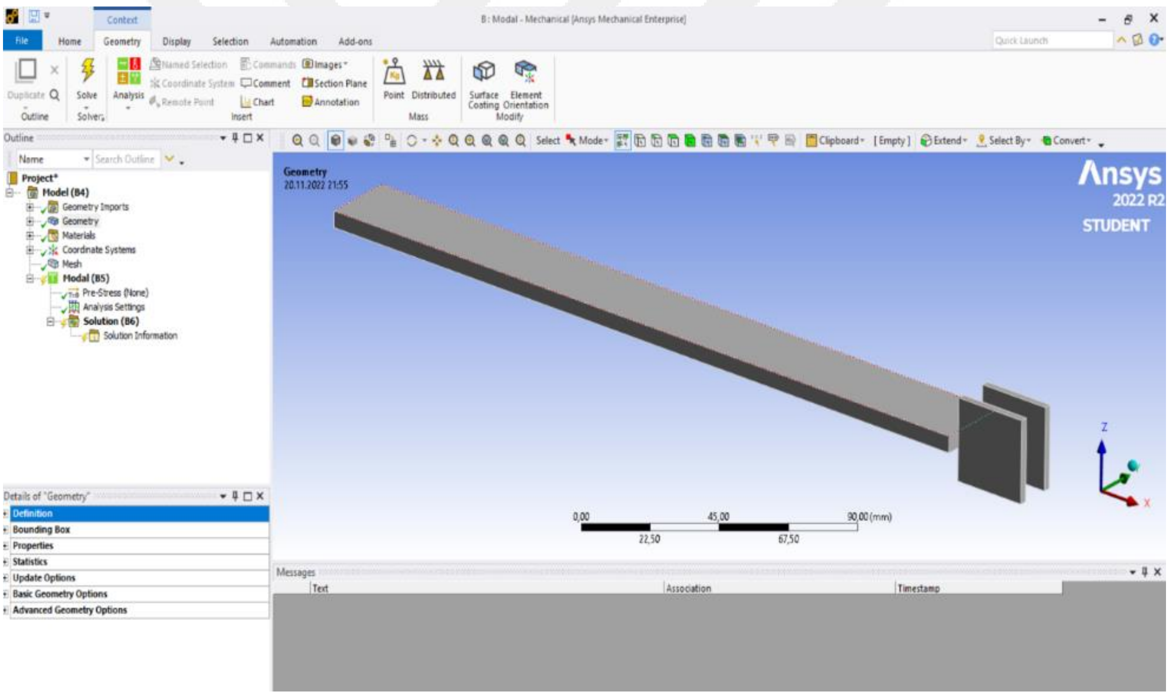

Figure 3.40. Modal analysis window with the shared cantilever beam geometry

This was done by right-clicking Geometry and from the appeared window the mouse was hovered on insert and from another list that pops up, distributed mass was left-clicked. Following that the surface should be selected for the distributed mass to be applied. The inner surfaces of the tip of the cantilever beam was selected and distributed mass was applied.

Figure 3.41 and 3.42 shows the location and mass properties of the two-point masses created on the geometry representing the activators.

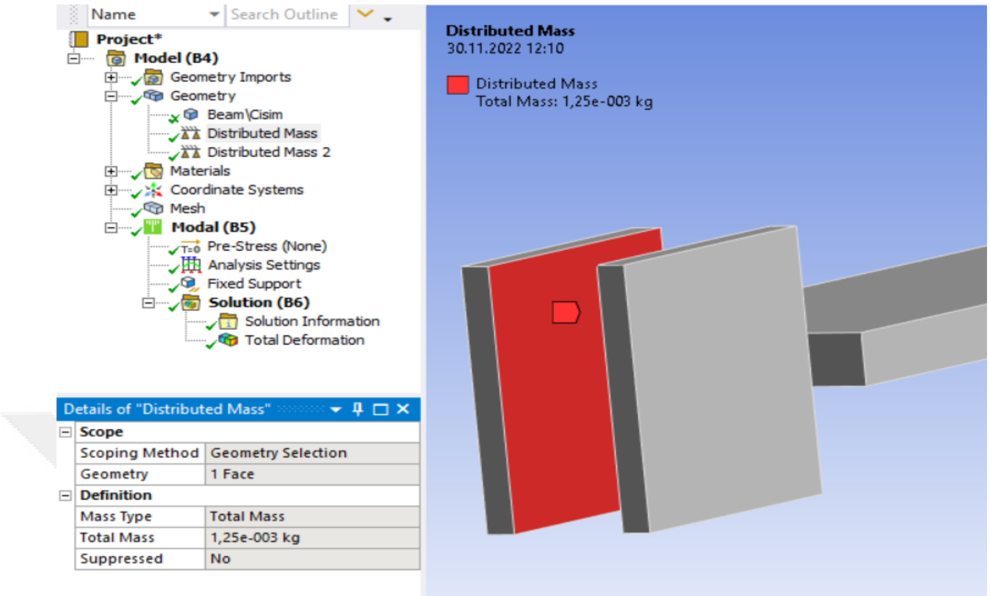

Figure 3.41. Location and mass value in kg of distributed mass 1

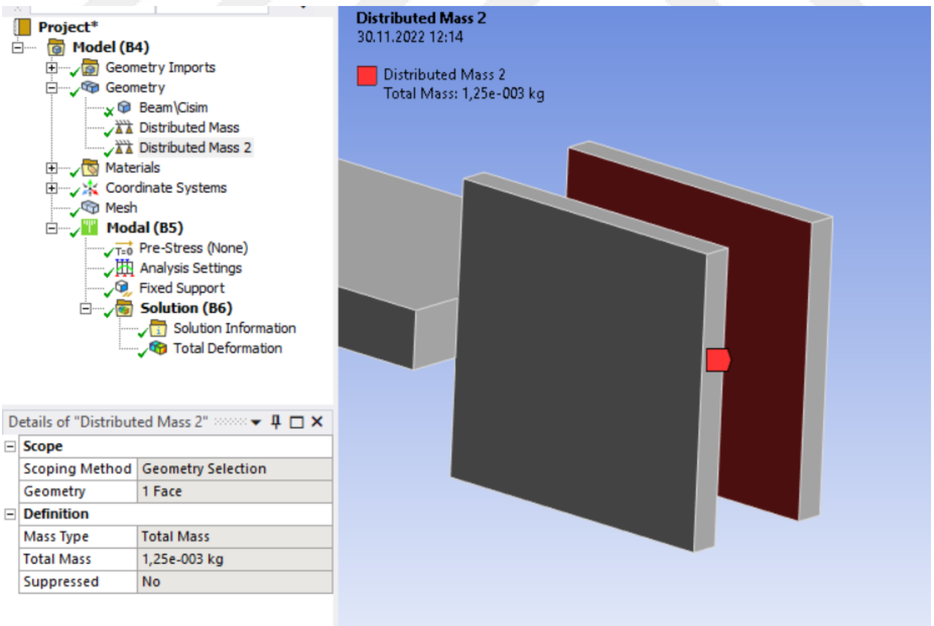

Figure 3.42. Location and mass value in kg of distributed mass 2

One of the important aspects of numerical analysis is the meshing procedure. As commonly known, the quality of the meshing performed on a geometry substantially affects the accuracy of the analysis results. There are a lot of criteria regarding the quality of the mesh, however, since the beam geometry is not so complex, not all the detailed criteria of mesh quality will not be discussed here. Nevertheless, some aspects of mesh quality will be covered just enough to obtain a decent quality of the mesh generated for the beam.

There are many mesh metrics to be emphasized however it is crucial to explain one of the most important aspects of mesh metrics which is element quality. Element quality is the mesh metric where the quality of every single mesh element is rated as a number between zero to one. If the quality of a mesh element is rated as 1, it is the most ideal mesh element in the geometry. If a mesh element is rated as 0, it is the worst possible mesh element in the geometry. In the quality part of the mesh window, element quality can be viewed for a completed mesh and the minimum, maximum, and average values of the mesh quality are given. Generally, the minimum value of the element quality is expected to be higher than 0.2 and values lower than that are considered unacceptable. The average value of the element quality is expected to be high as possible.

When a mesh is generated without any arrangements and settings made, ANSYS creates a default mesh suitable for the geometry. When we generate a mesh as default, the mesh structure can be seen in Figure 3.43. The minimum value of element quality is 0.11702, the maximum value is 0.8615 and the average value is 0.2699. These values can be expressed as very poor and some adjustments have to be made to improve the element quality.

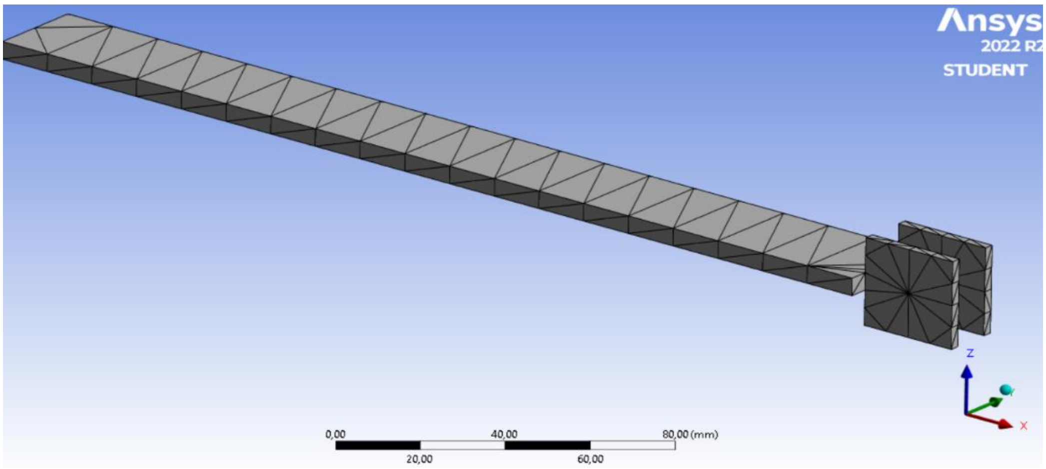

Figure 3.43. Default mesh generated by ANSYS

Another aspect of mesh quality is the number of nodes and elements. As the number of nodes and elements increases the precision of the analysis increases. These values can be viewed in the statistics window of the mesh section. The number of nodes for the mesh was 712 and the number of elements was 242. The element quality metrics for the default mesh can be seen in Figure 3.44. Additionally, the distribution of the elements according to their quality can be seen in Figure 3.45 for the default mesh as well.

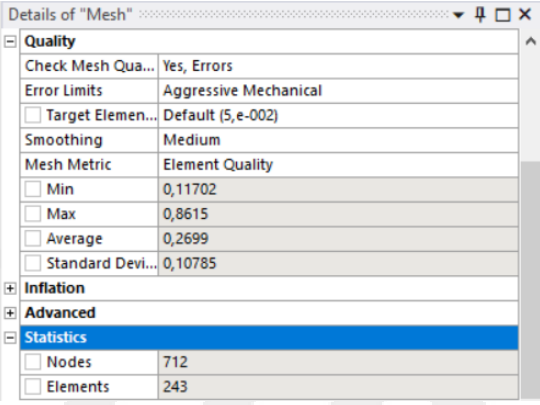

Figure 3.44. Element quality metrics of the default mesh and the number of nodes and elements

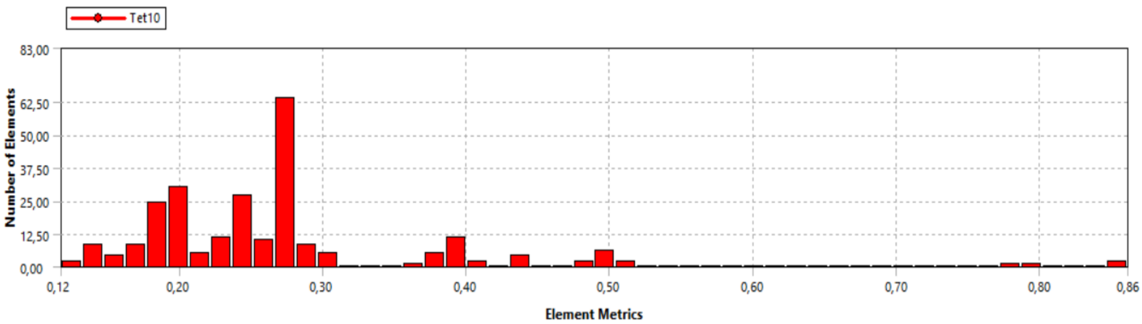

Figure 3.45. Distribution of the number of elements according to their element quality values

To increase mesh quality, under details of mesh window, sizing was clicked. By default, use adaptive sizing section has a yes value and this value was chosen as no. When this is done some more options appear. The capture proximity value was no as default and this value was altered to yes. Following that, the proximity gap factor value was 3, which was the default value, this was changed to 2. Since ANSYS student was used in the analyses, there is a limit to the number of elements to be included in the mesh for solving. The maximum number of elements allowed for solving structural problems is 32000. The number of elements was adjusted to a number just below this limit and the element quality values were increased substantially reaching a significant improvement from the default mesh of ANSYS. The appearance of the improved mesh can be seen in Figure 3.46.

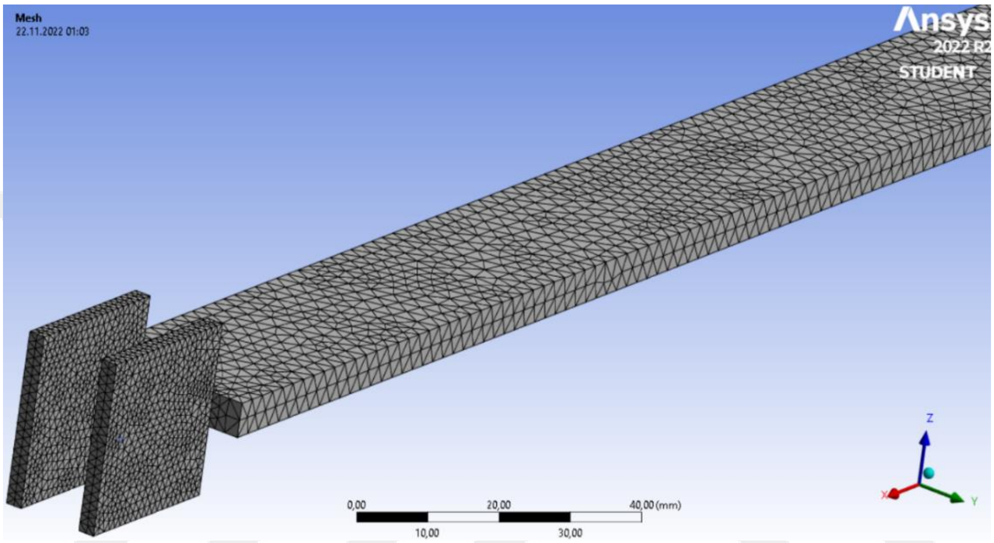

Figure 3.46. Mesh generated after making the arrangements

The metrics regarding element quality for the improved mesh can be seen in Figure 3.47. The distribution of the number of elements according to their element quality values for the improved mesh as well can be seen in Figure 3.48.

Details of "Mesh"	
Check Mesh Quality	Yes, Errors
Error Limits	Standard Mechanical
Target Element Quality	Default (5,e-002)
Smoothing	Medium
Mesh Metric	Element Quality
Min	0,27628
Max	0,99806
Average	0,81179
Standard Deviation	9,7704e-002
+ Inflation	
+ Advanced	
− Statistics	
Nodes	51834
Elements	31679

Figure 3.47. Element quality metrics of the custom mesh and the number of nodes and elements

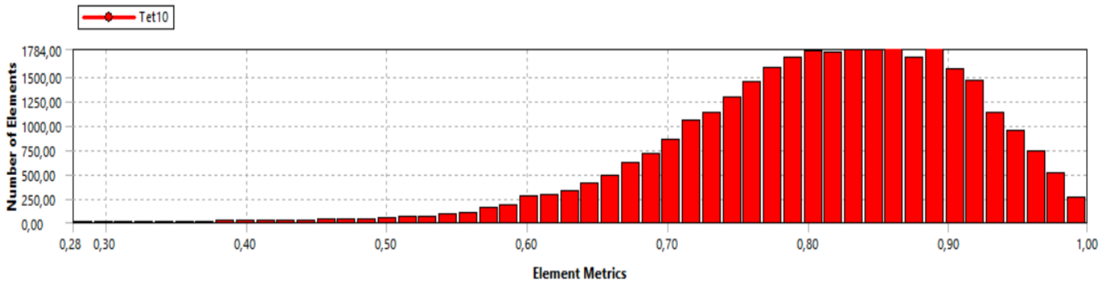

Figure 3.48. Distribution of the number of elements according to their element quality values

After completing the meshing, the fixed end of the cantilever beam was specified in the analysis since this geometry is a cantilever beam. This can be done by right-clicking on modal in the opened menu clicking insert and in the further menu clicking add fixed support as seen in Figure 3.49.

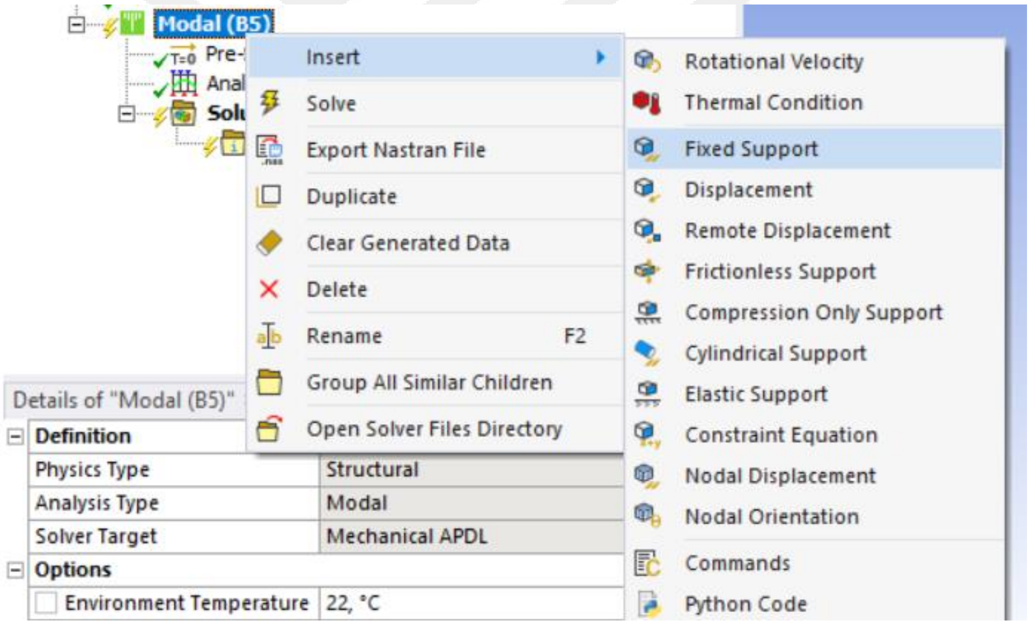

Figure 3.49. Fixed-end specification of the cantilever beam

Following the add fixed support command a surface was selected on the beam for the selection process of the boundary condition. The selected face can be seen in Figure 3.50.

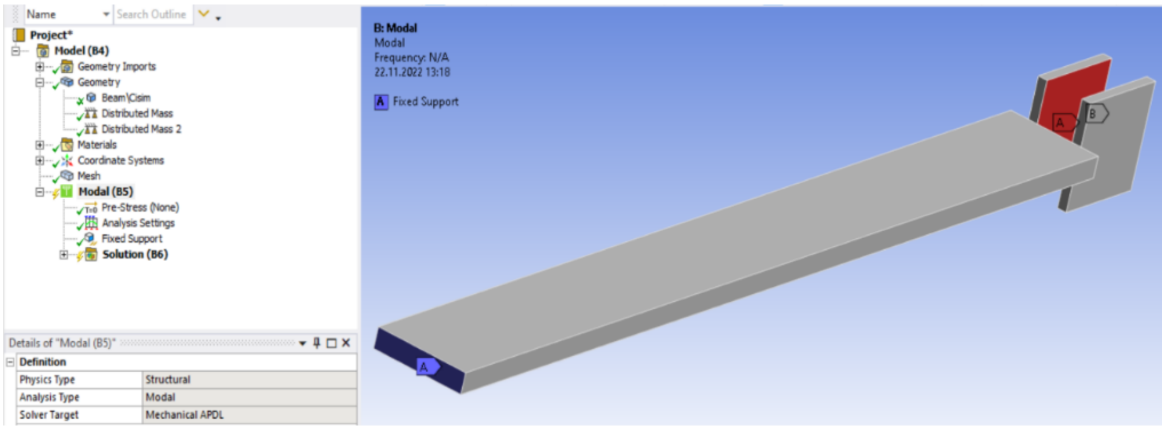

Figure 3.50. Fixed end selection of the cantilever beam for setting the boundary condition

After completing the preparations for the analysis, the solving process was started by right-clicking the solution and on the opened window clicking solve. With some processing of the computer, the results were displayed on the screen. Natural frequency values of the first six modes were given as tabular data and also these were given as a graph as well. As stated earlier, only mode 1 values will be considered in the numerical analysis since the experimental values were mode 1 calculations as well, due to the capabilities of the test gear. The results for the pure ABS cantilever beam can be seen in Figure 3.51 as tabular data.

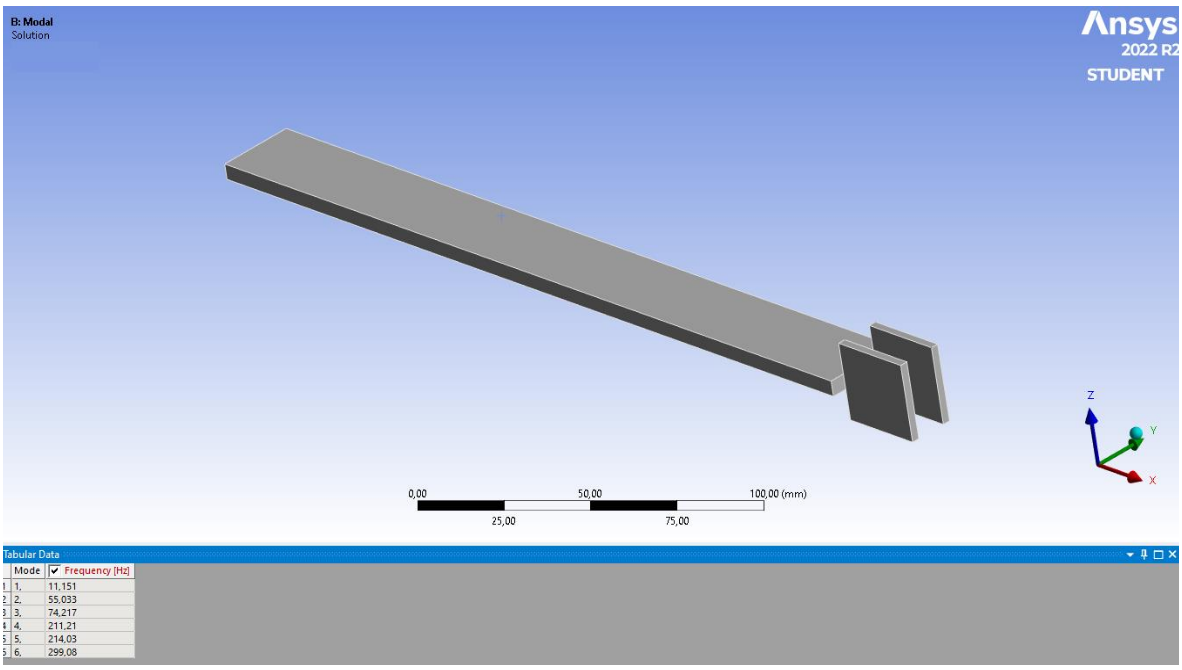

Figure 3.51. Pure ABS modal analysis results

A total deformation solution was also added to the solution section to see the behavior and deflections of the mode shapes. The oscillation can also be viewed as an animation if desired to better observe the movement of the beam according to the mode shapes. To do that, the solution section was right-clicked and the insert was pointed and total deformation was selected as seen in Figure 3.52

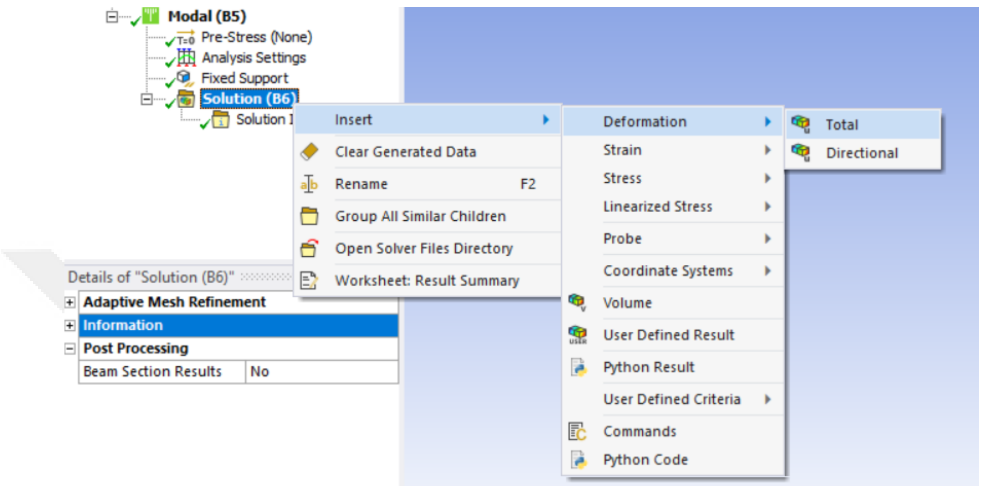

Figure 3.52. Adding a total deformation element to the solution

A solution for a total deformation calculation can be seen in Figure 3.53.

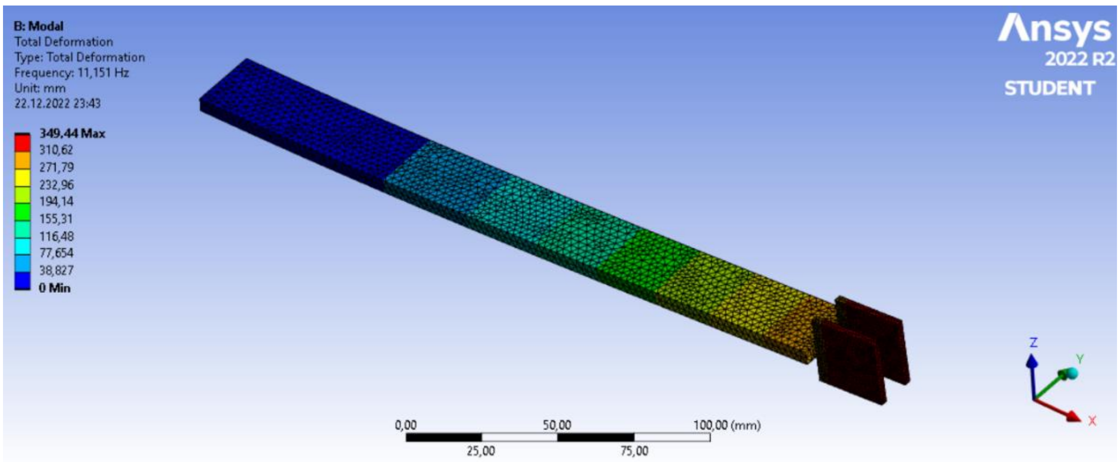

Figure 3.53. Total deformation results in mode 1 of the beam modal analysis

An initial comparison of the experimental results and numerical results were made and it was seen that there were errors greater than expected. Error to some extent is naturally inherent in such a procedure which will have the cumulative effects of vibration testing errors, dimensional differences from the 3D printing process of the specimens which may be caused also by the use of ABS itself and of course assumption made that the material is isotropic for the simplicity of the numerical calculations. However, the addition of the nanoparticles may have caused more deviations of the geometry causing changes in natural frequency calculation values causing the error to be larger. After reconsideration of the method applied and the examination of the 3D printed cantilever beam specimens, the dimensions of the specimens were measured in detail and average dimensions were calculated. The new dimensions of every specimen was modeled in ANSYS spaceclaim and numerical calculations were re-run. The density of the specimens was also recalculated and used in these numerical calculations. All calculations and error values were given in a table in the results and discussions section.

3.6. Scanning Electron Microscope Analysis of the Tensile Test Specimens

For the monitoring of the distribution of the $CaCO_3$ and CB nanoparticles in the ABS matrix, and the observation of the morphology of the fractured surfaces of the 3D printed tensile test specimens, the surfaces were investigated with a scanning electron microscope (SEM). Samples of proper dimensions were taken from the fractured tensile test specimens and they were sputter-coated with gold. FEI Quanta 650 field-emission microscope was used for taking the SEM micrographs of the coated surfaces with an acceleration voltage value of 20kV. This process was carried out at Çukurova University Central Laboratory Facility. SEM results will be discussed in the next chapter. A uniform distribution of the $CaCO_3$ particles were observed and some agglomerations of $CaCO_3$ nanoparticles were detected in specimens having

Figure 3.54. FEI Quanta 650 field-emission microscope

more than 2wt% $CaCO_3$ content. As per CB nanocomposites a uniform distribution of CB particles were observed and agglomerations of CB particles increased for specimens containing more than 0.3wt% CB nanoparticles.

4. RESULTS AND DISCUSSIONS

4.1. Experimental and Numerical Results for Beams of ABS + $CaCO_3$ Nanoparticles

4.1.1. Experimental Vibration Test Results for beams of ABS + $CaCO_3$ nanoparticles

Beams of pure ABS and nanoparticles of $CaCO_3$ added in various weight fractions were tested and time – displacement data were logged via the VDAS software and the data was exported to an Excel file. The file was read by the Matlab code and the time – displacement graphs, FFT graphs, and curve-fitting graphs of the tests were plotted. The results for beams with pure ABS and $CaCo_3$ nanoparticles were given with time – displacement graphs, curve-fitting graphs and FFT graphs for every specimen with pure ABS along with various contents of $CaCO_3$ nanoparticles.

Time - displacement and curve fitting graphs of a pure ABS specimen are seen in Figure 4.1.

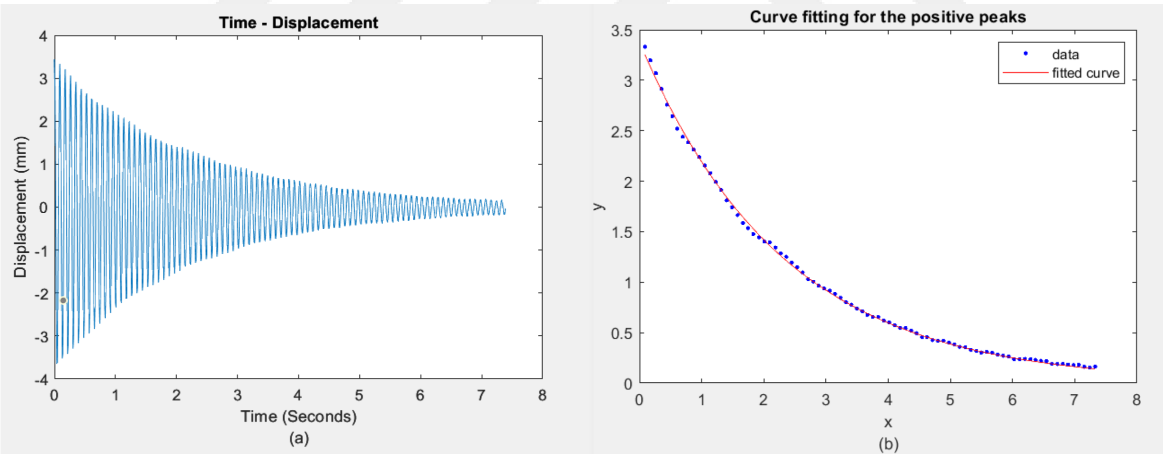

Figure 4.1. Graphs of a pure ABS beam: (a) Time history, (b) Curve fitting.

The FFT graph of a pure ABS specimen can be seen in Figure 4.2.

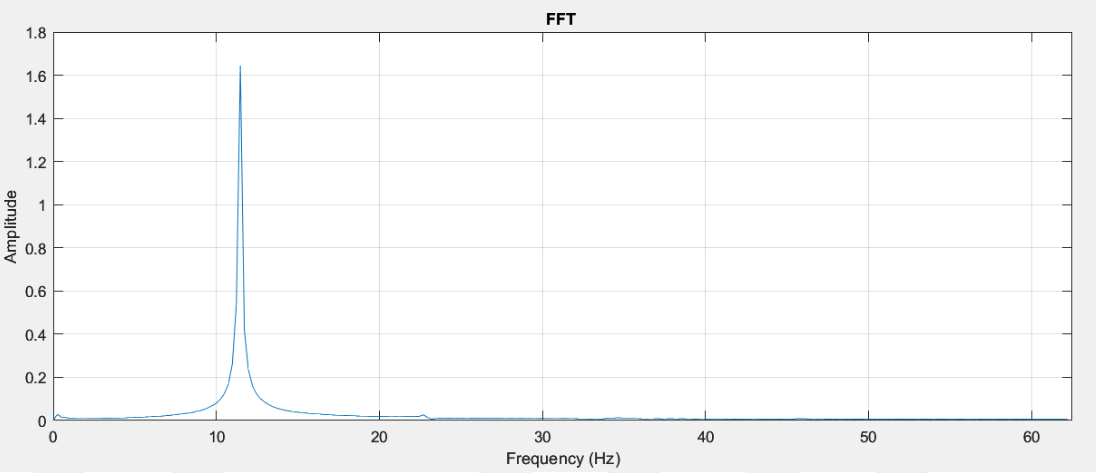

Figure 4.2. FFT analysis graph of pure ABS beam

Time - displacement and curve fitting graphs of an ABS and 1wt% $CaCO_3$ specimen are seen in Figure 4.3.

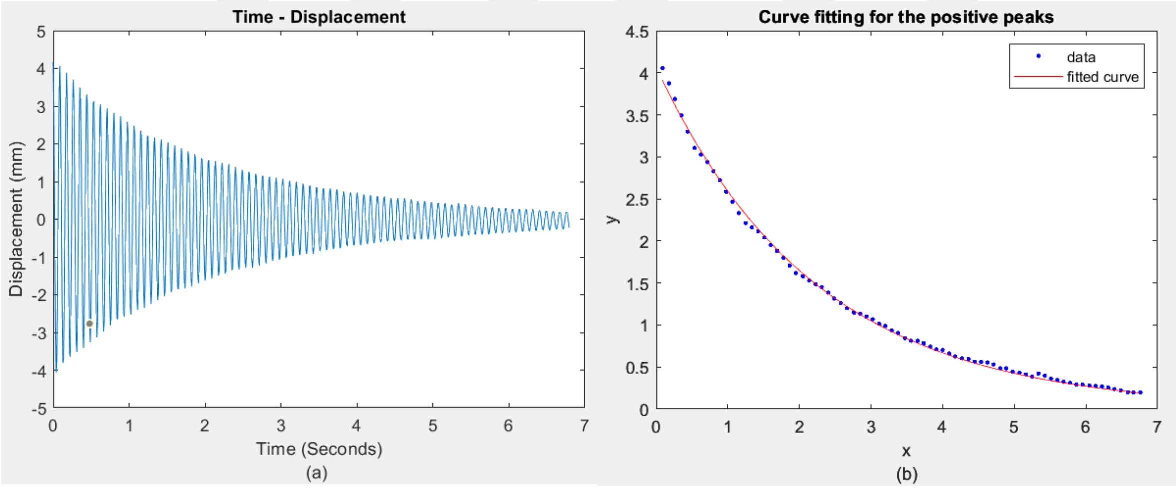

Figure 4.3. Graphs of an ABS+1wt% $CaCO_3$ beam: (a) Time history, (b) Curve fitting

The FFT graph of an ABS and 1wt% $CaCO_3$ specimen can be seen in Figure 4.4.

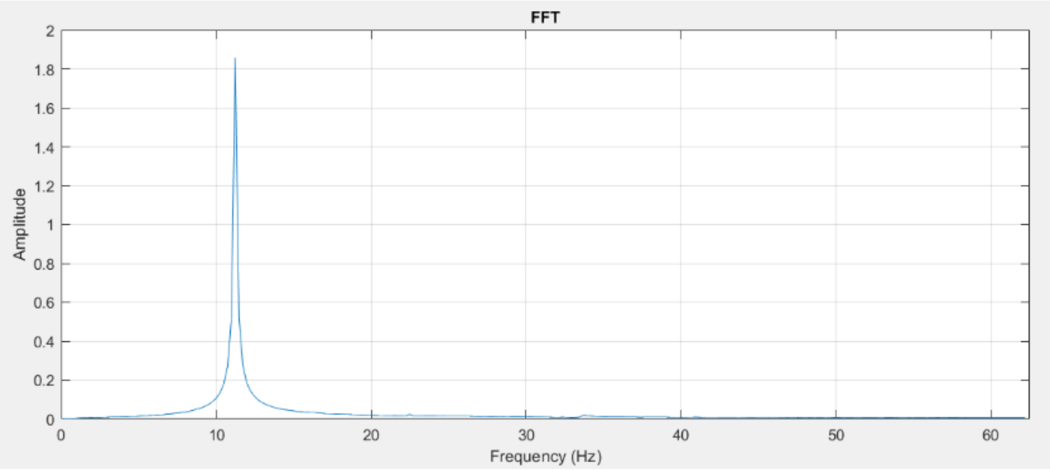

Figure 4.4. FFT analysis graph of ABS and 1wt% $CaCO_3$ beam

Time - displacement and curve fitting graphs of an ABS and 2wt% $CaCO_3$ specimen are seen in Figure 4.5.

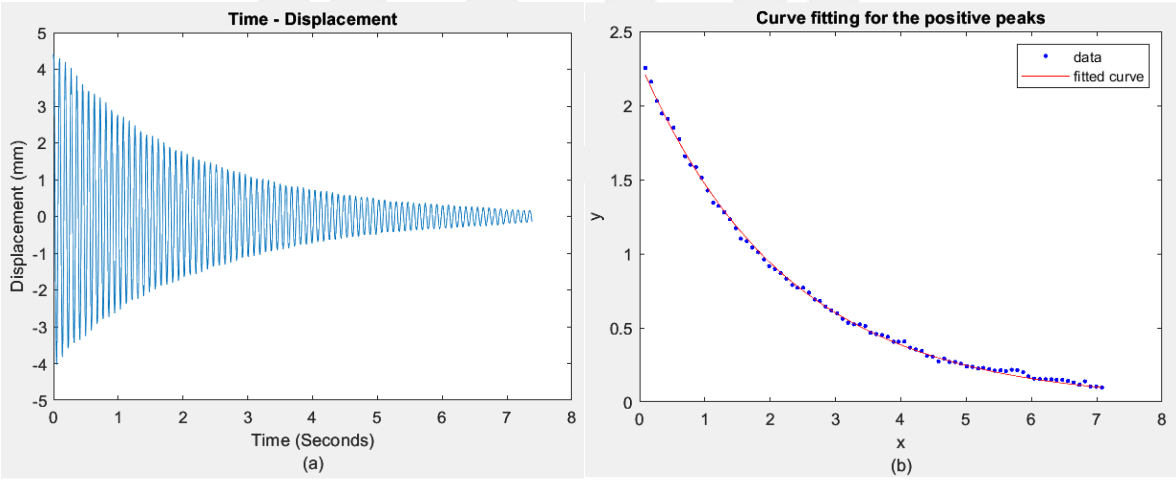

Figure 4.5. **G**raphs of an ABS and 2wt% $CaCO_3$ beam: (a) Time history, (b) Curve fitting

The FFT graph of an ABS and 2wt% $CaCO_3$ specimen can be seen in Figure 4.6.

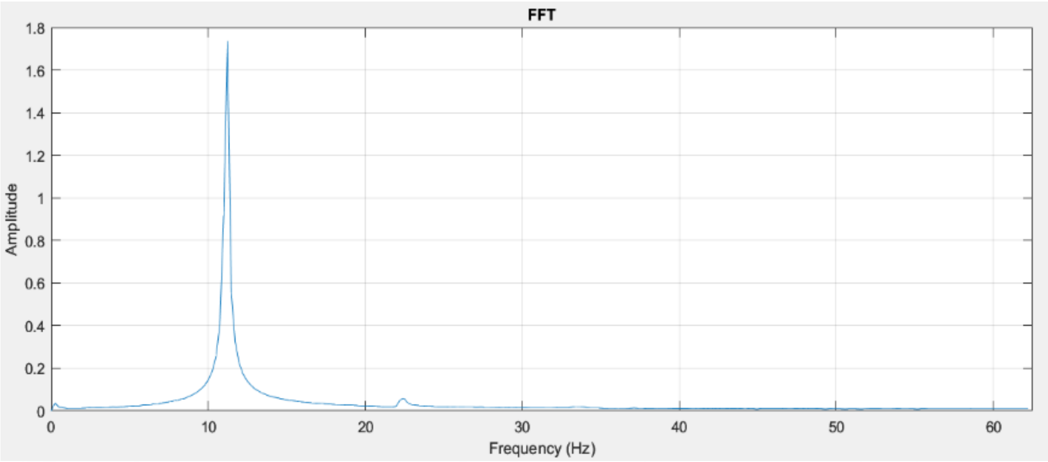

Figure 4.6. FFT analysis graph of an ABS and 2wt% $CaCO_3$ beam

Time - displacement and curve fitting graphs of an ABS and 3wt% $CaCO_3$ specimen are seen in Figure 4.7.

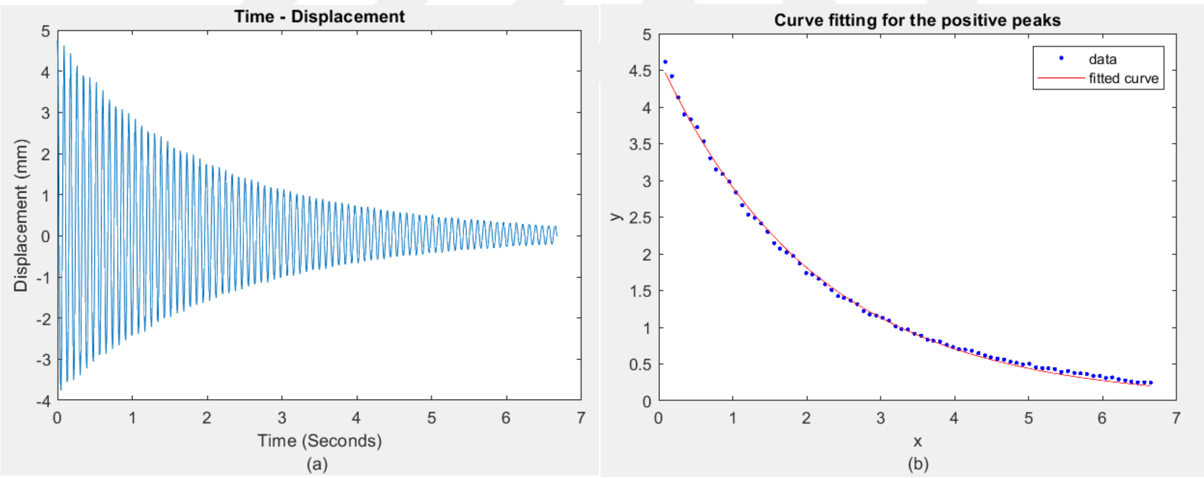

Figure 4.7. Graphs of ABS and 3wt% $CaCO_3$ beam: (a) Time history, (b) Curve fitting

The FFT graph of an ABS and 3wt% $CaCO_3$ specimen can be seen in Figure 4.8.

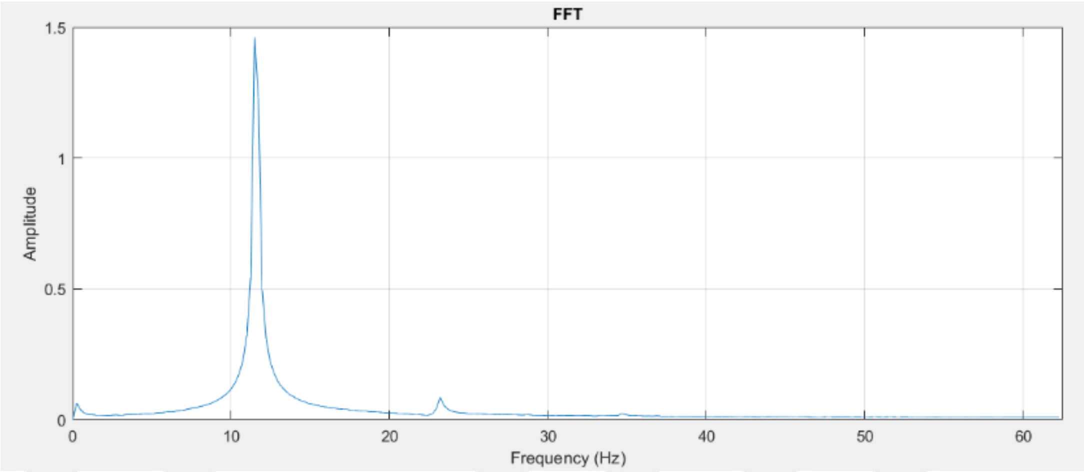

Figure 4.8. FFT analysis graph of ABS and 3wt% $CaCO_3$ beam

Time - displacement and curve fitting graphs of an ABS and 5wt% $CaCO_3$ specimen are seen in Figure 4.9.

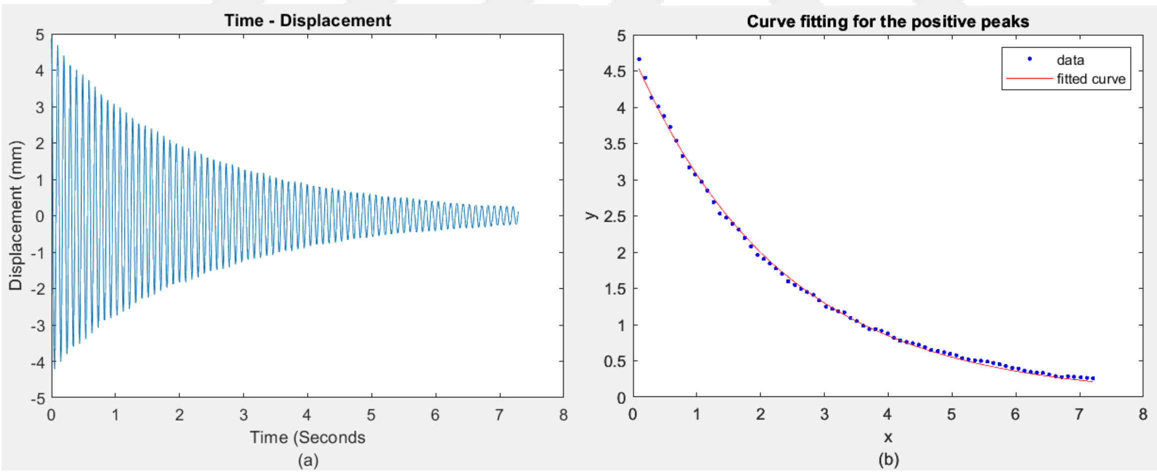

Figure 4.9. Graphs of ABS and 5wt% $CaCO_3$ beam: (a) Time history, (b) Curve fitting

The FFT graph of an ABS and 5wt% $CaCO_3$ specimen can be seen in Figure 4.10.

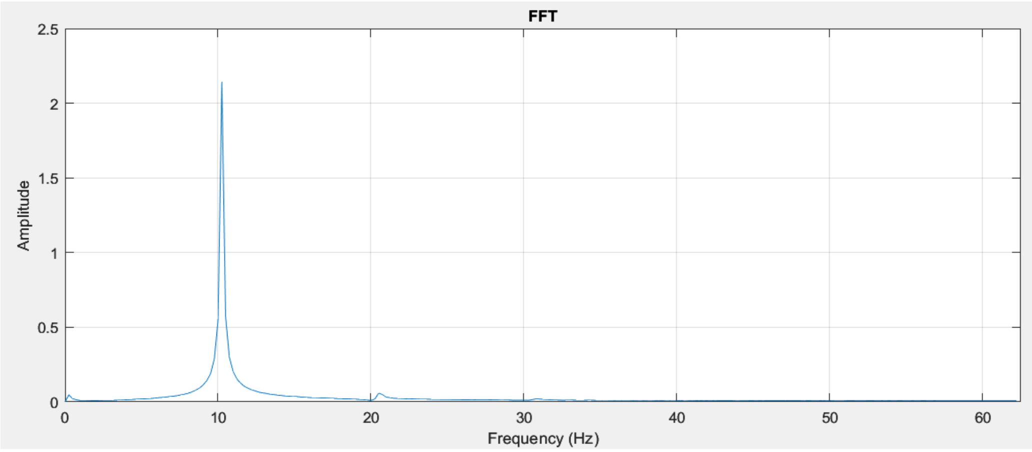

Figure 4.10. FFT analysis graph of ABS and 5wt% $CaCO_3$ beam

As stated in the previous section, the frequency calculated in the FFT analysis gives us the damped natural frequency ω_D and since we have calculated the damping ratio ζ the natural frequency value can be calculated with Equation (3.1). When the natural frequency values are calculated, all the experimental test results were obtained and the results can be seen in Table 4.1.

Table 4.1. Experimental test results for ABS+ $CaCO_3$ nanocomposite beams

	Damped Natural Frequency (Hz)	**Natural Frequency** (Hz)	**Damping Ratio**
Pure ABS	11.4746	11.4748	0.0063
ABS + 1wt% $CaCO_3$	11.2305	11.2307	0.0067
ABS + 2wt% $CaCO_3$	11.2305	11.2307	0.0068
ABS + 3wt% $CaCO_3$	11.4746	11.4749	0.0069
ABS + 5wt% $CaCO_3$	10.2539	10.2542	0.0070

4.1.2. Tensile Test Results for specimens of ABS + $CaCO_3$ nanoparticles

The tensile tests of ABS beams with $CaCO_3$ nanoparticles were carried out as discussed in the previous section and the tensile test graphs and results were obtained. Tensile test graph of pure ABS can be seen in Figure 4.11.

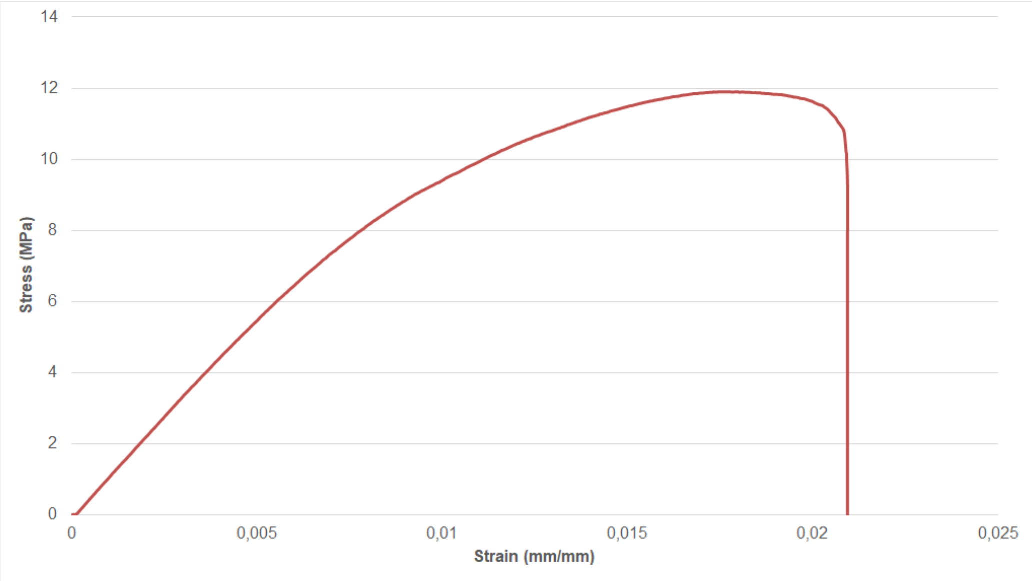

Figure 4.11. Stress – Strain graph of pure ABS specimen

Tensile test graph of ABS + 1wt% $CaCO_3$ specimen can be seen in Figure 4.12.

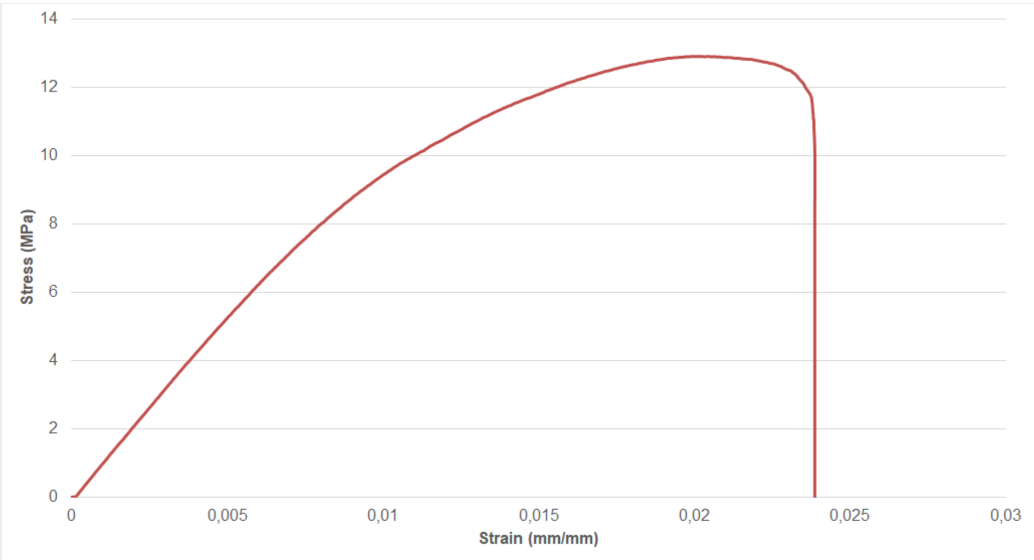

Figure 4.12. Stress – Strain graph of ABS + 1wt% $CaCO_3$ specimen

Tensile test graph of ABS + 2wt% $CaCO_3$ specimen can be seen in Figure 4.13.

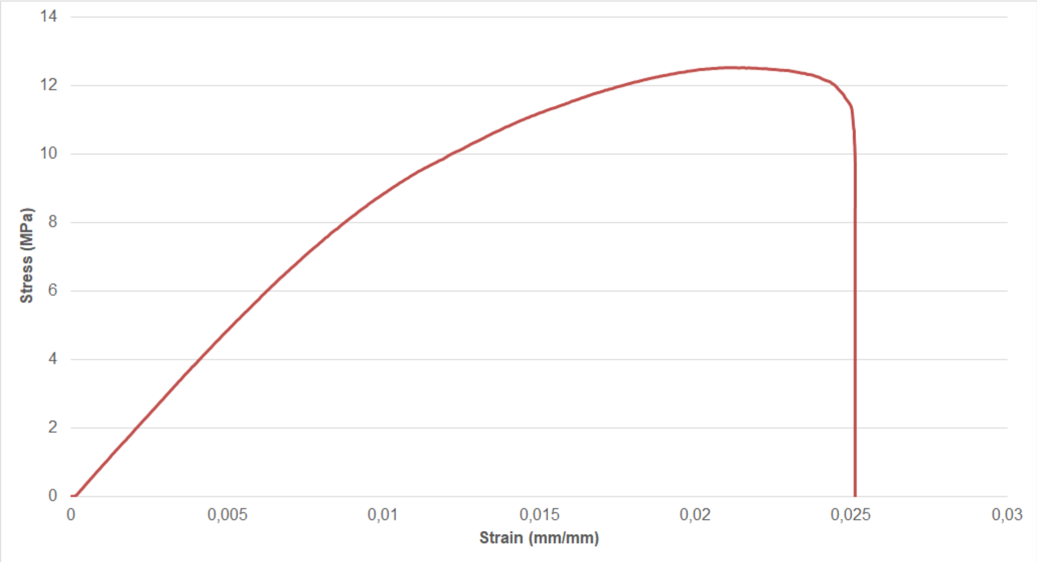

Figure 4.13. Stress – Strain graph of ABS + 2wt% $CaCO_3$ specimen

Tensile test graph of ABS + 3wt% $CaCO_3$ specimen can be seen in Figure 4.14.

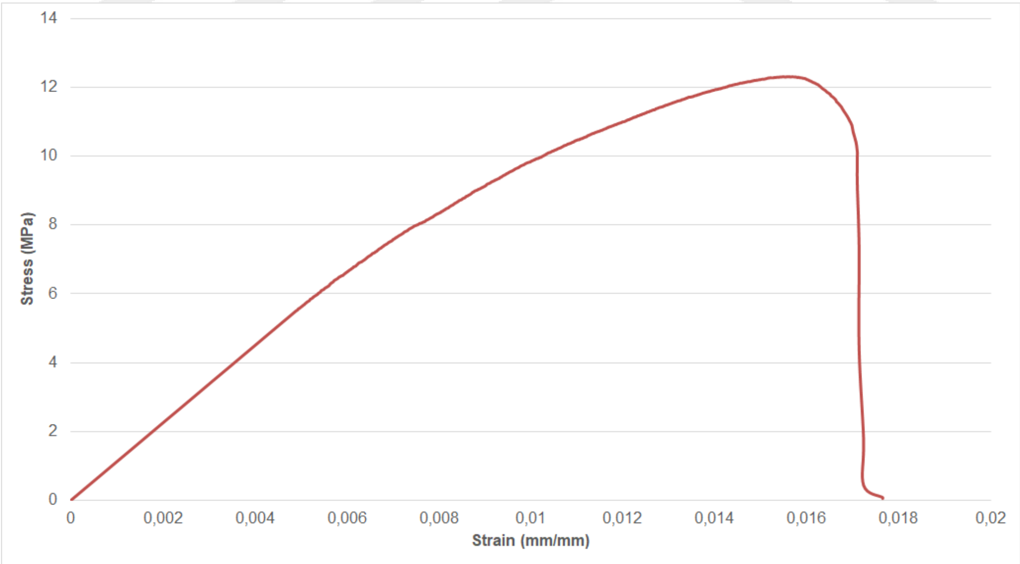

Figure 4.14. Stress – Strain graph of ABS + 3wt% $CaCO_3$ specimen

Tensile test graph of ABS + 3wt% $CaCO_3$ specimen can be seen in Figure 4.15.

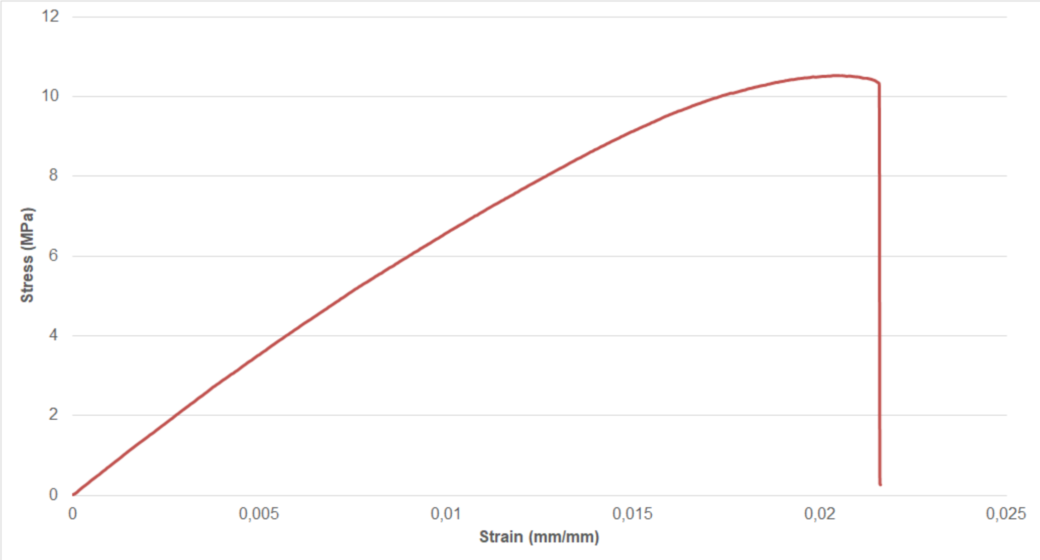

Figure 4.15. Stress – Strain graph of ABS + 5wt% $CaCO_3$ specimen

The calculated mechanical properties of Modulus of Elasticity and Poisson's Ratio are given in Table 4.2 along with the density values of beams.

Table 4.2. Modulus of Elasticity, Poisson's Ratio, Tensile Strength and Density values

	Modulus of Elasticity (MPa)	**Poisson's Ratio**	**Yield Strength (MPa)**	**Ultimate Strength (MPa)**	**Density (kg/m^3)**
Pure ABS	1108	0.261	9.1	11.95	699.38
ABS + 1wt% $CaCO_3$	1050	0.224	9.66	12.62	684.66
ABS + 2wt% $CaCO_3$	1084	0.213	9,80	12,41	706.74
ABS + 3wt% $CaCO_3$	1114	0.217	8.95	12.10	704.29
ABS + 5wt% $CaCO_3$	768	0.173	7.80	10.65	613.49

After getting the mechanical properties of the materials, numerical calculations were able to be performed by using these properties as input for material properties in ANSYS.

4.1.3. Numerical Calculation Results for beams of ABS + $CaCO_3$ nanoparticles

As discussed in the previous section, the numerical calculations for Natural Frequency values were obtained in ANSYS software. The Elastic Modulus values obtained from the tensile tests and density values calculated by the weight of the samples were used as input in Engineering Data section. Then Modal analysis was performed as explained in detail in the previous section. The screenshot from ANSYS modal analysis of pure ABS beam can be seen in Figure 4.16.

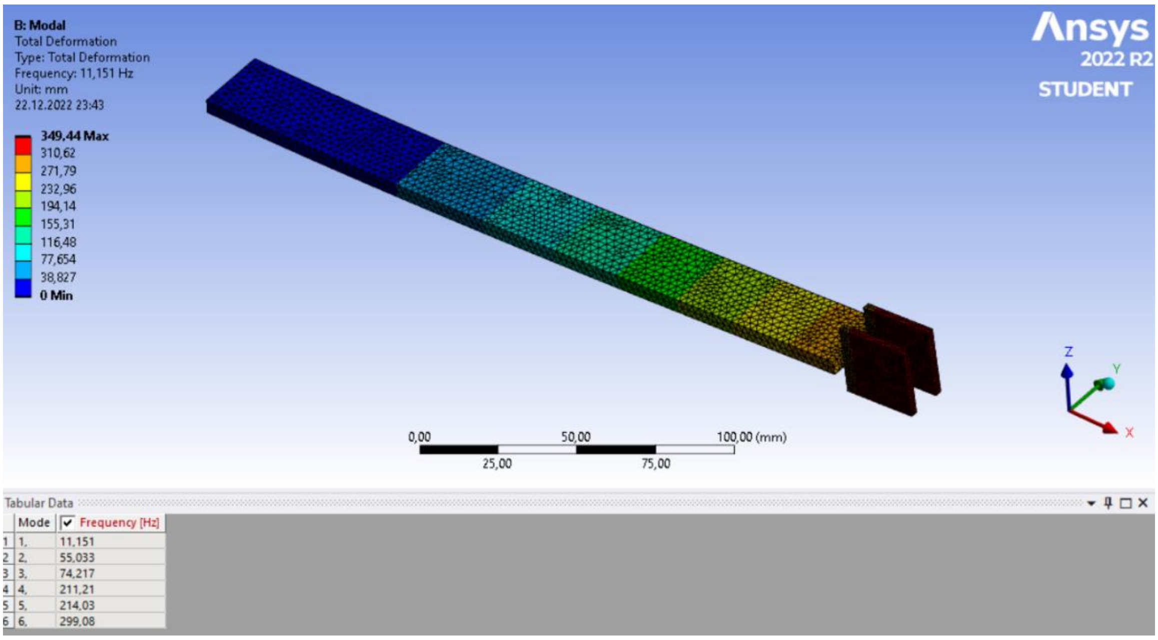

Figure 4.16. Modal analysis result in ANSYS for pure ABS beam

The screenshot from ANSYS modal analysis of ABS+1wt%$CaCO_3$ nanocomposite specimen can be seen in Figure 4.17.

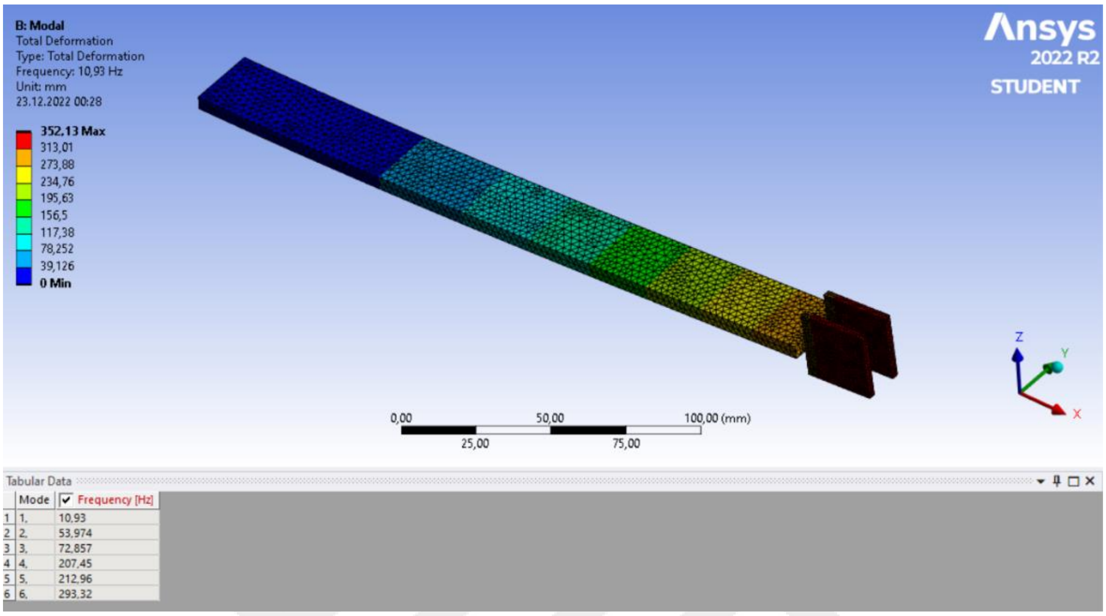

Figure 4.17. Modal analysis results in ANSYS for ABS + 1wt% $CaCO_3$ beam

The screenshot from ANSYS modal analysis of ABS+2wt%$CaCO_3$ nanocomposite specimen can be seen in Figure 4.18.

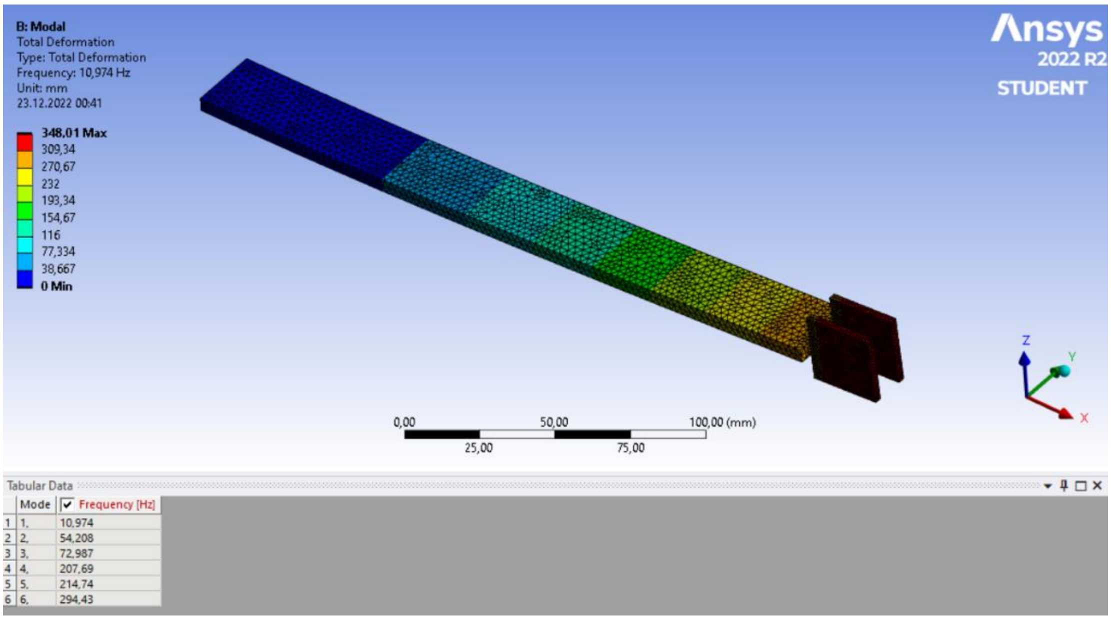

Figure 4.18. Modal analysis results in ANSYS for ABS + 2wt% $CaCO_3$ beam

The screenshot from ANSYS modal analysis of ABS+3wt%$CaCO_3$ nanocomposite specimen can be seen in Figure 4.19.

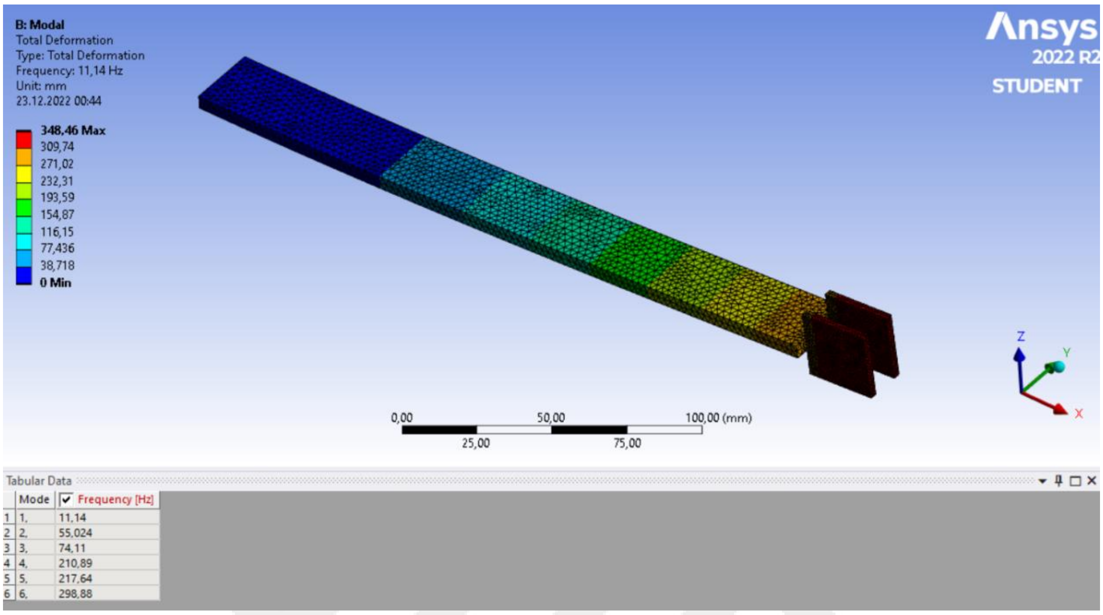

Figure 4.19. Modal analysis results in ANSYS for ABS + 3wt% $CaCO_3$ beam

The screenshot from ANSYS modal analysis of ABS+5wt%$CaCO_3$ nanocomposite specimen can be seen in Figure 4.20.

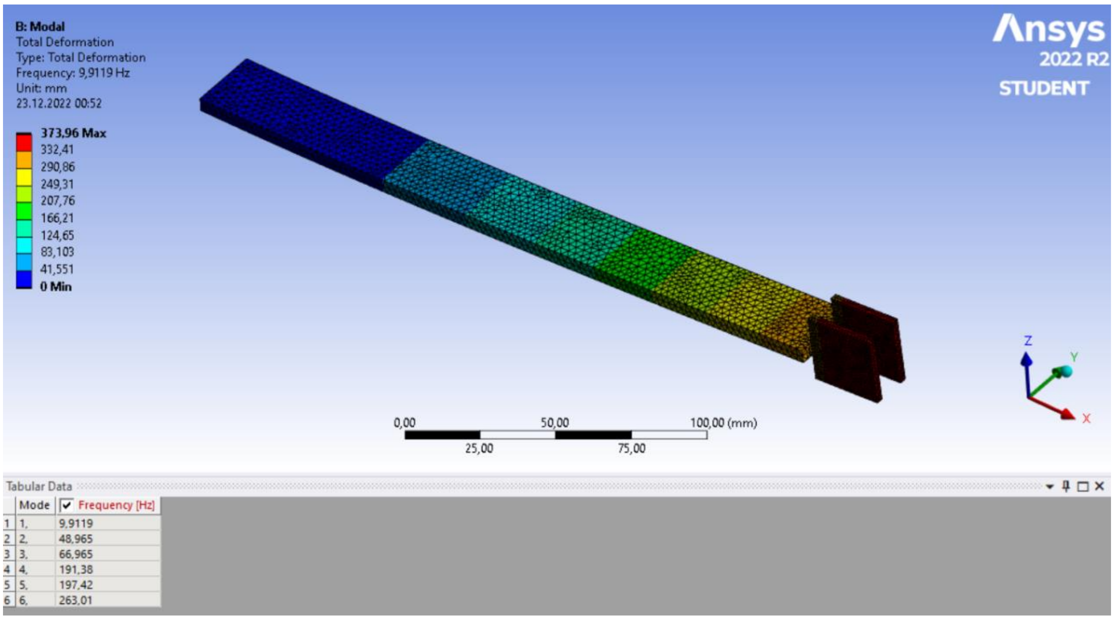

Figure 4.20. Modal analysis results in ANSYS for ABS + 5wt% $CaCO_3$ beam

As can be seen in the Figures above, ANSYS performs the modal analysis for the first six modes of natural frequency values. The numerical results for pure ABS and all ABS+$CaCO_3$ nanocomposite beams can be seen in Table 4.3.

Table 4.3. Numerically calculated natural frequency values of $CaCO_3$ beams in first 6 modes

	Pure ABS	**ABS + 1wt% $CaCO_3$**	**ABS + 2wt% $CaCO_3$**	**ABS + 3wt% $CaCO_3$**	**ABS + 5wt% $CaCO_3$**
Natural Frequency Mode 1 (Hz)	11.151	10.93	10.97	11.14	9.91
Natural Frequency Mode 2 (Hz)	55.033	53.97	54.20	55.02	48.965
Natural Frequency Mode 3 (Hz)	74.217	72.85	72.98	74.11	66.965
Natural Frequency Mode 4 (Hz)	211.21	207.45	207.69	210.89	191.38
Natural Frequency Mode 5 (Hz)	214.03	212.96	214.74	217.64	197.42
Natural Frequency Mode 6 (Hz)	299.08	293.32	294.43	298.88	263.01

4.2. Experimental and Numerical Results for Beams of ABS + CB Nanoparticles

4.2.1. Experimental Vibration Test Results for beams of ABS + CB nanoparticles

Beams of pure ABS and nanoparticles of CB added in various weight fractions were tested and time – displacement data were logged via the VDAS software and the data was exported to an Excel file. The file was read by the Matlab code and first, the time – displacement graphs, FFT graphs, and curve-fitting graphs of the tests were plotted. Time - displacement and curve fitting graphs of an ABS + 0.3wt% CB specimen are seen in Figure 4.21.

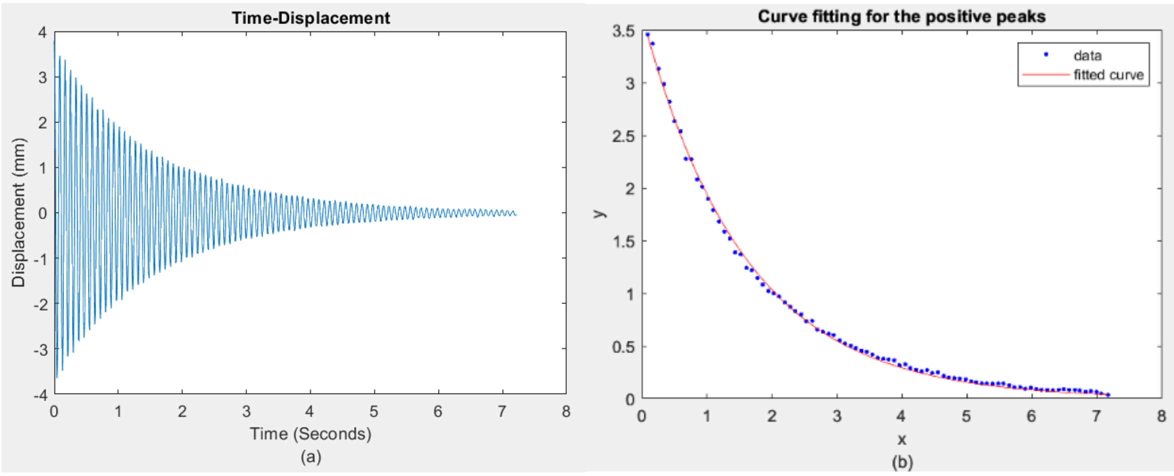

Figure 4.21. Resulting graphs of ABS + 0.3wt% CB beam: (a) Time history, (b) Curve fitting

The FFT graph of a pure ABS + 0.3wt% CB specimen can be seen in Figure 4.22.

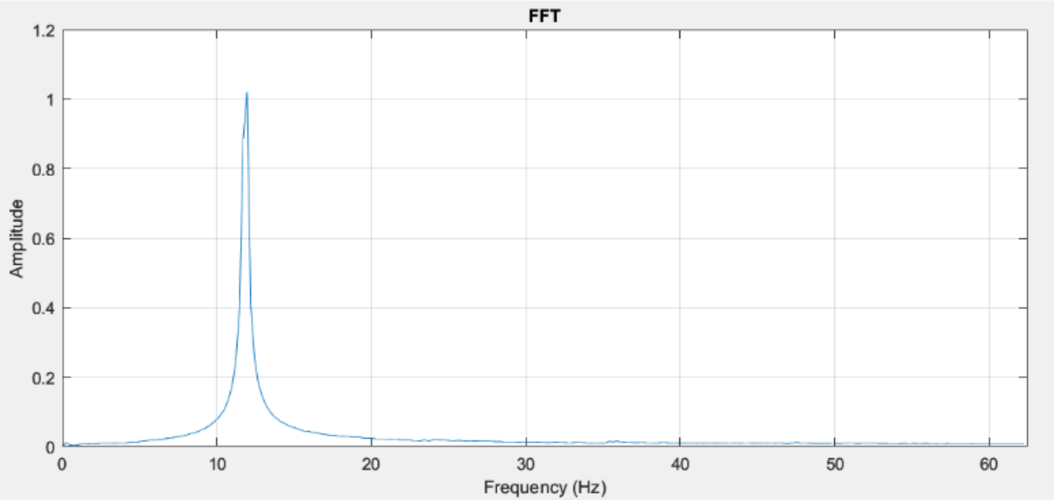

Figure 4.22. FFT analysis graph of ABS + 0.3wt% CB beam

Time - displacement and curve fitting graphs of an ABS + 1wt% CB specimen are seen in Figure 4.23.

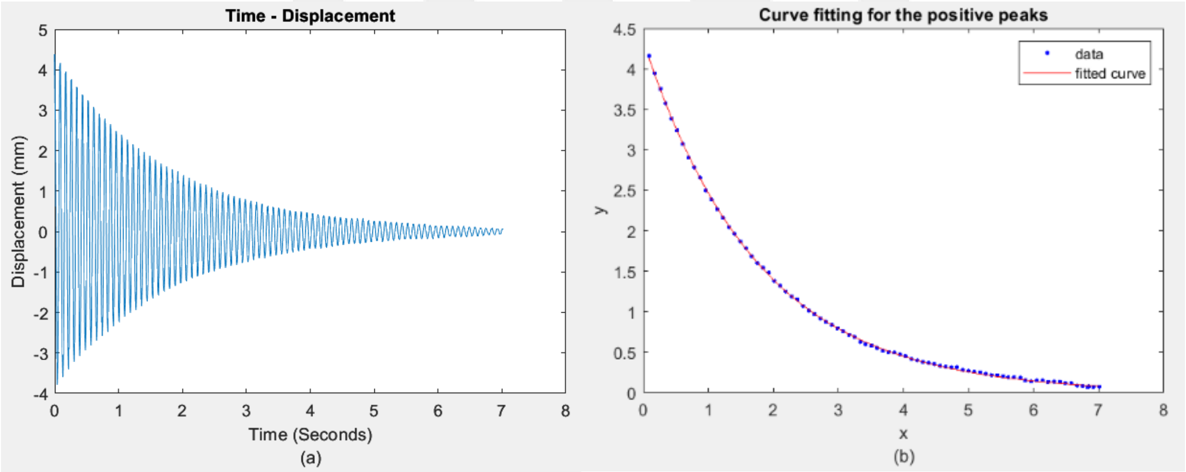

Figure 4.23. Resulting graphs of ABS + 1wt% CB beam: (a) Time history, (b) Curve fitting

The FFT graph of a pure ABS + 1wt% CB specimen can be seen in Figure 4.24.

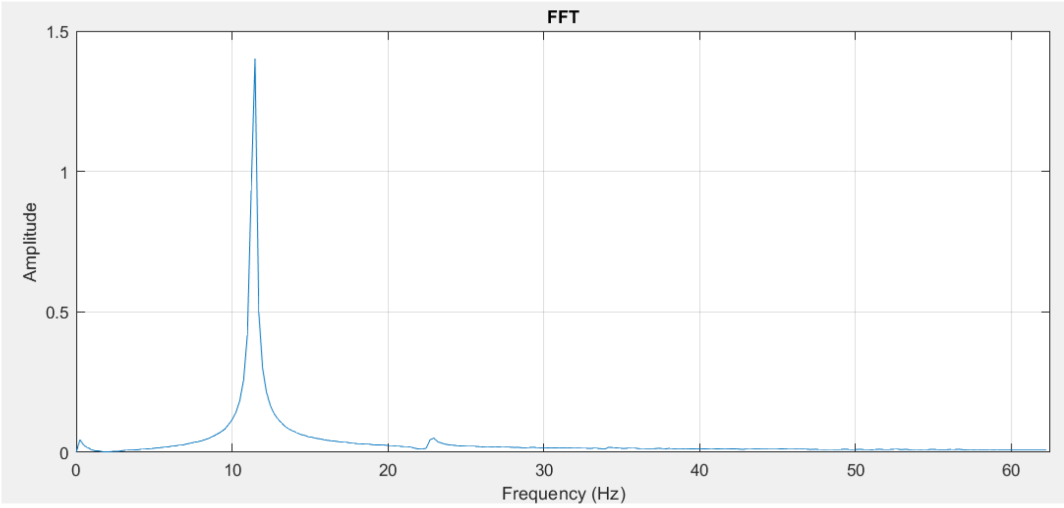

Figure 4.24. FFT analysis graph of ABS + 1wt% CB beam

Time - displacement and curve fitting graphs of an ABS + 2wt% CB specimen are seen in Figure 4.25.

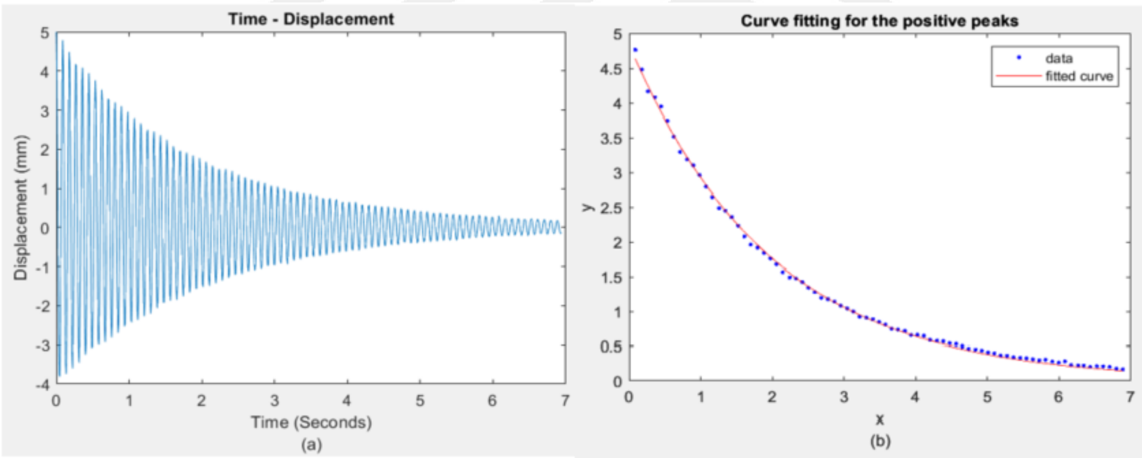

Figure 4.25. Resulting graphs of ABS + 2wt% CB beam: (a) Time history, (b) Curve fitting

The FFT graph of a pure ABS + 2wt% CB specimen can be seen in Figure 4.26.

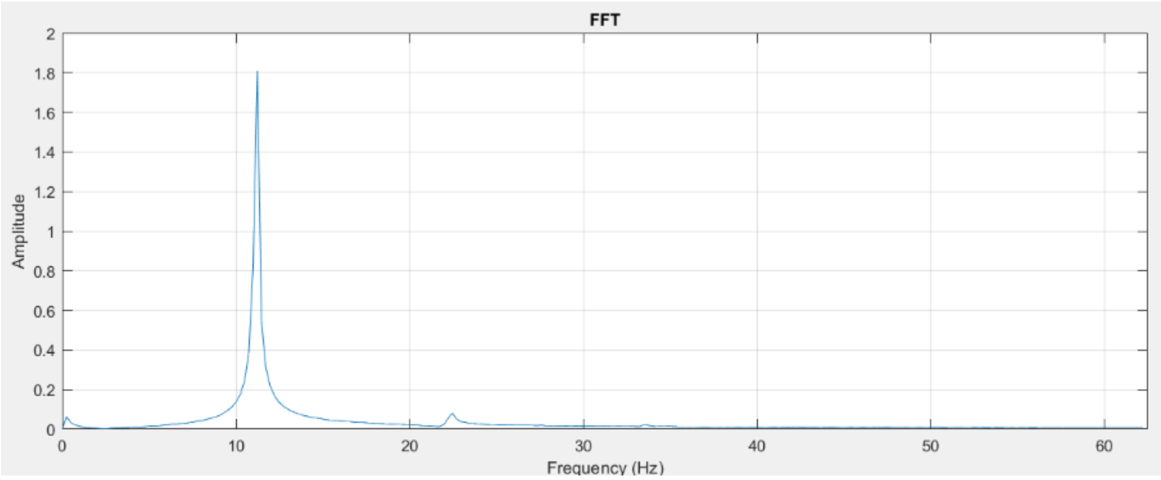

Figure 4.26. FFT analysis graph of ABS + 2wt% CB beam

All experimental vibration test results with natural frequency and damping ratio values of CB nanocomposite beams can be seen in Table 4.4.

Table 4.4. Experimental test results for CB/ABS nanocomposite beams

	Damped Natural Frequency (Hz)	**Natural Frequency** (Hz)	**Damping Ratio**
Pure ABS	11.4746	11.4748	0.0063
ABS + 0.3wt% CB	11.9629	11.9633	0.0088
ABS + 1wt% CB	11.4746	11.4750	0.0082
ABS + 2wt% CB	11.2305	11.2307	0.0075

4.2.2. Experimental Tensile Test Results for beams of ABS + CB nanoparticles

Tensile test graph of ABS + 0.3wt%CB specimen can be seen in Figure 4.27.

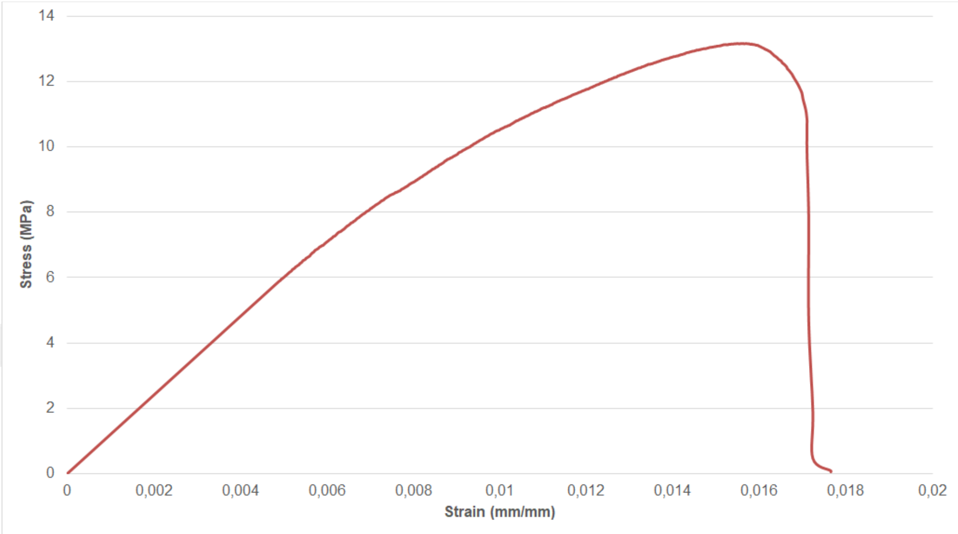

Figure 4.27. Stress – Strain graph of ABS + 0.3wt% CB specimen

Tensile test graph of ABS + 1wt% CB specimen can be seen in Figure 4.28.

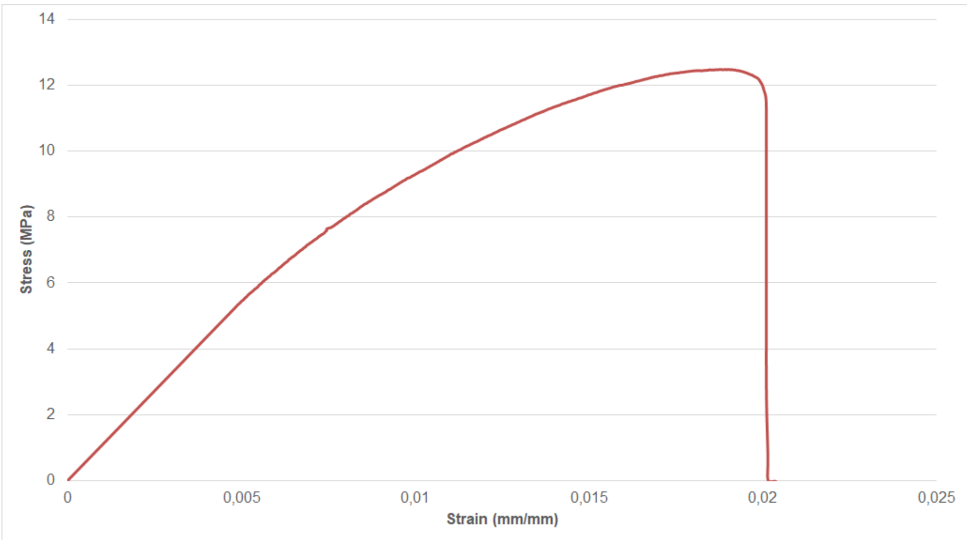

Figure 4.28. Stress – Strain graph of ABS + 1wt% CB specimen

Tensile test graph of ABS + 2wt% CB specimen can be seen in Figure 4.29.

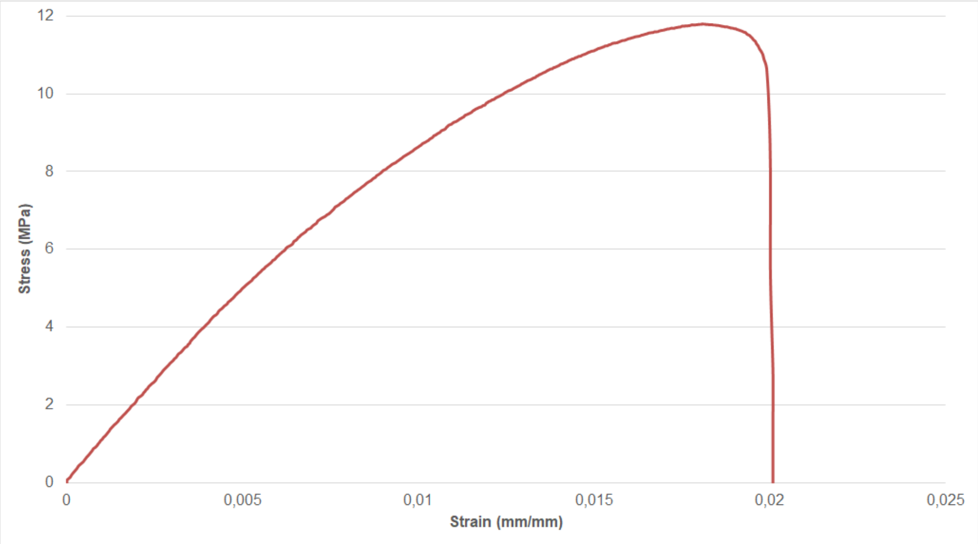

Figure 4.29. Stress – Strain graph of ABS + 2wt% CB specimen

All tensile test results are given in Table 4.5.

Table 4.5. Mechanical properties of beam specimens after tensile testing along with Density values of CB samples

	Modulus of Elasticity (MPa)	**Poisson's Ratio**	**Yield Strength (MPa)**	**Ultimate Strength (MPa)**	**Density (kg/m^3)**
Pure ABS	1108	0.261	9.1	11.95	699.38
ABS + 0.3wt% CB	1124	0.218	10.35	13.05	640.49
ABS + 1wt% CB	1072	0.200	9.85	12.30	687.11
ABS + 2wt% CB	1042	0.172	9.15	11.80	692.02

4.2.3. Numerical Calculation Results for beams of ABS + CB nanoparticles

The screenshot from ANSYS modal analysis of pure ABS beam can be seen in Figure 4.30.

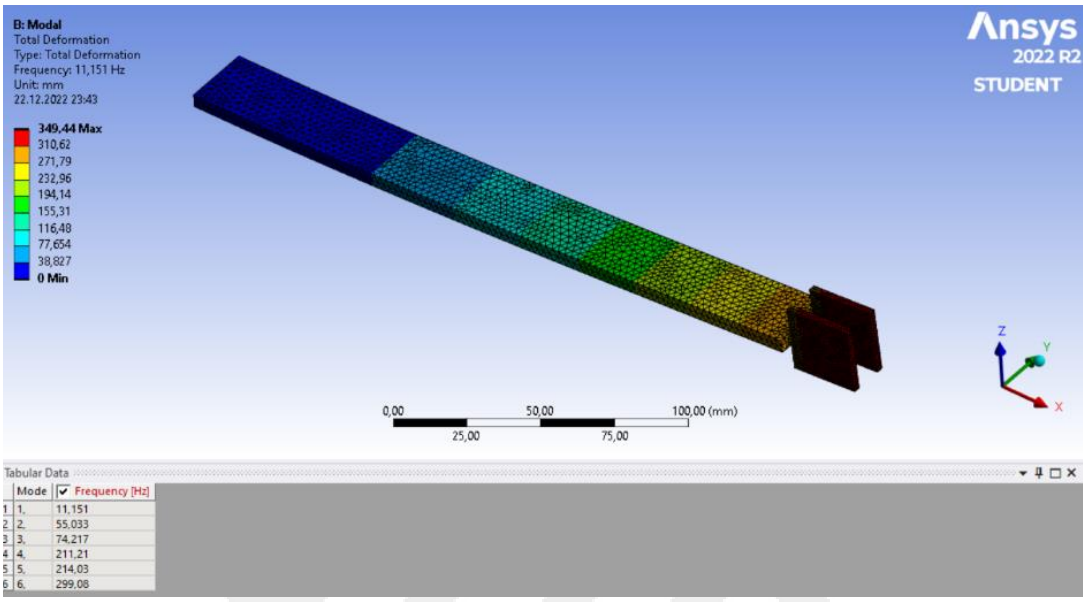

Figure 4.30. Modal analysis result in ANSYS for pure ABS beam

The screenshot from ANSYS modal analysis of an ABS + 0.3wt% CB beam can be seen in Figure 4.31.

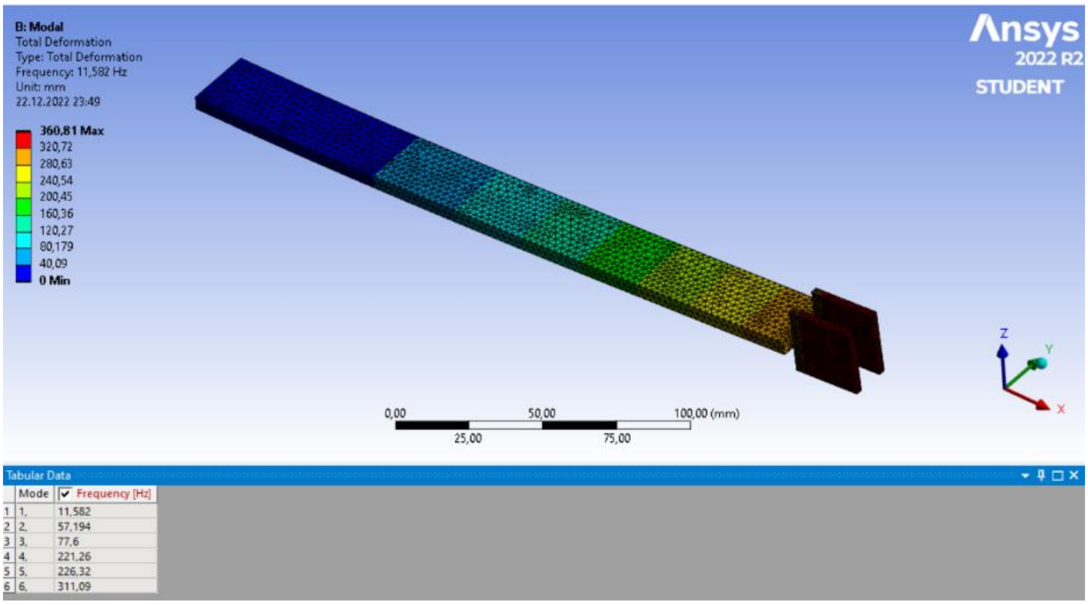

Figure 4.31. Modal analysis result in ANSYS for ABS + 0.3wt% CB beam

The screenshot from ANSYS modal analysis of an ABS + 1wt%CB beam can be seen in Figure 4.32.

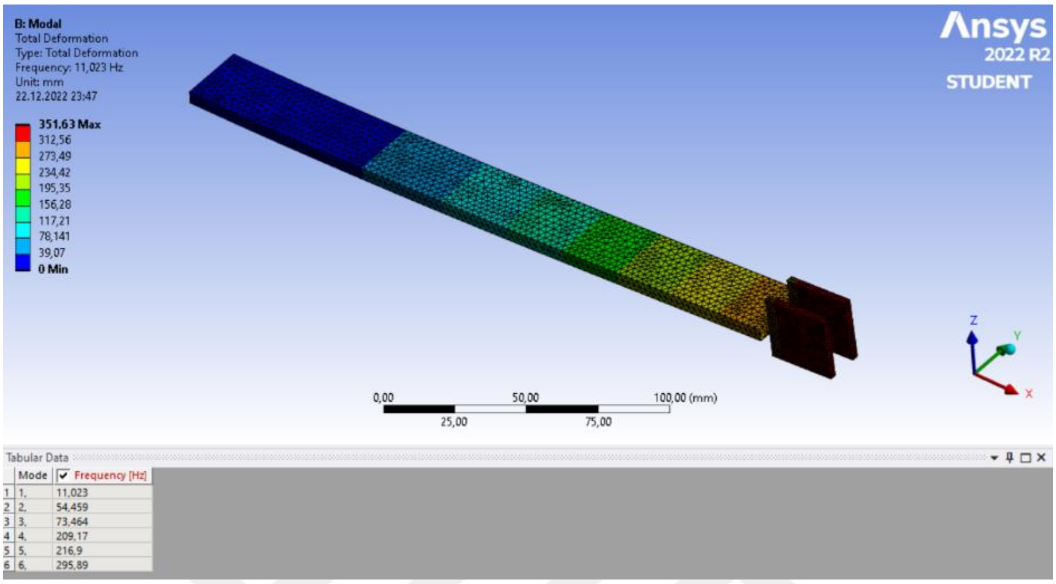

Figure 4.32. Modal analysis result in ANSYS for ABS + 1wt% CB beam

The screenshot from ANSYS modal analysis of an ABS + 1wt%CB beam can be seen in Figure 4.33.

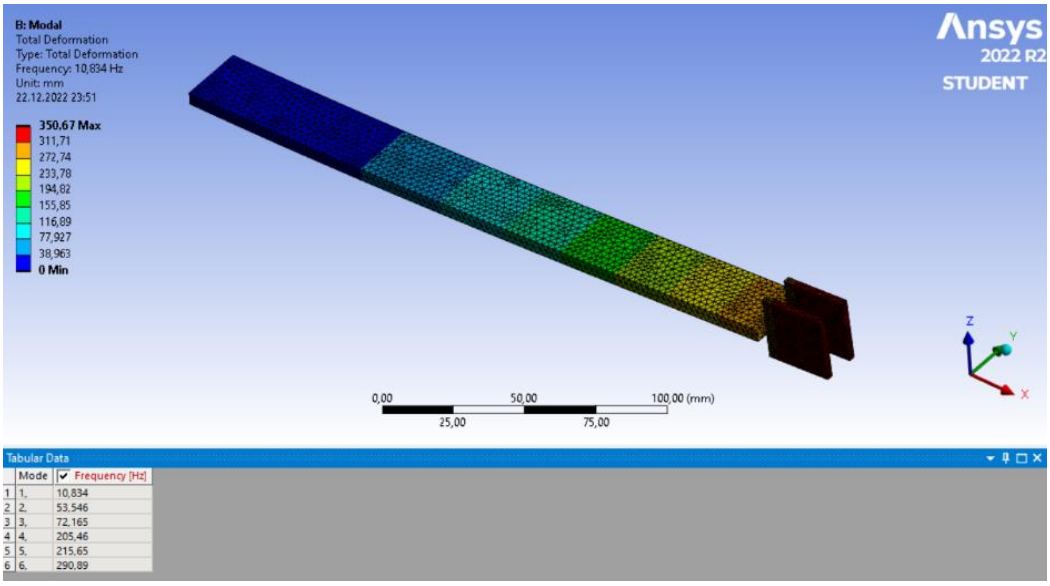

Figure 4.33. Modal analysis result in ANSYS for ABS + 2wt% CB beam

Table 4.6. Numerically calculated natural frequency values of CB beams in first 6 modes

	Pure ABS	ABS + 0.3wt% CB	ABS + 1wt% CB	ABS + 2wt% CB
Natural Frequency Mode 1 (Hz)	11.151	11.582	11.023	10.834
Natural Frequency Mode 2 (Hz)	55.033	57.194	54.459	53.546
Natural Frequency Mode 3 (Hz)	74.217	77.6	73.464	72.165
Natural Frequency Mode 4 (Hz)	211.21	221.26	209.17	205.46
Natural Frequency Mode 5 (Hz)	214.03	226.32	216.9	215.65
Natural Frequency Mode 6 (Hz)	299.08	311.09	295.89	290.89

4.3. SEM results of nanocomposite specimens

4.3.1. SEM results of ABS + $CaCO_3$ nanocomposites

The SEM specimens were taken from the fractured surfaces of tensile test specimens 3D printed with the nanocomposite filaments. The first specimen was the pure ABS material. The SEM image in 200000 times magnified mode for pure ABS specimen can be seen in Figure 4.34.

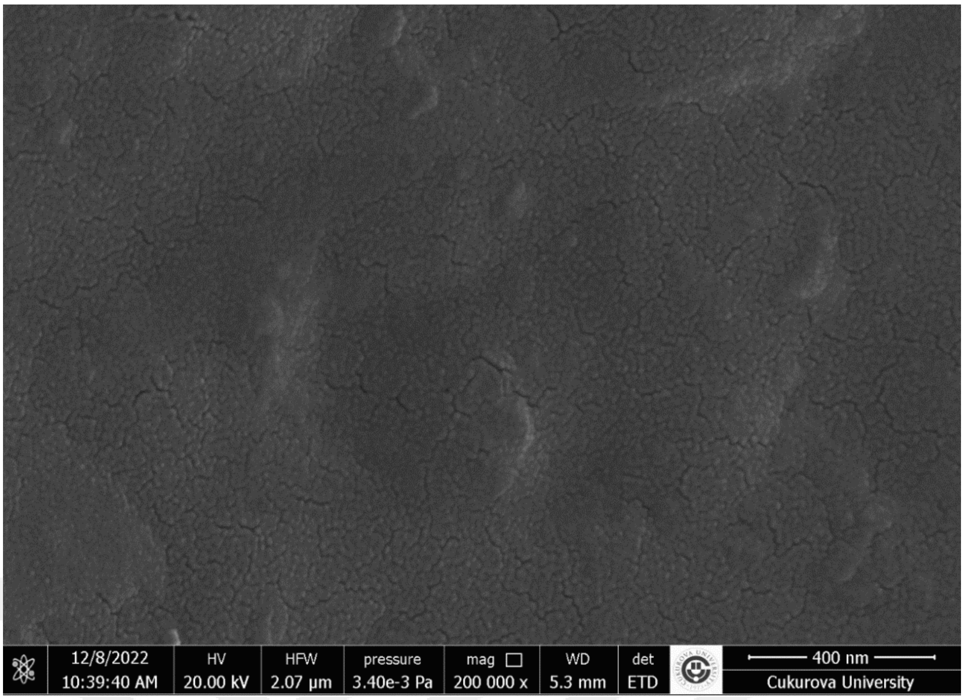

Figure 4.34. SEM image of 200000 times magnified pure ABS specimen

The 100 times magnified image of the pure ABS specimen can be seen in Figure 4.35. It can be concluded from the image that the layers of the specimen were evenly distributed. This shows the good operation of the 3D printer during the printing process. It also reflects the quality of the pure ABS filament produced in house because the beads of the deposited layers are very uniform and smooth on the surface. Figure 4.36 shows the 200000 times magnified image of 1wt% $CaCO_3$ nanocomposite specimen.

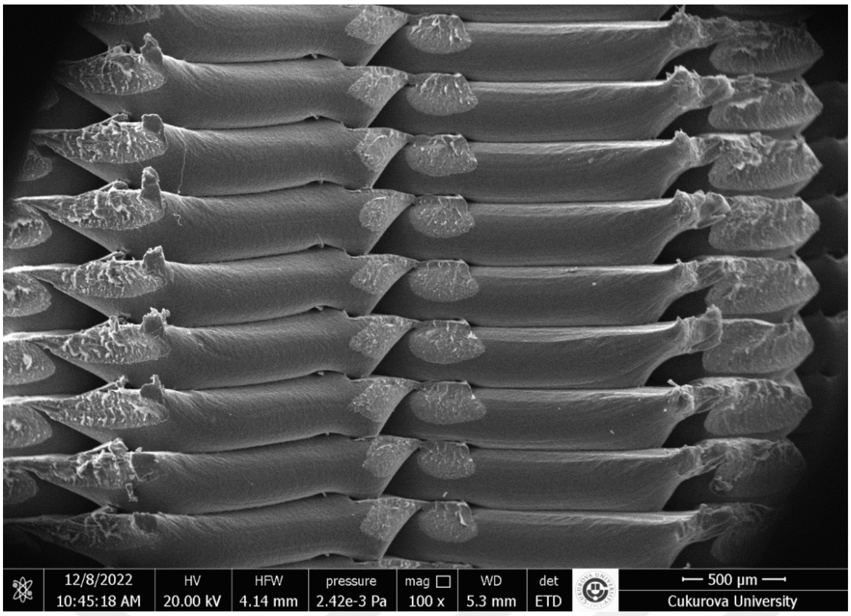

Figure 4.35. SEM image of 100 times magnified pure ABS specimen

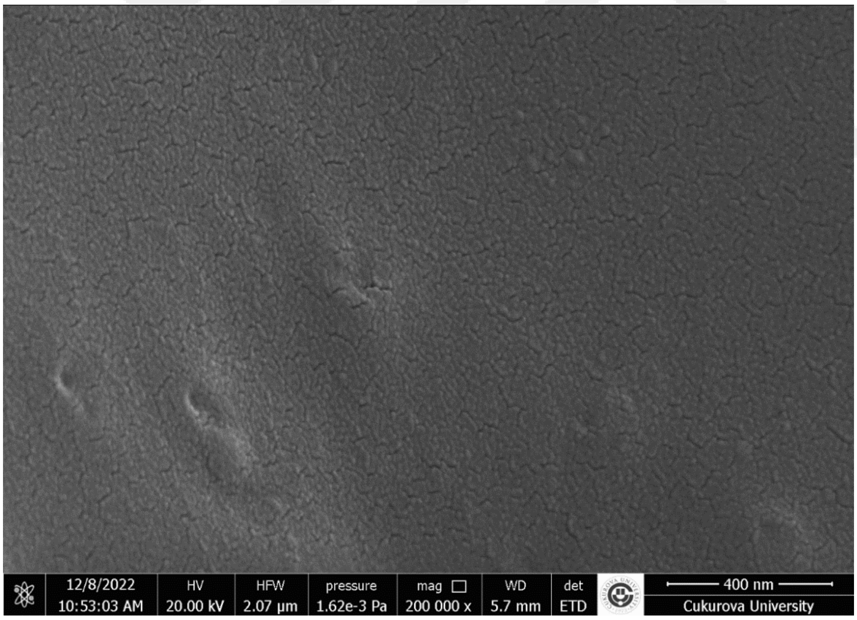

Figure 4.36. SEM image of 200000 times magnified ABS + 1wt% $CaCO_3$ specimen

As seen in Figure 4.36 there seems to be no particular difference compared to the pure ABS image. It is hard to image low weight fractions of $CaCO_3$ nanoparticles in ABS matrix, especially in low weight fraction values [44]. The same situation was observed for 2wt%

$CaCO_3$ nanocomposite specimen and as seen in Figure 4.37. the $CaCO_3$ nanoparticles were not observed in the 200000 times magnified image of 2wt% $CaCO_3$ nanocomposite specimen.

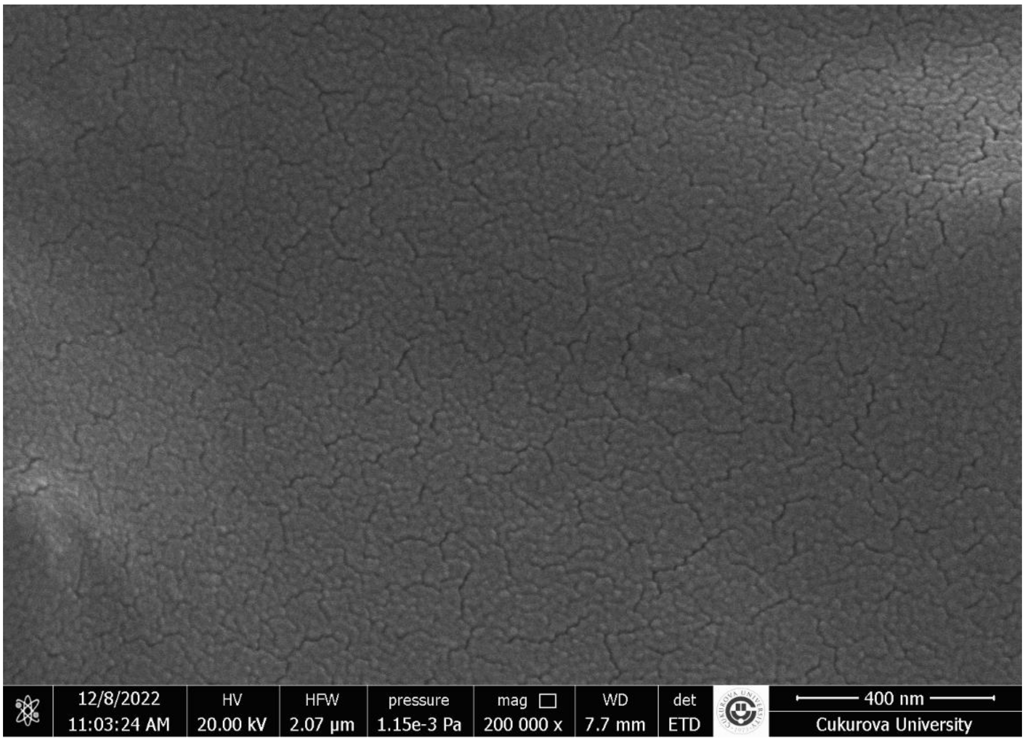

Figure 4.37. SEM image of 200000 times magnified ABS + 2wt% $CaCO_3$ specimen

The 200000 times magnified SEM image of 3wt% $CaCO_3$ nanocomposite specimen can be seen in Figure 4.38. We observe an agglomeration of $CaCO_3$ nanoparticles in close detail. It can be observed from the image that several particles were agglomerated. It is known that nano-$CaCO_3$ particles are prone to agglomeration due to their high surface tension [44]. One agglomerate was captured on the screen and these agglomerations were expected in higher weight fractions.

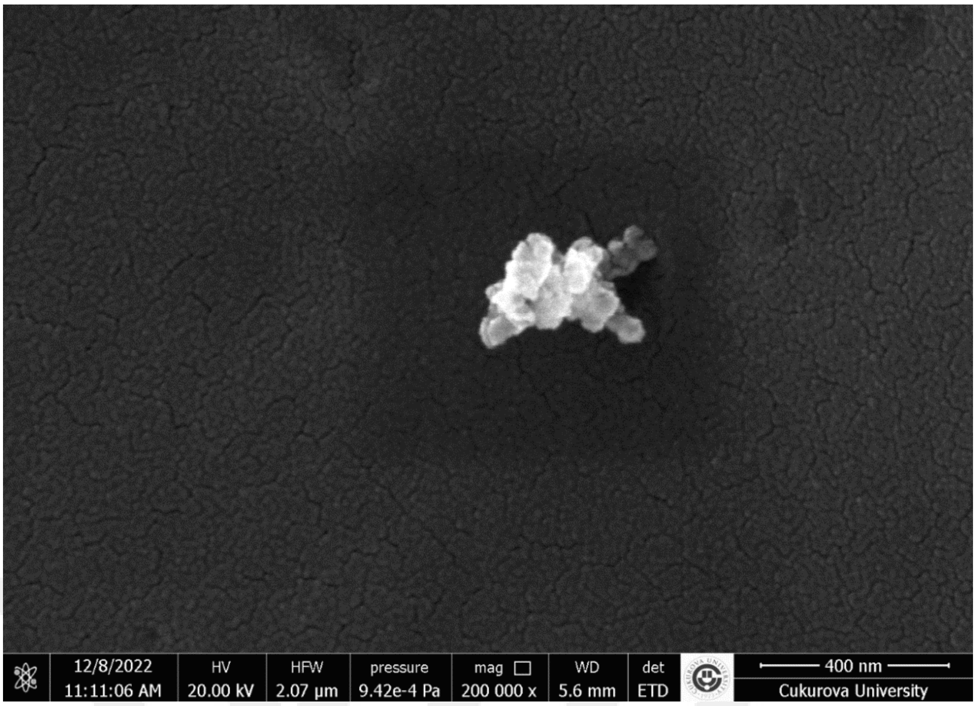

Figure 4.38. SEM image of 200000 times magnified ABS + 3wt% $CaCO_3$ specimen displaying an agglomeration of $CaCO_3$ nanoparticles

When we look at the 5000 times magnified image of the 3wt% $CaCO_3$ nanocomposite specimen, we also see smaller particles distributed in the matrix however the number of these particles are small and it shows a less dense dispersion of nanoparticles in various agglomeration sizes smaller than the large one zoomed in Figure 4.38. The 5000 times magnified SEM image of 3wt% $CaCO_3$ nanocomposite specimen can be seen in Figures 4.39 and 4.40.

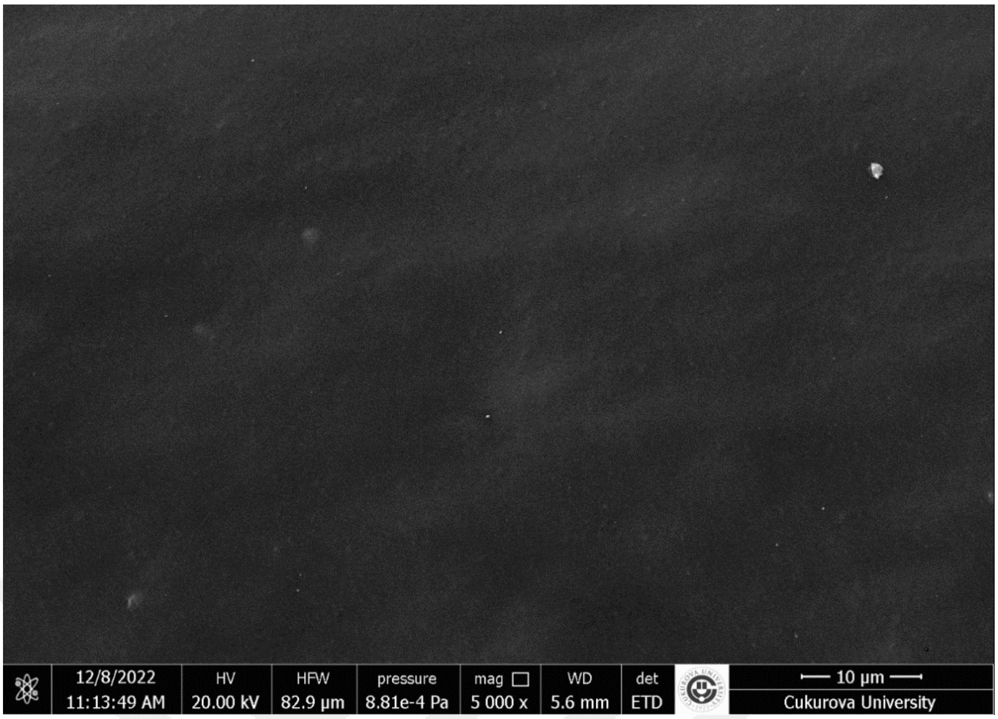

Figure 4.39. SEM image of 5000 times magnified ABS + 3wt% $CaCO_3$

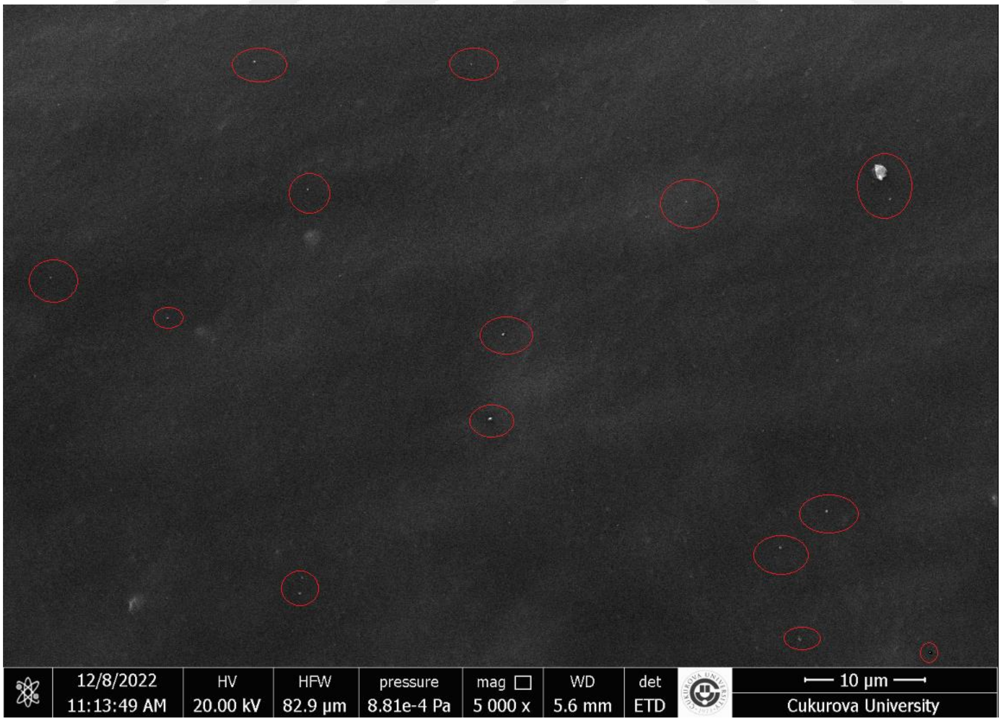

Figure 4.40. SEM image of 5000 times magnified ABS + 3wt% $CaCO_3$ specimen particles

The 5000 times magnified SEM image of 5wt% $CaCO_3$ nanocomposite specimen can be seen in Figure 4.41. It is evident that there are larger number of agglomerations compared to all other weight fractions and much more particles of $CaCO_3$ agglomerated in many different sizes are observed. A large agglomeration of $CaCO_3$ particles can be seen in the 200000 times magnified SEM image of 5wt% $CaCO_3$ nanocomposite specimen in Figure 4.42. It is expected that, as the weight fraction increase, the maximum size of the agglomeration tends to increase accordingly.

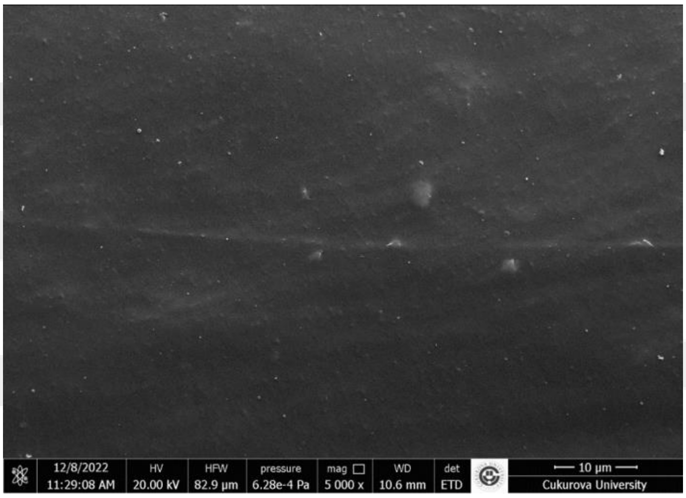

Figure 4.41. SEM image of 5000 times magnified ABS + 5wt% $CaCO_3$ specimen particles

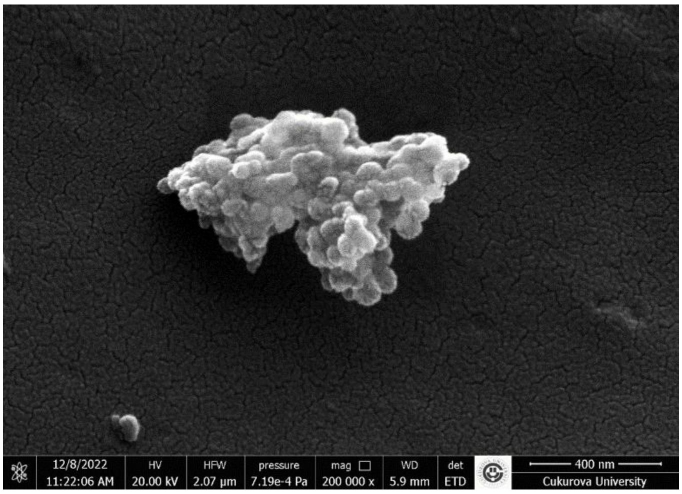

Figure 4.42. SEM image of 200000 times magnified ABS + 5wt% $CaCO_3$ specimen displaying an agglomeration of $CaCO_3$ nanoparticles

When we take a look at Table 4.2, we observe that all cantilever beam specimens have densities of similar values except the beam with 5wt% $CaCO_3$ content. When the reason for such difference was considered, it was found to be useful to investigate the SEM image from this perspective. When the images of layers of the FDM process were examined, the beam with low density exhibited excessive numbers of voids (or craters) on the surface of the layer beads. More voids may be inside the beads as well. This low density value may be attributed to the voids in the beads and these voids may be formed due to the nanoparticles addition and high agglomerations of $CaCO_3$ nanoparticle content [41]. As seen in pure ABS images, no voids or craters are present on the surface of the beads. The beads of 5wt% $CaCO_3$ specimen can be seen in Figure 4.43.

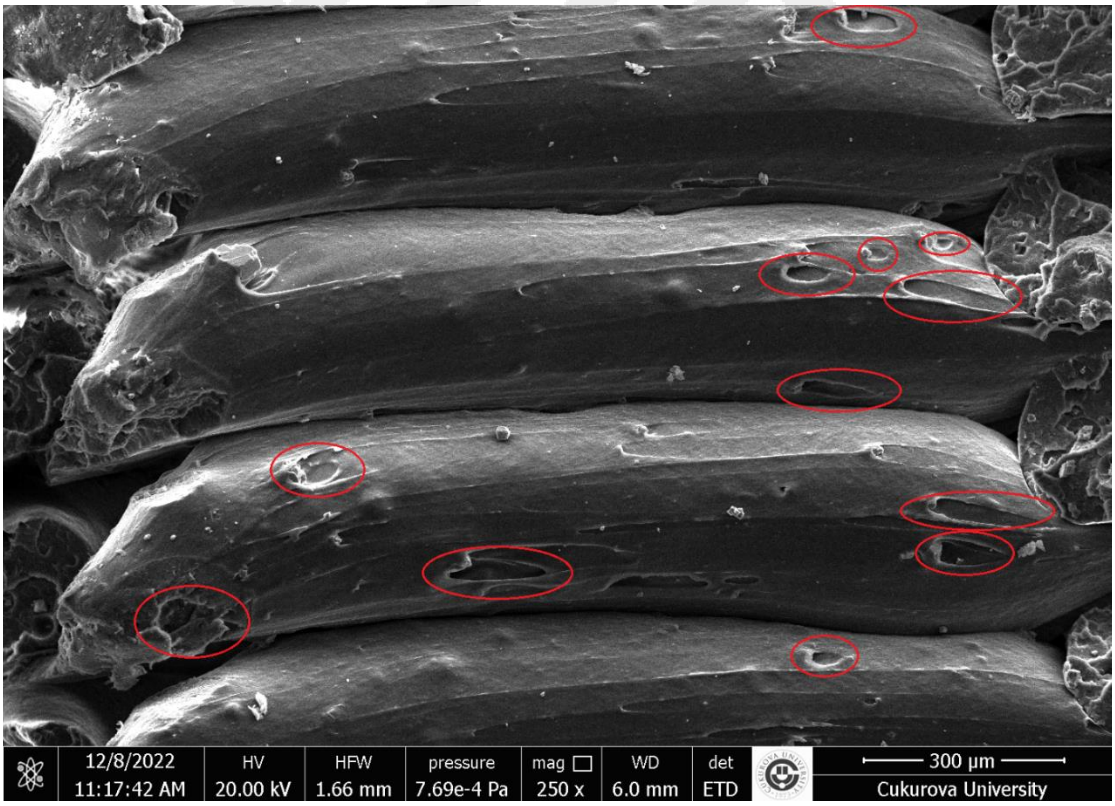

Figure 4.43. SEM image of 250 times magnified ABS + 5wt% $CaCO_3$ specimen displaying the voids on the beads

The comparison of pure ABS and 5wt% $CaCO_3$ specimens can be seen in Figure 4.44.

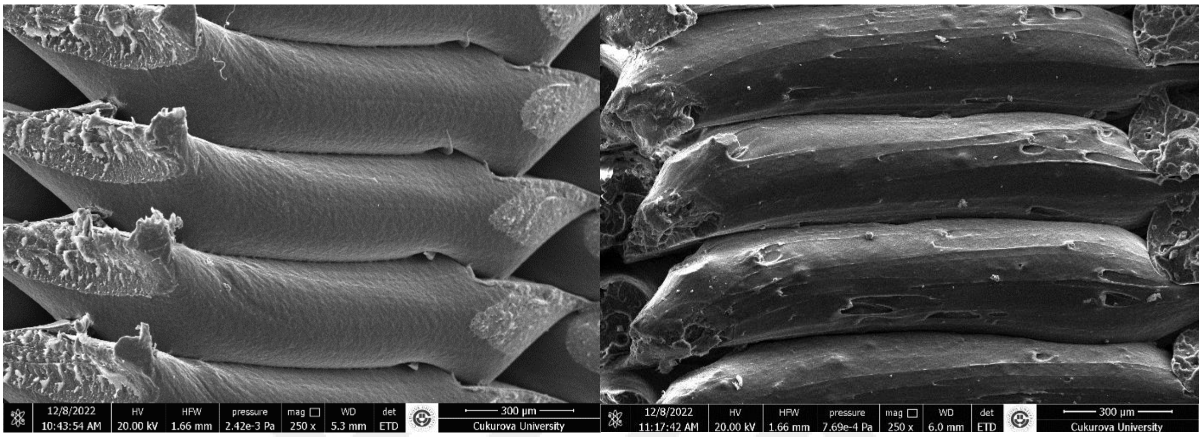

Figure 4.44. Pure ABS beads (on the left) and ABS + 5wt% $CaCO_3$ beads (on the right)

From Figure 4.45 it can be clearly seen that pure ABS beads have smooth surfaces with no craters or voids on them. When the images of all specimens were examined, it was observed that a few voids occurred with 1wt% $CaCO_3$ content and with every increase in the nanoparticle content the amount of voids increased in the surface of the beads reaching maximum with 5wt% $CaCO_3$ content. These voids may also be the reason why the stiffness and strength of specimens decreased.

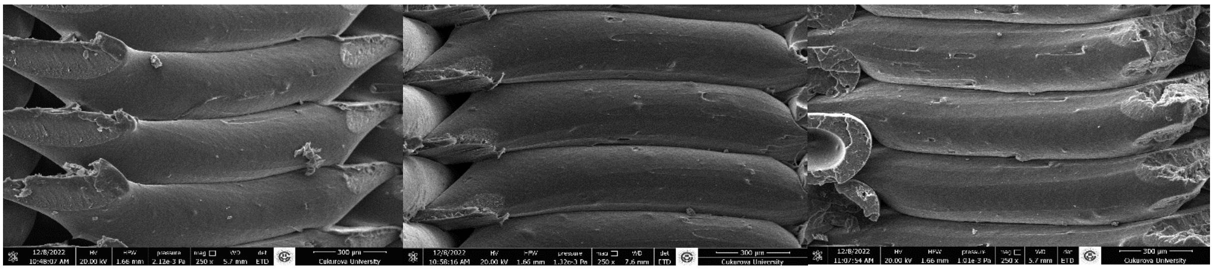

Figure 4.45. Images of layer beads for 1,2 and 3 wt% $CaCO_3$ content from left to right

4.3.2. SEM results of ABS + CB nanocomposites

The SEM images of ABS + 2wt% CB are seen in Figure 4.46. It is evident that the micro-structure looks significantly different than pure ABS. The CB particles are very hard to distinguish from ABS matrix due to the black color caused by Carbon Black. White zones are detected in the SEM images and the interpretation that these white zones represent CB nanoparticles was hypothesized. By using the image processing software ImageJ, the area of these white zones was approximately calculated. The comparison of white zones and the selected area in ImageJ software for ABS + 2wt% CB specimen can be seen in Figure 4.46. The percentage of the area of the zones to the area of all the image area was calculated.

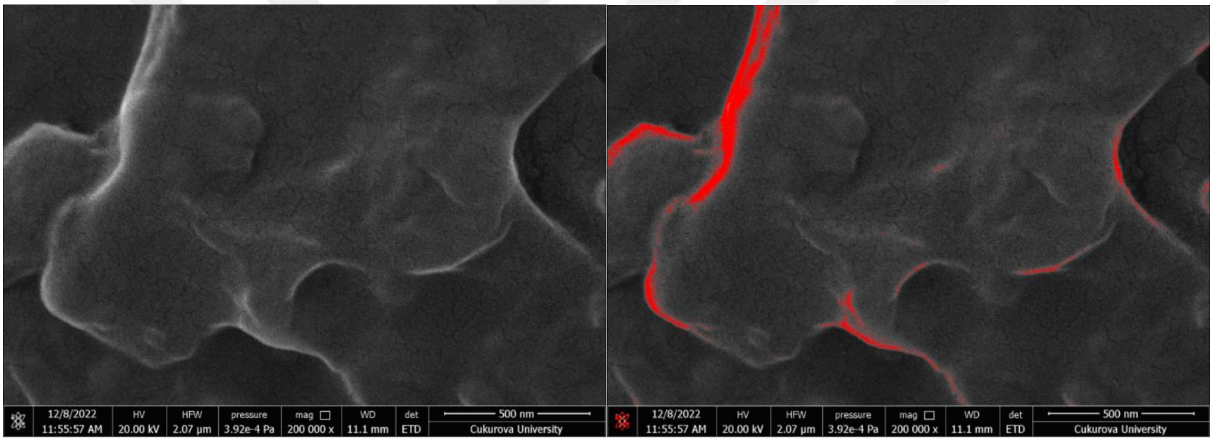

Figure 4.46. Comparison of white zones

The calculation of the image from 2wt% CB nanoparticle performed by image processing software can be seen in Figure 4.47. As seen from Figure 4.47 the ratio of the area of the white zones to the area of the complete image is calculated as 1.86% by the default threshold function of the software. It can be seen that this image was zoomed 200000 times and this portion of image may contain less particles in percentage than the complete specimen itself causing a slight error

This function called threshold can be fine-tuned and some adjustments were made in detail to capture most of the white zones in the image to get the idea that these white areas represent CB nanoparticles. Consequently, this calculation gives a strong impression of white zones representing the CB nanoparticles. We should also consider that the images will neither give us the exact weight fraction nor the volume fraction of the composites but maybe some value in between those values.

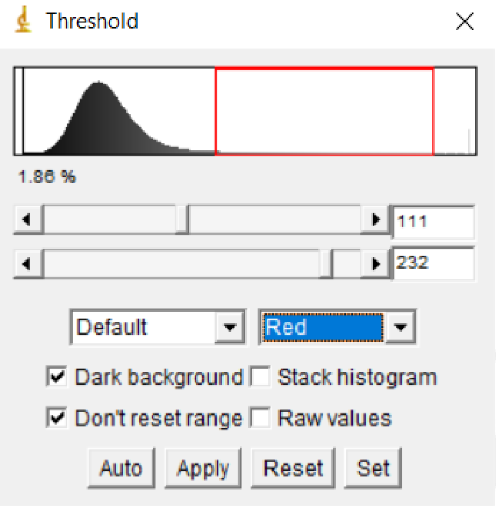

Figure 4.47. Area fraction calculation of 2wt% CB image in 200000 times magnification

Figure 4.48 shows the threshold operation for ABS + 1wt% CB nanocomposite SEM image for 200000 times magnification.

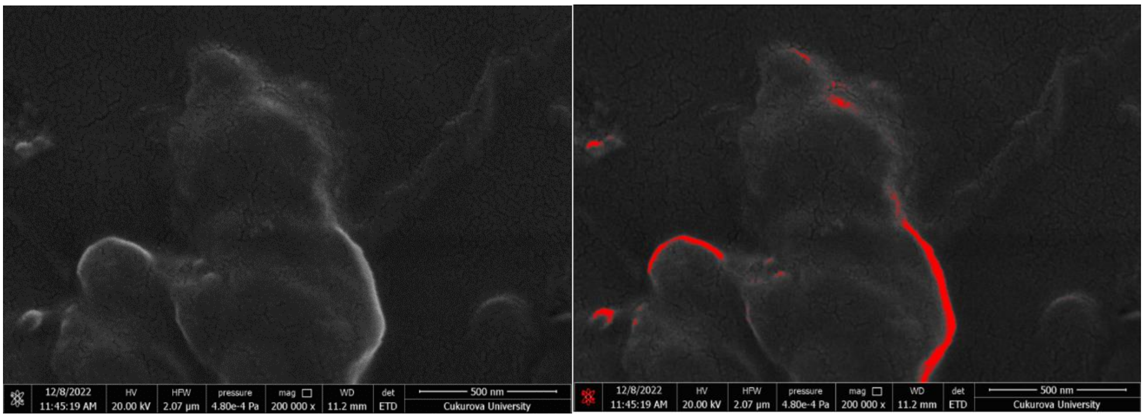

Figure 4.48. SEM image of 1wt%CB and its white zone representation on ImageJ software

Figure 4.49. gives the result of the threshold calculation by ImageJ software which is 0.96%. Notice that the software labels only the white areas not the grey ones and it can be clearly seen in the red labelled image that the grey dots around the red area was not picked.

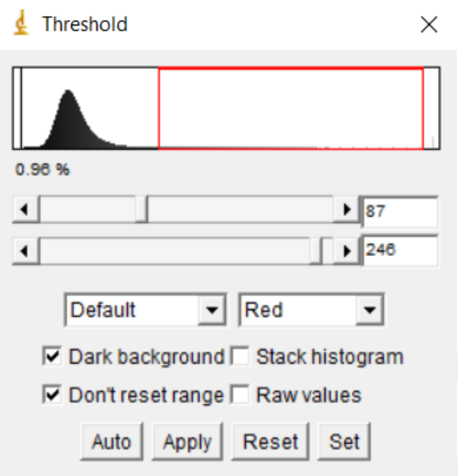

Figure 4.49. Area fraction calculation of 1wt% CB 200000 times magnified SEM image

The SEM image of specimen of 0.3wt% CB was examined with the software and 5000 times magnified image was used for area calculation which can be seen in Figure 4.50.

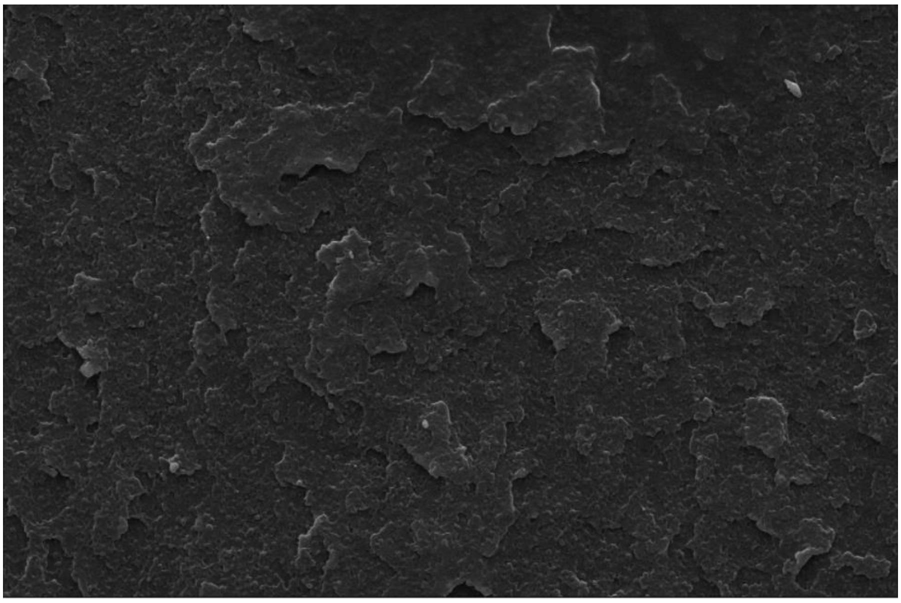

Figure 4.50. SEM image of 0.3wt% CB in 5000 times magnification

The representation of white zones with red color for better grasping of the view can be seen in Figure 4.51.

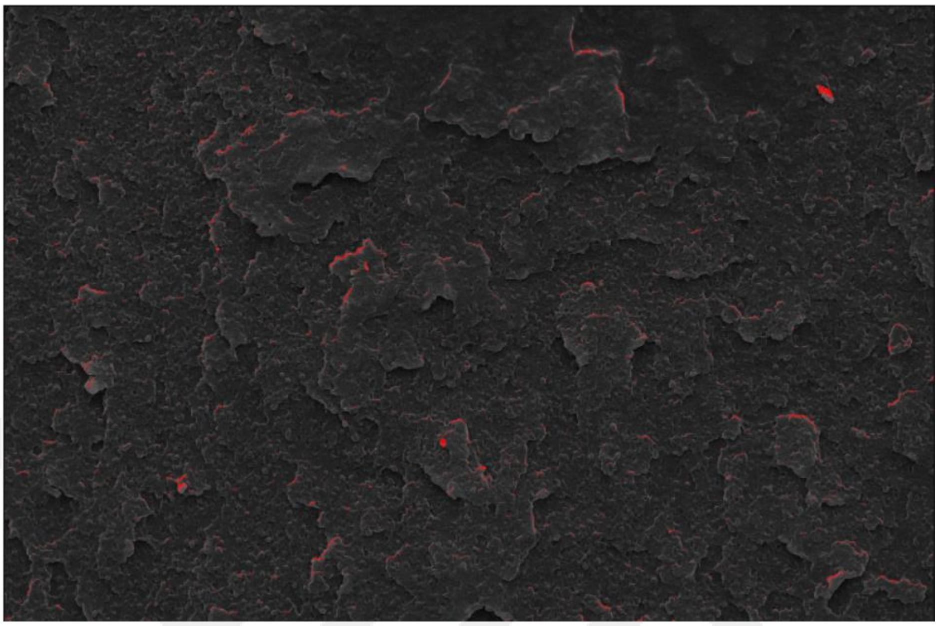

Figure 4.51. SEM image of 0.3wt% CB in 5000 times magnification with CB particles shown in red for area fraction calculation

The area calculation value of 0.39% was obtained and it can be seen in Figure 4.52. After having the conclusion that white areas represent CB nanoparticles, we shall assess the dispersion of CB nanoparticles in the ABS matrix for every weight fraction value.

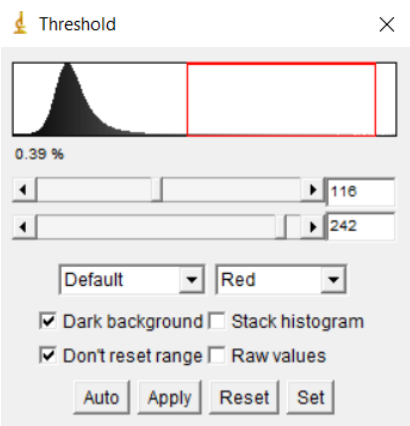

Figure 4.52. Area fraction calculation of 0.3wt% CB image in 5000 times magnification

By using the image processing software ImageJ, we can also show the white zones in contrast with black background to see how the particles are distributed in the ABS matrix via the SEM view. The black&white version of the image that was given in Figure 4.51 can be seen in Figure 4.53.

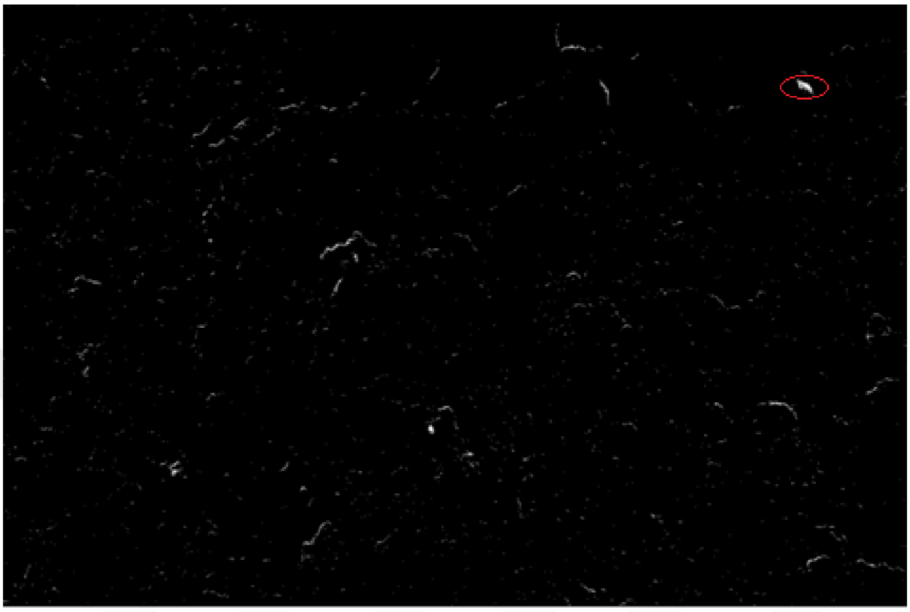

Figure 4.53. SEM image of 0.3wt% CB in 5000 times magnification with white dots representing CB nanoparticles

According to the image, an even distribution of the particles can be observed with only one agglomeration that is in a size which is obvious to observe and it is circled in a red line. This backs up the idea that the preparation and manufacturing of the composite filament was done successfully with evenly dispersed CB nanoparticles. When we consider the high surface area to volume ratio of Carbon Black nanoparticles, this distribution shows the characteristic of the nanoparticle.

In Figure 4.54, the SEM image of 5000 times magnified view of 1wt% CB nanocomposite specimen can be seen. In Figure 4.55, the modified black white image can be seen as well. It was observed that the agglomerations of CB particles increased in the 1wt% CB nanocomposite sample. These zones of agglomerated CB nanoparticles are circled in red. Due to these agglomerations, the distribution of the nanoparticles are less even compared to 0.3wt% CB nanocomposite specimen.

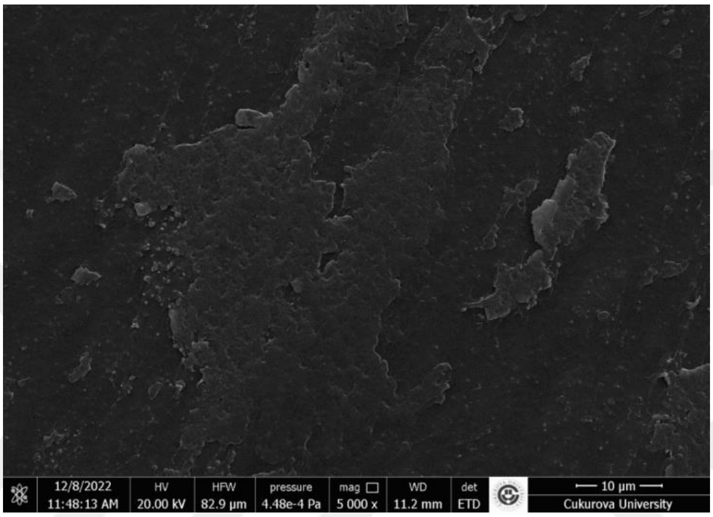

Figure 4.54. SEM image of 1wt% CB in 5000 times magnification

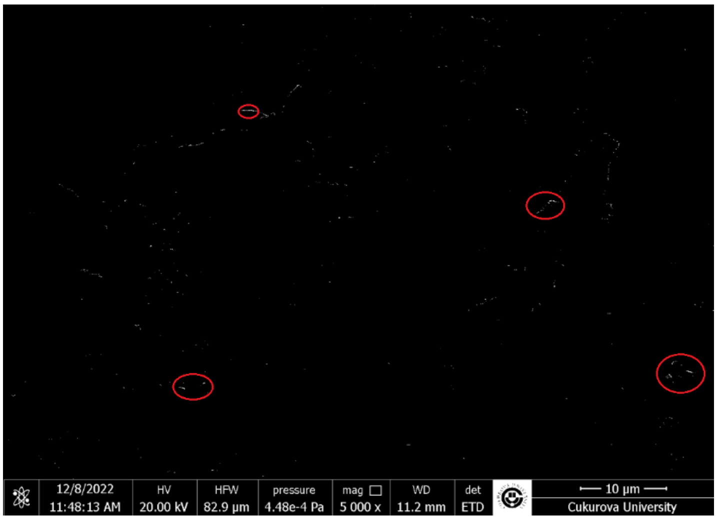

Figure 4.55. SEM image of 1wt% CB in 5000 times magnification with white dots representing CB nanoparticles

The 5000 times magnified SEM image of 2wt% CB nanocomposite specimen can be seen in Figure 4.56. The processed black and white image can be seen in Figure 4.57.

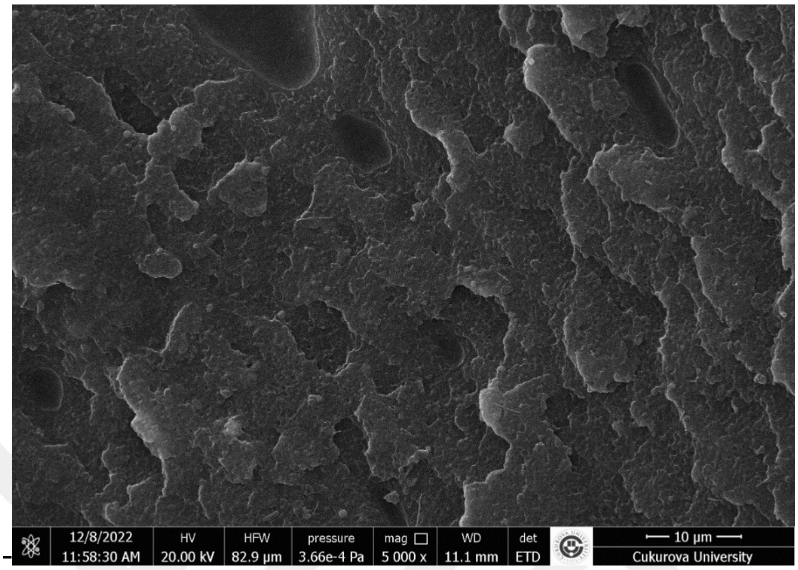

Figure 4.56. SEM image of 2wt% CB in 5000 times magnification

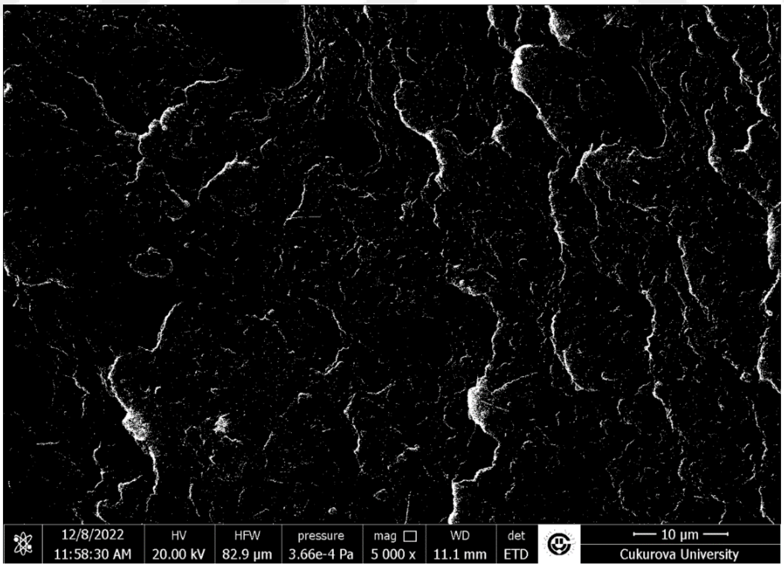

Figure 4.57. SEM image of 2wt% CB in 5000 times magnification with white dots representing CB nanoparticles

As it can be interpreted from the image in Figure 4.58, the agglomerations of CB nanoparticles are very much bigger in size compared to 1wt% CB nanocomposite image and the number of agglomerations are increased in a significant scale. The findings in the image are of great importance for interpreting the damping behavior of the specimen.

4.4. General overview of all results regarding nanocomposite beams of ABS+$CaCO_3$

As can be seen in Table 4.7, the natural frequency for ABS+$CaCO_3$ nanocomposites tend to decrease initially with added $CaCO_3$ nanoparticles and further addition resulting in 2wt% $CaCO_3$ makes no change in the natural frequency being equal to that of 1wt% $CaCO_3$ content. The addition of 3wt% $CaCO_3$ nanoparticles has caused an increase in the natural frequency value compared to 2wt% $CaCO_3$ content. Finally, the addition of 5wt% $CaCO_3$ nanoparticles caused a decrease in the natural frequency value compared to 3wt% $CaCO_3$ content. As seen in Table 4.7, the numerical natural frequency values display a parallel trend compared to the experimental results with varying percent error values.

We can observe that there are discrepancies between experimental and numerical results when we evaluate the numerical natural frequency values. In Table 4.7, these data are expressed as percent error values. The pure ABS computation has the least % error value compared to any calculation. It is important to note that some inaccuracy should be expected as a result of certain factors, such as the assumption that the beam specimens would be regarded to be made of isotropic materials. Due to the nature of the process, additively manufactured components are known to exhibit orthotropic behavior; nonetheless, this assumption was made to substantially simplify the numerical computation procedure.

Table 4.7. Comparison of experimental and numerical results

	Natural Frequency (Experimental) (Hz)	**Natural Frequency (Numerical) (Hz)**	**Percent Error**
Pure ABS	11.4748	11.151	2.82
ABS + 1wt% $CaCO_3$	11.2307	10.93	2.67
ABS + 2wt% $CaCO_3$	11.2307	10.97	2.32
ABS + 3wt% $CaCO_3$	11.4749	11.14	2.87
ABS + 5wt% $CaCO_3$	10.2542	9.91	3.35

Additionally, the analog to digital signal conversion in experimental vibration measurements results in some inaccuracy every time. The percent error values are acceptable despite the issues addressed earlier. The numerical and experimental values of $CaCO_3$ beams can be seen in the form of a graph in Figure 4.58.

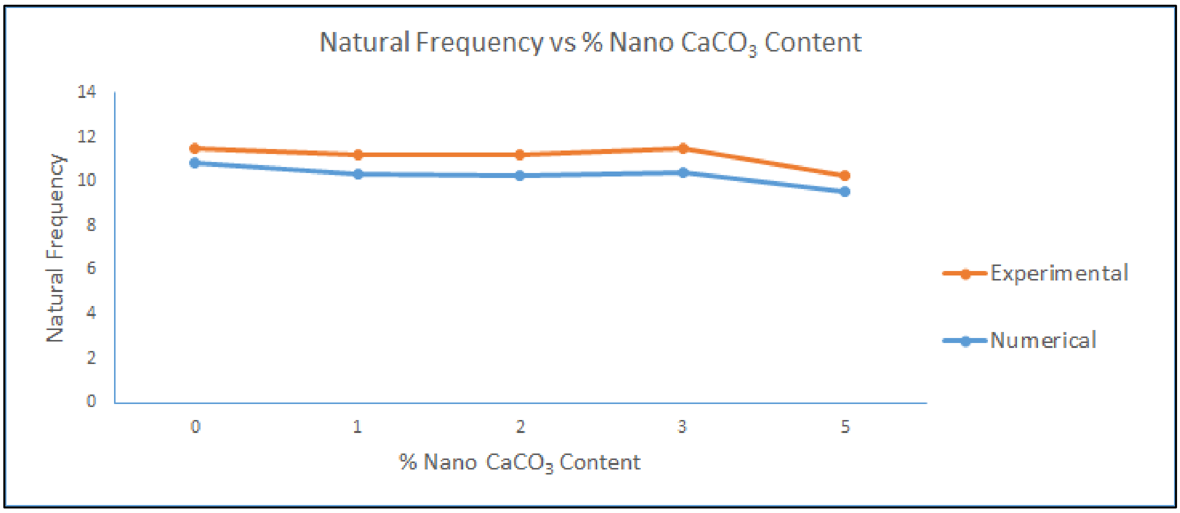

Figure 4.58. Graph of natural frequency along with % nano-$CaCO_3$ content for both experimental and numerical results

We can make the interpretation that the addition of $CaCO_3$ has limited effect on the natural frequency values. However, when we look at 5wt% $CaCO_3$ specimen there is a considerable decrease in natural frequency value compared to pure ABS specimen. This might be attributed to the decrease in stiffness which can be seen in the decrease in Young's Modulus however this cannot be the only reason for the decrease. When we look at the density values, we see that there is immense drop in the density value. As discussed in the SEM interpretations, huge voids were detected in 5wt% $CaCO_3$ sample images in FDM beads. The density decrease may be caused by these voids in the beads contributing to the decrease in natural frequency. As given in the theory part, the natural frequency heavily depends on the mass of the beam as well. These voids, if present in the beads, may also be contributing to the reason why the stiffness of the 5wt% specimen decreased. Of course the agglomerated nanoparticles may also be another effect decreasing the stiffness.

When we take a closer look at the damping ratio values, it is clearly observed that the damping ratio values increase with the increase in weight fraction of $CaCO_3$ nanoparticles. This can be clearly seen from the graph in Figure 4.59.

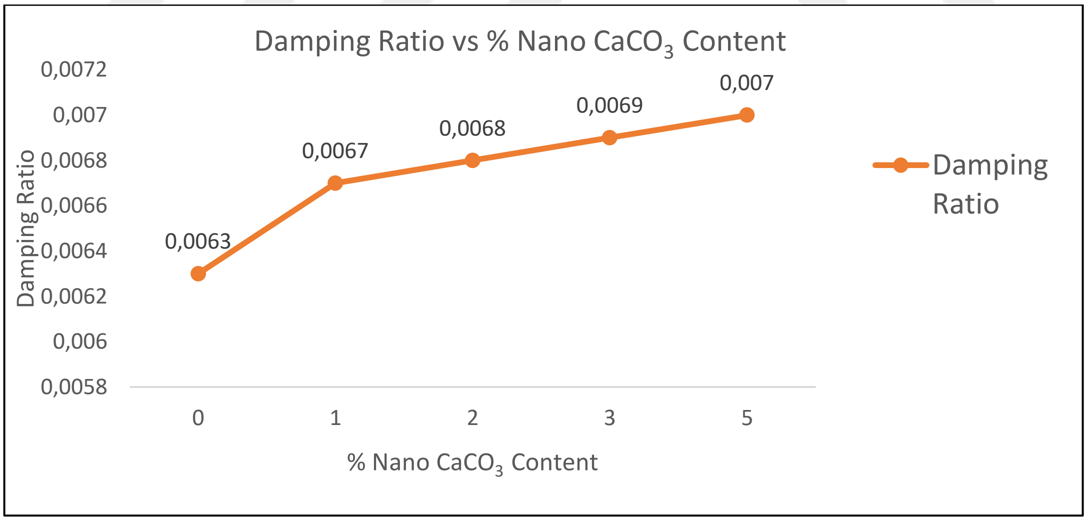

Figure 4.59. The graph of damping ratio changing with % Nano $CaCO_3$ content

The results for 1wt% $CaCO_3$ nanocomposite specimen indicate a relatively high increase in the damping ratio compared to pure AB specimen. Higher weight fractions showcase a lower increase ratio for every 1% increase in the weight fraction of the $CaCO_3$ nanoparticles. The rate of increase in the damping ratio value slows and becomes linear after 1wt% $CaCO_3$ nanocomposite specimen. This can also be observed in Figure 4.60. The reason for this slowing increase rate in damping ratio may also be explained by the stick slip mechanism mentioned in the following section. The SEM images present bigger sized agglomerations with higher weight fractions of $CaCO_3$ nanoparticle and this reduces the stick slip effect. This may be due to the smaller surface area formed by bundled aggregates caused by agglomerations compared to non-agglomerated uniformly distributed nanoparticles. Since the $CaCO_3$ nanoparticle couldn't be observed in the SEM image of 1wt% $CaCO_3$ specimen, the high increase in the damping ratio according to the slip stick theory may be the indicator that the most evenly dispersed specimen is the 1wt% $CaCO_3$ specimen. The percent change in damping ratio values were given in Table 4.8. These values were comparative values to pure ABS for every nanocomposite specimen with various nanoparticle content.

Table 4.8. The % change in damping ratios of nanocomposite beams compared to pure ABS

	Damping Ratio **(ζ)**	**Percent Change Compared to Pure ABS** **(%)**
Pure ABS	0.0063	-
ABS + 1wt% $CaCO_3$	0.0067	6.3
ABS + 2wt% $CaCO_3$	0.0068	7.9
ABS + 3wt% $CaCO_3$	0.0069	9.5
ABS + 5wt% $CaCO_3$	0.0070	11.1

4.5. General overview of all results regarding nanocomposite beams of ABS+CB

As can be seen in Table 4.7, the natural frequency for ABS+CB nanocomposites tend to increase initially with added CB nanoparticles and then showcase a declining trend with further increase in the CB nanoparticles. The addition of 0.3% CB nanoparticles has provided a 4.25% increase in the natural frequency value compared to the pure ABS cantilever beam. Addition of 1wt% CB has caused a decrease from that value and the natural frequency value became equal to that of pure ABS beam. The beam containing 2wt% CB displayed the lowest natural frequency value of 11.2305 Hz meaning a 2.12% decrease compared to pure ABS beam.

Table 4.9. Comparison of experimental and numerical results

	Natural Frequency (Experimental) (Hz)	**Natural Frequency (Numerical) (Hz)**	**Percent Error (%)**
Pure ABS	11.4746	11.151	2.82
ABS + 0.3wt% CB	11.9629	11.582	3.18
ABS + 1wt% CB	11.4746	11.023	3.93
ABS + 2wt% CB	11.2305	10.834	3.53

When we assess the numerical natural frequency values, we can see that there are differences in experimental and numerical values. These are given as percent error values in Table 4.7. The percent error value for pure ABS is the smallest among all calculations. It is essential to point out that some error should be expected due to some effects such as the assumption that the beam specimens would be considered isotropic materials. As known additively manufactured parts display orthotropic behavior owing to the nature of the process however this assumption was made to greatly simplify the numerical calculation process. Also, there is always some error occurring in the experimental vibration measurements due to the conversion of analog signals to digital signals. The error values are minimal and acceptable. The graph in Figure 4.60 shows the natural frequency value change regarding CB nanoparticle content both for experimental and numerical calculations.

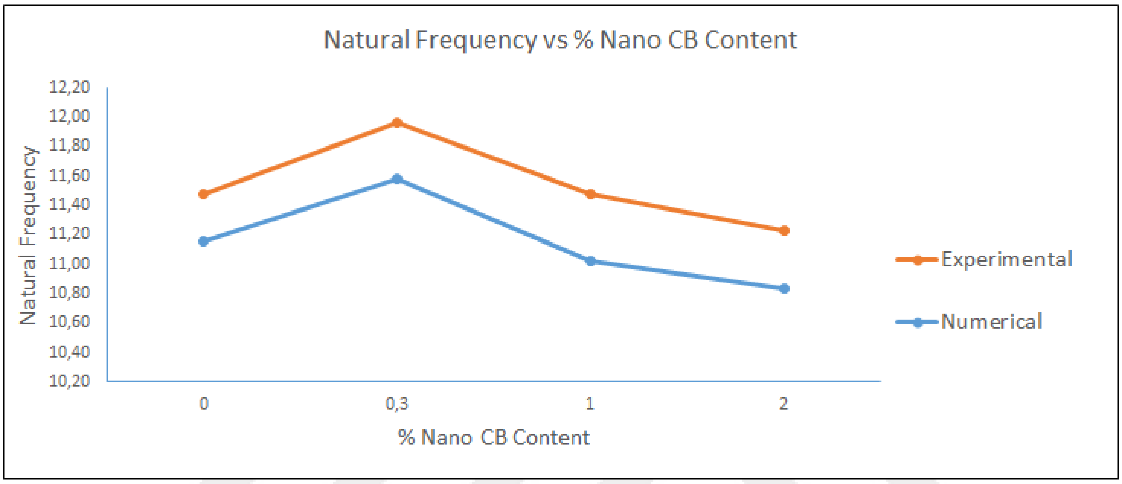

Figure 4.60. Graph of natural frequency along with % Nano CB content for both experimental and numerical results

Regarding the damping ratio values, the graph of damping ratio values with respect to % Nano CB content can be seen in Figure 4.61. It can be seen from the graph that the addition of 0.3wt% CB nanoparticles a significant increase in the damping ratio value compared to the pure ABS specimen. This significant increase means a 39,6% increase when compared to pure ABS cantilever beam. The addition of 0.3wt% CB to pure ABS results in an increase in the natural frequency and it also enhances the damping ratio considerably. Therefore, we can say that ABS + 0,3wt% CB nanocomposite filament is the most beneficial option when vibrational characteristics are taken into account.

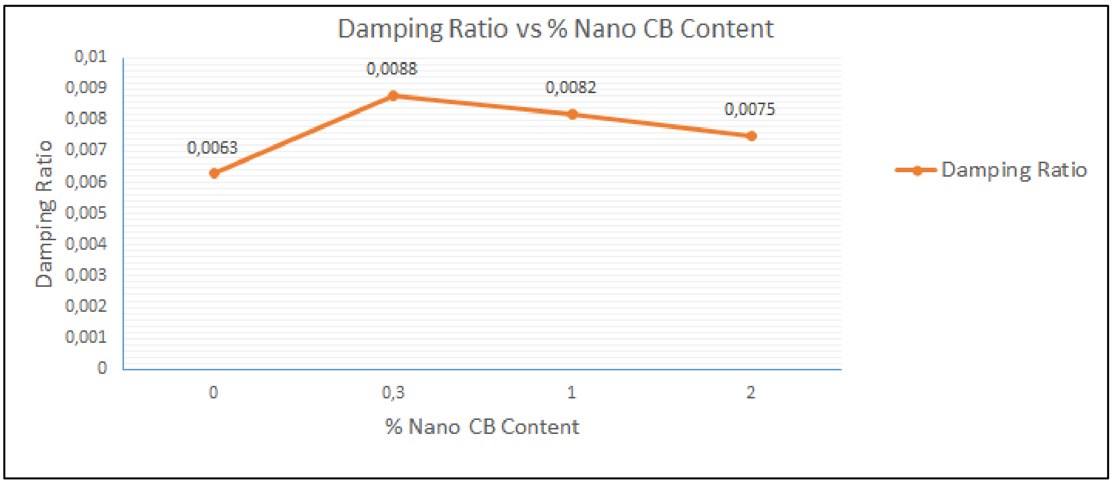

Figure 4.61. Graph of damping ratio change along with % Nano CB content

The % change in damping ratios of nanocomposite beams compared to pure ABS are listed in Table 4.8. In calculating the percent change, the values of every beam with certain CB content was always compared with the damping ratio of pure ABS beam to see the effect of CB content on damping.

Table 4.10. The % change in damping ratios of nanocomposite beams compared to pure ABS

	Damping Ratio	**Percent Change Compared to Pure ABS**
Pure ABS	0.0063	-
ABS + 0.3wt% CB	0.0088	39.6
ABS + 1wt% CB	0.0082	30.1
ABS + 2wt% CB	0.0075	19

Another phenomenon that is observed from the results is that the stiffness of the nanocomposites decreases with the addition of CB nanoparticles resulting in the natural frequency to decrease as well, especially in CB content more than 0.3wt%.

It is clearly evident that the inclusion of CB nanoparticles in the ABS matrix cause an extensive increase in the damping ratio values of the cantilever beam specimens. After its peak value the damping ratio starts to decrease with more CB nanoparticle inclusion however the values are still higher than that of pure ABS specimens.

The damping behavior can also be seen in Figure 4.62 where the displacement-time graphs of pure ABS and 0.3wt% CB nanocomposite beams show how the excitation is damped. As seen in the Figures, the pure ABS still continues to vibrate after seven seconds however 0.3wt% CB beam is at the end of its vibration. As mentioned in the previous chapter, the VDAS data logger has a limited memory which can store limited amount of data therefore for pure ABS all the vibration cannot be seen till its fully damped. Nevertheless, along with detailed calculations of the experiment, it can even be clearly seen from the graphs that addition of 0.3wt% CB significantly enhances the damping ratio value.

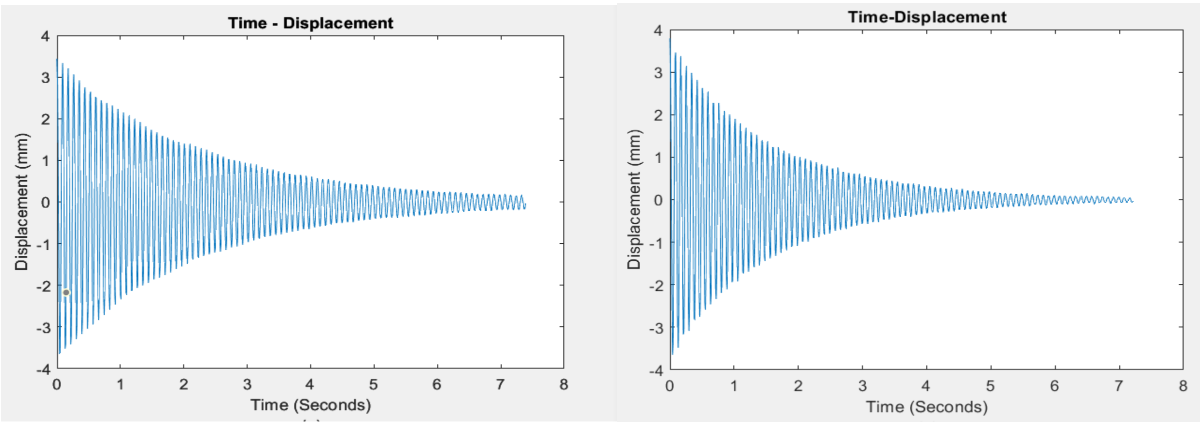

Figure 4.62. Time – displacement comparison of pure ABS (on the left) and 0.3wt CB beams (on the right)

This behavior was explained by a mechanism called ‘’stick-slip’’ which was used in [57] investigating vibration characteristics of nanocomposite cantilever beams.

When the results of CB nanocomposite cantilever beams were considered, we observe a similar change in damping ratio values. The addition of CB nanoparticles does not affect the stiffness of the beams too much according to the tensile test results, there is a small decrease in the elastic modulus of 1wt% and 2wt% CB nanocomposites. These decreases may be explained with the factors regarding nanoparticle addition and the parameters affecting the process fused deposition modeling. Regarding 0.3wt% CB nanocomposite beams, it can be seen that the stiffness value increases in a small amount (Table 4.5) however the damping ratio increases significantly. This is a very similar behavior compared to the behavior of epoxy-CNT composites explained with the stick-slip mechanism in the mentioned study. For higher weight-percent ratios of CB content the damping ratio values decrease concerning 0.3wt% CB content, which may be due to the agglomerations of CB nanoparticles causing less uniform dispersion in the ABS matrix, reducing the damping effect.

As given in Section 2 [59] investigated the effect of carbon nanotube content in epoxy matrix cantilever beams on damping characteristics. The increase in the CNT content initially increased the damping ratio however the further increase in the CNT content caused a smaller increase in the values. In the study, the maximum increase in the damping ratio was obtained with 0.4wt% CNT content providing a 41% improvement in the damping ratio compared to pure epoxy. In our study, a similar improvement was obtained with the 0.3wt% CB content providing a 39.6% improvement in damping ratio compared to pure ABS 3D printed beam in Mode 1 vibration. This improvement is a useful finding which can be helpful in 3D printed parts of strong ABS which are designed to work in environments where harsh vibration is present and the damping is of great importance. In such cases, these parts can be 3D printed with ABS + 0.3wt% CB nanocomposites for improved damping characteristics. Another important advantage of using CB nanoparticles to enhance damping characteristics instead of CNTs would be the cost advantage. CB is significantly cheaper than CNTs which would provide excellent damping enhancement with a cheaper alternative. ABS+CB nanocomposites would be a great solution for applications of automotive and aeronautics industries where vibration damping is crucial. It wouldn't be rational to apply the same mechanism between epoxy resin and CNTs however further research should be carried out to explain the mechanism that causes the damping enhancement with the use of CB nanoparticles in ABS matrix.

5. CONCLUSIONS

In this study, the free vibration behavior of 3D printed cantilever beams composed of ABS with Carbon Black and ABS with Calcium Carbonate nanoparticles in various weight fractions was studied. To compare the nanocomposite beams to pure ABS beams a pure ABS beam was also fabricated. Pure ABS and nanocomposite filaments were produced in-house by melt extruding the ABS granules and nanoparticles procured from the market. The weight fraction values used for the Calcium Carbonate nanocomposite filaments were 1%, 2%, 3%, and 5% and the weight fractions for Carbon Black nanocomposite filaments were 0.3%, 1%, and 2%. By using the produced filaments with Carbon Black and Calcium Carbonate nanoparticle additives of different weight fractions, cantilever beams were 3D printed for physical testing. Physical testing of the beams was carried out with vibration test equipment designed for the Mode 1 testing of cantilever beams. Natural frequency and damping ratio values were calculated by time – displacement data obtained from the physical tests. Along with the physical tests, numerical analysis of the beams was performed on computer software. For the numerical calculations, the mechanical properties of the produced nanocomposite materials were necessary. Tensile test specimens of the same parameters with the beams were also 3D printed for determining the mechanical properties of the nanocomposite materials. Tensile tests of the specimens were performed and mechanical properties were obtained. These properties were used in numerical analysis for the free vibration behavior of the beams for validation of the physical tests.

The results of the physical tests reveal that the highest natural frequency value obtained among all the nanocomposite beams was the CB/ABS nanocomposite beam containing 0.3wt% of CB nanoparticled with a frequency value of 11.9633 Hz. It was observed that the addition of Carbon black nanoparticles of 0.3% caused an increase in natural frequency values initially however further addition of Carbon Black nanoparticles of 1% and 2% resulted in the decrease of the natural frequency values of the nanocomposite beams. On the other hand, the 1% inclusion of Calcium Carbonate nanoparticles in the ABS matrix caused an initial decrease in natural frequency compared to pure ABS beam however nanocomposite beams of

3% $CaCO_3$ content had an increase in the natural frequency value. Finally, a decrease in natural frequency value was observed again for the nanocomposite beams having 5% $CaCO_3$ nanoparticles in the ABS matrix however the enhancement in the damping ratio is the highest with a 11.1% value.

The inclusion of 1% $CaCO_3$ nanoparticles in the ABS matrix resulted in an increase of 6.3 % in the damping ratio value compared to the pure ABS beam. Further increase in the $CaCO_3$ content resulted in smaller increases for every other nanocomposite beam of increased $CaCO_3$ content. Regarding CB/ABS nanocomposite beams the results showed that the inclusion of 0.3% CB nanoparticles in the ABS matrix resulted in a 39.6 % increase in the damping ratio compared to that of a pure ABS beam. The damping ratio for ABS+0.3wt% CB is the highest value among all beam specimens which is 0.0088. However further increase in CB content caused a decrease in the damping ratio in 1wt% and 2wt% CB nanocomposite ABS beams. The addition of 0.3wt% CB nanoparticles is the best choice since it causes an increase in the natural frequency along with a considerable enhancement of 39.6% in the damping ratio value.

6. RECOMMENDATIONS

In this thesis, an effort was made to investigate the free vibration behavior of 3D printed nanocomposite cantilever beams consisting of Carbon Black and Calcium Carbonade nanoparticles with various weight fractions. The beams were tested physically to determine natural frequency and damping ratio values. A numerical analysis of the beams was also performed for validation of the natural frequency values. Tensile test values were used in the numerical analysis procedure. Results were examined to see the effect of nanoparticle content on the natural frequency and damping ratio values. Some recommendations can be listed below for further investigations to be made on the subject;

- The natural frequency and the damping ratio values of the beams can be determined in higher modes of vibration such as Mode 2 and Mode 3 by using suitable vibration testing equipment.
- The effect of nanoparticle inclusion interacting with various printing parameters on vibrational behavior can be investigated as well. For instance, the printing geometry of the beams such as triangle, line and hexagon in combination with nanoparticle inclusion and their combined effects on vibration behavior can be investigated.
- The results of numerical calculations can be compared with other numerical analysis computer software such as ABAQUS.
- The specimen having 0.3wt% CB displayed the highest damping ratio however there is a gap between 0.3 and 1wt% CB specimens. A value between 0.3 and 1 can be tested in order to see if there is any further increase in the damping ratio value.
- The natural frequency and damping ratio characteristics of the nanocomposite beams can be measured in various ambient temperatures in order to see the effect of nanoparticle inclusion on the vibration behavior of the beams in various temperatures.
- The same nanoparticles of different particle sizes can be added to the filament materials and the effect of nanoparticle size on the vibration behavior of the beams can be investigated.
- In this study, ABS was used as the matrix material for the nanocomposite beams, in

further studies, a different thermoplastic as matrix material such as PLA can be used and the vibrational characteristics can be investigated.

- In this study the free vibration behavior of the nanocomposite beams was investigated, in further studies, the forced vibration characteristics of the same beams can be assessed with suitable test equipment.
- Filaments of nanocomposite content with 0.1wt% increments may be fabricated and beams of such materials may be 3D printed and vibration tests can be performed in order to find the optimum damping ratio for CB content since the gap between 0.3% and 1% was large. The damping ratio value may still increase for more than 0.3wt% CB content.

REFERENCES

[1] A. Nassehi, S. Newman, V. Dhokia, Z. Zhu, and R. I. Asrai, “Using formal methods to model hybrid manufacturing processes,” *Enabling Manuf. Compet. Econ. Sustain.*, pp. 52–56, 2012

[2] I. Gibson, D. Rosen, and B. Stucker, *Additive Manufacturing Technologies*. New York: Springer, 2015.

[3] C. Sun, Y. Wang, M. D. McMurtrey, N. D. Jerred, F. Liou, and J. Li, “Additive manufacturing for energy: A review,” *Appl. Energy*, vol. 282, no. May 2020, 2021

[4] M. K. Niaki, S. A. Torabi, and F. Nonino, “Why manufacturers adopt additive manufacturing technologies: The role of sustainability,” *J. Clean. Prod.*, vol. 222, pp. 381–392, 2019

[5] A. Bhargav, V. Sanjairaj, V. Rosa, L. W. Feng, and J. Fuh YH, “Applications of additive manufacturing in dentistry: A review,” *J. Biomed. Mater. Res. - Part B Appl. Biomater.*, vol. 106, no. 5, pp. 2058–2064, 2018

[6] F. J. Mercado Rivera and A. J. Rojas Arciniegas, “Additive manufacturing methods: techniques, materials, and closed-loop control applications,” *Int. J. Adv. Manuf. Technol.*, vol. 109, no. 1–2, pp. 17–31, 2020

[7] M. Pagac *et al.*, “A review of vat photopolymerization technology: Materials, applications, challenges, and future trends of 3d printing,” *Polymers (Basel).*, vol. 13, no. 4, pp. 1–20, 2021

[8] O. Gülcan and K. Günaydın, “The State of the Art of Material Jetting — A Critical Review,” Polymers, vol. 13, no. 16, p. 2829, Aug. 2021.

[9] S. C. Ligon, R. Liska, J. Stampfl, M. Gurr, and R. Mülhaupt, “Polymers for 3D Printing and Customized Additive Manufacturing,” *Chem. Rev.*, vol. 117, no. 15, pp. 10212–10290, 2017

[10] F. M. Mwema and E. T. Akinlabi, “Basics of Fused Deposition Modelling (FDM),” *SpringerBriefs Appl. Sci. Technol.*, pp. 1–15, 2020

[11] A. D. Valino, J. R. C. Dizon, A. H. Espera, Q. Chen, J. Messman, and R. C. Advincula, “Advances in 3D printing of thermoplastic polymer composites and nanocomposites,”

Prog. Polym. Sci., vol. 98, p. 101162, 2019

[12] A. Jaisingh Sheoran and H. Kumar, “Fused Deposition modeling process parameters optimization and effect on mechanical properties and part quality: Review and reflection on present research,” *Mater. Today Proc.*, vol. 21, pp. 1659–1672, 2020

[13] F. Górski, R. Wichniarek, W. Kuczko, P. Zawadzki, and P. Buń, “Strength of Abs Parts Produced By Fused Deposition Modelling Technology – a Critical Orientation Problem,” *Adv. Sci. Technol. Res. J.*, vol. 9, no. 26, pp. 12–19, 2015

[14] N. Boyard, O. Christmann, M. Rivette, O. Kerbrat, and S. Richir, “Support optimization for additive manufacturing: Application to FDM,” *Rapid Prototyp. J.*, vol. 24, no. 1, pp. 69–79, 2018

[15] W. Ma, W. C. But, and P. He, “NURBS-based adaptive slicing for efficient rapid prototyping,” *CAD Comput. Aided Des.*, vol. 36, no. 13, pp. 1309–1325, 2004

[16] A. Dey, I. N. R. Eagle, and N. Yodo, “A review on filament materials for fused filament fabrication,” *J. Manuf. Mater. Process.*, vol. 5, no. 3, p. 69, 2021

[17] N. Vidakis *et al.*, “Strain rate sensitivity of polycarbonate and thermoplastic polyurethane for various 3d printing temperatures and layer heights,” *Polymers (Basel).*, vol. 13, no. 16, p. 2752, 2021

[18] D. Fico, D. Rizzo, R. Casciaro, and C. E. Corcione, “A Review of Polymer-Based Materials for Fused Filament Fabrication (FFF): Focus on Sustainability and Recycled Materials,” *Polymers (Basel).*, vol. 14, no. 3, p. 465, 2022

[19] J. Lee, J. An, and C. K. Chua, “Fundamentals and applications of 3D printing for novel materials,” *Appl. Mater. Today*, vol. 7, pp. 120–133, 2017

[20] R. Kumar and R. Singh, “On the 3D printing of recycled ABS , PLA and HIPS thermoplastics for structural applications,” vol. 2, no. 2, pp. 115–137, 2018

[21] A. Dey and N. Yodo, “A systematic survey of FDM process parameter optimization and their influence on part characteristics,” *J. Manuf. Mater. Process.*, vol. 3, no. 3, p. 64, 2019

[22] M. Kunovjanek and C. Wankmüller, “An analysis of the global additive manufacturing response to the COVID-19 pandemic,” *J. Manuf. Technol. Manag.*, vol. 32, no. 9, pp. 75–100, 2020

[23] A. K. Kaw, *Micromechanics of Composite Materials*. Boca Raton, FL, Taylor and

Francis LLC, 2006.

[24] T. W. Clyne and D. Hull, *An Introduction to Composite Materials*., University Printing House, Cambridge University Press, 2019.

[25] S. S. Rao, “Fundamentals of Vibration”, Mechanical Vibrations Sixth Edition in SI Units, London Road, Harlow. Pearson Education Ltd., 2018, Chapter 1, pp 46-47.

[26] A. K.Chopra, "Free Vibration", *Dynamics of Structures*, Global Edi., Harlow: Pearson Education Limited, 2014, Chapter 2, pp 39-54.

[27] T. D. Ngo, A. Kashani, G. Imbalzano, K. T. Q. Nguyen, and D. Hui, “Additive manufacturing (3D printing): A review of materials, methods, applications and challenges,” *Compos. Part B Eng.*, vol. 143, no. December 2017, pp. 172–196, 2018

[28] M. Nikzad, S. H. Masood, and I. Sbarski, “Thermo-mechanical properties of a highly filled polymeric composites for Fused Deposition Modeling,” *Mater. Des.*, vol. 32, no. 6, pp. 3448–3456, 2011

[29] J. Justo, L. Távara, L. García-Guzmán, and F. París, “Characterization of 3D printed long fibre reinforced composites,” *Compos. Struct.*, vol. 185, pp. 537–548, 2017

[30] L. G. Blok, M. L. Longana, H. Yu, and B. K. S. Woods, “An investigation into 3D printing of fibre reinforced thermoplastic composites,” *Addit. Manuf.*, vol. 22, pp. 176–186, 2018

[31] K. Prashantha and F. Roger, “Multifunctional properties of 3D printed poly(lactic acid)/graphene nanocomposites by fused deposition modeling,” *J. Macromol. Sci. Part A Pure Appl. Chem.*, vol. 54, no. 1, pp. 24–29, 2016

[32] J. Bustillos, D. Montero, P. Nautiyal, A. Loganathan, B. Boesl, and A. Agarwal, “Integration of graphene in poly(lactic) acid by 3D printing to develop creep and wear-resistant hierarchical nanocomposites,” *Polym. Compos.*, vol. 39, no. 11, pp. 3877–3888, 2018

[33] J. Gonçalves *et al.*, “Electrically conductive polyetheretherketone nanocomposite filaments: From production to fused deposition modeling,” *Polymers (Basel).*, vol. 10, no. 8, pp. 1–20, 2018

[34] J. F. Christ, C. J. Hohimer, N. Aliheidari, A. Ameli, C. Mo, and P. Pötschke, “3D printing of highly elastic strain sensors using polyurethane/multiwall carbon nanotube composites,” *Sensors Smart Struct. Technol. Civil, Mech. Aerosp. Syst. 2017*, vol.

10168, no. April 2017, p. 101680E1-101680E7, 2017

[35] C. Aumnate, A. Pongwisuthiruchte, P. Pattananuwat, and P. Potiyaraj, “Fabrication of ABS/Graphene oxide composite filament for fused filament fabrication (FFF) 3D Printing,” *Adv. Mater. Sci. Eng.*, vol. 2018, article ID 2830437, 9 pages, 2018

[36] H. K. Sezer and O. Eren, “FDM 3D printing of MWCNT re-inforced ABS nano-composite parts with enhanced mechanical and electrical properties,” *J. Manuf. Process.*, vol. 37, no. December 2017, pp. 339–347, 2019

[37] Z. Weng, J. Wang, T. Senthil, and L. Wu, “Mechanical and thermal properties of ABS/montmorillonite nanocomposites for fused deposition modeling 3D printing,” *Mater. Des.*, vol. 102, pp. 276–283, 2016

[38] S. Dul, L. Fambri, and A. Pegoretti, “Fused deposition modelling with ABS-graphene nanocomposites,” *Compos. Part A Appl. Sci. Manuf.*, vol. 85, pp. 181–191, 2016

[39] N. Vidakis *et al.*, “The mechanical and physical properties of 3D-Printed materials composed of ABS-ZnO nanocomposites and ABS-ZnO microcomposites,” *Micromachines,* vol. 11, no. 6, pp. 1–20, 2020

[40] N. Vidakis, M. Petousis, A. Maniadi, E. Koudoumas, M. Liebscher, and L. Tzounis, “Mechanical properties of 3D-printed acrylonitrile-butadiene-styrene TiO2 and ATO nanocomposites,” *Polymers (Basel).*, vol. 12, no. 7, pp. 1–16, 2020

[41] T. J. Quill *et al.*, “Thermal and mechanical properties of 3D printed boron nitride – ABS composites,” *Appl. Compos. Mater.*, vol. 25, no. 5, pp. 1205–1217, 2017

[42] L. Zárybnická, R. Ševčík, J. Pokorný, D. Machová, E. Stránská, and J. Šál, “$CaCO_3$ Polymorphs Used as Additives in Filament Production for 3D Printing,” *Polymers (Basel).*, vol. 14, no. 199, 2022

[43] C. Wang *et al.*, “Reinforcement of polylactic acid for fused deposition modeling process with nanoparticles treated bamboo powder,” *Polymers (Basel).*, vol. 11, no. 1146, 2019

[44] L. Jiang, Y. C. Lam, K. C. Tam, T. H. Chua, G. W. Sim, and L. S. Ang, “Strengthening acrylonitrile-butadiene-styrene (ABS) with nano-sized and micron-sized calcium carbonate,” *Polymer (Guildf).*, vol. 46, no. 1, pp. 243–252, 2004

[45] S. Meng, H. He, Y. Jia, P. Yu, B. Huang, and J. Chen, “Effect of nanoparticles on the mechanical properties of acrylonitrile–butadiene–styrene specimens fabricated by fused

deposition modeling," *J. Appl. Polym. Sci.*, vol. 134, no. 44470, pp. 1–9, 2017

[46] Seyedzavvar, M. and Boga ,C., "A study on the effects of internal architecture on the mechanical properties and mixed-mode fracture behavior of 3D printed $CaCO_3$ / ABS nanocomposite samples," vol. 29, no. 1, pp. 185-206, 2022

[47] J. Sudeepan, K. Kumar, T. K. Barman, and P. Sahoo, "Study of Tribological Behavior of ABS/ CaCO 3 Composite Using Grey Relational Analysis," *Procedia Mater. Sci.*, vol. 6, no. Icmpc, pp. 682–691, 2014

[48] B. Li, S. Zhang, L. Zhang, Y. Gao, and F. Xuan, "Strain sensing behavior of FDM 3D printed carbon black filled TPU with periodic configurations and flexible substrates," *J. Manuf. Process.*, vol. 74, no. December 2021, pp. 283–295, 2022

[49] J. Beniak, L. Šooš, P. Križan, M. Matúš, and V. Ruprich, "Resistance and Strength of Conductive PLA Processed by FDM Additive Manufacturing," *Polymers (Basel).*, vol. 14, no. 678, 2022

[50] R. Hashemi Sanatgar, C. Campagne, and V. Nierstrasz, "Investigation of the adhesion properties of direct 3D printing of polymers and nanocomposites on textiles: Effect of FDM printing process parameters," *Appl. Surf. Sci.*, vol. 403, pp. 551–563, 2017

[51] P. H. M. Cardoso, M. F. L. de Oliveira, M. G. de Oliveira, and R. M. da Silva Moreira Thiré, "3D Printed Parts of Polylactic Acid Reinforced with Carbon Black and Alumina Nanofillers for Tribological Applications," *Macromol. Symp.*, vol. 394, no. 1, pp. 1–13, 2020

[52] L. Lei, Z. Yao, J. Zhou, B. Wei, and H. Fan, "3D printing of carbon black/polypropylene composites with excellent microwave absorption performance," *Compos. Sci. Technol.*, vol. 200, no. June, p. 108479, 2020

[53] N. Jayanth and P. Senthil, "Application of 3D printed ABS based conductive carbon black composite sensor in void fraction measurement," *Compos. Part B Eng.*, vol. 159, no. September 2018, pp. 224–230, 2019

[54] N. Jayanth, P. Senthil, and B. Mallikarjuna, "Experimental investigation on the application of FDM 3D printed conductive ABS-CB composite in EMI shielding," *Radiat. Phys. Chem.*, vol. 198, no. April, p. 110263, 2022

[55] J. Zhang, B. Yang, F. Fu, F. You, X. Dong, and M. Dai, "Resistivity and its anisotropy characterization of 3D-printed acrylonitrile butadiene styrene copolymer (ABS)/carbon

black (CB) composites," *Appl. Sci.*, vol. 7, no. 20, 2017

[56] M. Dawoud, I. Taha, and S. J. Ebeid, "Strain sensing behaviour of 3D printed carbon black filled ABS," *J. Manuf. Process.*, vol. 35, no. July 2017, pp. 337–342, 2018

[57] H. Rajoria and N. Jalili, "Passive vibration damping enhancement using carbon nanotube-epoxy reinforced composites," *Compos. Sci. Technol.*, vol. 65, no. 14, pp. 2079–2093, 2005

[58] F. De Borbón, D. Ambrosini, and O. Curadelli, "Damping response of composites beams with carbon nanotubes," *Compos. Part B Eng.*, vol. 60, pp. 106–110, 2014

[59] S. Pan, Q. Dai, B. Safaei, Z. Qin, and F. Chu, "Damping characteristics of carbon nanotube reinforced epoxy nanocomposite beams," *Thin-Walled Struct.*, vol. 166, no. June, p. 108127, 2021

[60] K. V. Singh, F. Khan, J. Veta, and A. K. Singh, "Influence of printing orientation on the dynamic characteristics and vibration behavior of 3d printed structures," Proceedings of the ASME 2017 International Design EngineeringTechnical Conferences and Computers and Information in Engineering. 2017

[61] M. Mansour, K. Tsongas, D. Tzetzis, and A. Antoniadis, "Mechanical and Dynamic Behavior of Fused Filament Fabrication 3D Printed Polyethylene Terephthalate Glycol Reinforced with Carbon Fibers," *Polym. - Plast. Technol. Eng.*, vol. 57, no. 16, pp. 1715–1725, 2018

[62] M. Amirpour, S. Bickerton, E. Calius, B. R. Mace, and R. Das, "Numerical and experimental study on free vibration of 3D-printed polymeric functionally graded plates," *Compos. Struct.*, vol. 189, no. January, pp. 192–205, 2018

[63] F. Ali and B. V. Chowdary, "Natural Frequency prediction of FDM manufactured parts using ANN approach," *IFAC-PapersOnLine*, vol. 52, no. 13, pp. 403–408, 2019

[64] M. Mansour, K. Tsongas, and D. Tzetzis, "Measurement of the mechanical and dynamic properties of 3D printed polylactic acid reinforced with graphene," *Polym. Technol. Mater.*, vol. 58, no. 11, pp. 1234–1244, 2019

[65] S. Kannan and M. Ramamoorthy, "Mechanical characterization and experimental modal analysis of 3D Printed ABS, PC and PC-ABS materials," *Mater. Res. Express,* vol. 7, no 015341, 2020

[66] S. Kannan, M. Ramamoorthy, E. Sudhagar, and B. Gunji, "Mechanical characterization

and vibrational analysis of 3D printed PETG and PETG reinforced with short carbon fiber," *AIP Conf. Proc.*, vol. 2270, no. 030004-1–030004-6; November, 2020

[67] T. Yao, H. Ouyang, S. Dai, Z. Deng, and K. Zhang, "Effects of manufacturing micro-structure on vibration of FFF 3D printing plates: Material characterisation, numerical analysis and experimental study," *Compos. Struct.*, vol. 268, no. September 2020, p. 113970, 2021

[68] R. C. Parpala, D. Popescu, and C. Pupaza, "Infill parameters influence over the natural frequencies of ABS specimens obtained by extrusion-based 3D printing," *Rapid Prototyp. J.*, vol. 27, no. 6, pp. 1273–1285, 2021

[69] M. Palmieri, G. Zucca, G. Morettini, L. Landi, and F. Cianetti, "Vibration Fatigue of FDM 3D Printed Structures: The Use of Frequency Domain Approach," *Materials (Basel).*, vol. 15, no. 3, pp. 1–18, 2022